


Analysis of second moments and their budgets for Richtmyer-Meshkov instability and variable-density turbulence induced by reshock

Man Long Wong *

Department of Aeronautics and Astronautics, & Center for Turbulence Research, Stanford University, Stanford, California 94305, USA

Jon R. Baltzer 

XTD-IDA, Los Alamos National Laboratory, Los Alamos, New Mexico 87545, USA

Daniel Livescu 

CCS-2, Los Alamos National Laboratory, Los Alamos, New Mexico 87545, USA

Sanjiva K. Lele

Department of Aeronautics and Astronautics, Department of Mechanical Engineering, & Center for Turbulence Research, Stanford University, Stanford, California 94305, USA



(Received 19 November 2021; accepted 18 March 2022; published 11 April 2022)

Nonlinear Richtmyer-Meshkov instability and the mixing transition induced by a Mach 1.45 shock and subsequent reshock at an interface between two ideal gases (sulfur hexafluoride and air) with high Atwood number are studied with second-moment analysis using data from high-resolution compressible Navier-Stokes simulations. The analysis first addresses the importance of two second-order moments: turbulent mass flux and density-specific-volume covariance, together with their transport equations. These quantities play an essential role in the development of Favre-averaged Reynolds stress and turbulent kinetic energy in this variable-density flow. Then, grid sensitivities and the time evolution of the turbulent quantities, which include the second moments, are investigated, followed by a detailed study of the transport equations for the second moments, including the Reynolds stress and the turbulent kinetic energy with well-resolved data before reshock. After reshock, budgets of the same but large-scale turbulent quantities are studied with the effects of the subfilter-scale stress taken into account. The budgets of these large-scale quantities are shown to have an insignificant influence from the numerical regularization. Finally, the effects of the subfilter-scale stress on the budgets of the large-scale turbulent quantities with different degrees of filtering are also examined.

DOI: [10.1103/PhysRevFluids.7.044602](https://doi.org/10.1103/PhysRevFluids.7.044602)

I. INTRODUCTION

Richtmyer-Meshkov (RM) instability (RMI) [1,2] arises in many natural phenomena and engineering applications when a shock wave traverses an interface separating two materials of different densities [3]. RMI is used by astrophysicists to explain the cause of turbulent mixing during a supernova explosion [4–6], and it is also taken into account in many stellar models [7]. In inertial confinement fusion (ICF), it is a common belief that there exists mixing between the capsule

*mlwong@alumni.stanford.edu

material and fuel due to RMI, and this prohibits a useful yield obtained from a fusion reaction for power generation [8–10]. RMI is also employed in some proposed combustion systems since it can enhance the mixing of fuel and oxidizer in supersonic and hypersonic air-breathing engines [11,12]. RMI is similar to Rayleigh-Taylor (RT) instability (RTI), which appears when there is a gravitational acceleration pointing in the opposite direction of the density gradient across an interface. In contrast to RTI, RMI occurs because of impulsive acceleration and is unstable regardless of the direction of the acceleration. Turbulent mixing induced from RMI and RTI with high density variations at the interfaces falls into the category of variable-density turbulence [13], where the Atwood number, which is defined as the difference in the fluid densities divided by their sum, is high. Variable-density turbulent mixing can also be triggered by other types of instabilities at an interface, such as Kelvin-Helmholtz (KH) instability (KHI), at a shear layer [13].

Direct numerical simulation (DNS) [14], which resolves all flow scales using a mesh with grid spacing of at least an order of magnitude of the Kolmogorov scale, is a powerful tool for studying turbulent flows, especially flows with a laminar to turbulent transition. However, its requirements of computational resources is tremendous for high Reynolds number flows, and it is computationally too expensive for many engineering applications, even on the largest supercomputers to date. As a result, turbulence modeling approaches are commonly adopted to avoid resolving all spatial and temporal scales in simulations of complex turbulent flows. Large-eddy simulation (LES) and Reynolds-averaged Navier-Stokes (RANS) methodologies are two popular modeling strategies [15,16]. LES consists of modeling of small scales that are assumed to be more universal and self-similar, while the larger scales are resolved on the grid. On the other hand, the entire flow structure is modeled based on statistical averaging in the RANS approach. In general, LES has higher fidelity than RANS-based simulations for turbulent flows where unsteady large scales play critical roles, since the large-scale features are resolved in LES. However, LES also has a larger demand on computational resources due to constraints on grid spacing and time step size for representing the motions of the scales captured. Often, the hybrid RANS-LES approach is chosen as a compromise between computational cost and accuracy [17].

The Besnard-Harlow-Rauenzahn (BHR) family of models based on second-moment closure represent a popular RANS-based approach for variable-density turbulence. The first version of the BHR model was proposed by Besnard *et al.* [18], in which the unclosed Reynolds stress tensor in the multispecies Favre-averaged (density-weighted-averaged) Navier-Stokes (FANS) equations is closed with the aid of additional modeled transport equations. These include modeled equations of decay rate of turbulent kinetic energy and other second-moment quantities, such as turbulent mass flux and density-specific-volume covariance. These second moments play important roles in variable-density turbulence; in particular, the turbulent mass flux directly affects the development of Favre-averaged Reynolds stress. The modeling assumptions of the first BHR model were not tested against different types of variable-density flows until the work by Banerjee *et al.* [19], where simplifications of the original BHR model were also introduced. In their model (BHR *k-S-a*), the Favre-averaged equations are closed with the turbulent kinetic energy transport equation instead of the equation of the Reynolds stress tensor. The transport equation of the decay rate of turbulent kinetic energy is also replaced with a more physically interpretable transport equation of turbulent length scale. Their model was validated with experimental data, but the model coefficients are tuned from flow to flow. Later, the BHR-2 model by Stalsberg-Zarling and Gore [20] was proposed. BHR-2 readopts the modeled transport equation of density-specific-volume covariance instead of an algebraic model in the BHR *k-S-a* model, which is only strictly valid for immiscible fluids. An improved BHR-3 model with modeled transport equations of the Reynolds stress tensor and density-specific-volume covariance was proposed by Schwarzkopf *et al.* [21] and was shown to be capable of capturing the Reynolds normal stress anisotropy and density-specific-volume covariance well in various variable-density flows, without varying model coefficients. The BHR-3 model was further improved by Schwarzkopf *et al.* [22] with two length scales to capture the difference between the transport and dissipation turbulent scales in RTI-induced turbulence. A two-point spectral closure model [23,24] modified from the constant-density BHRZ model [25] for variable-density flows was

analyzed for the buoyancy-driven variable-density homogeneous turbulence [26]. The model with minimal augmentation was further assessed for the RTI turbulence [27]. In addition to the BHR family of models, there are also similar models for turbulent mixing, such as the second-moment model by Grégoire *et al.* [28] with a Boussinesq approximation, and the k - L - a model by Morgan and Wickett [29] extended from the k - L model [30]. A literature review of different RANS-based models for RMI and other types of variable-density turbulence is provided by Zhou [31].

Modeling based on the transport of second moments is more popular in the RANS-based approach for variable-density flows, and most proposed LES models for the subfilter-scale (SFS) or subgrid-scale (SGS) terms are based on first-order closures [32]. These include the eddy-viscosity type SFS/SGS closure [33–35] and the stretched-vortex approach, such as [36,37]. There is still a lack of research on the application of second moments for the closure of SFS/SGS terms in LES. Besides, the role of SFS/SGS terms on the large-scale turbulent quantities, especially the resolved turbulent kinetic energy in variable-density flows, is still unclear. In this paper, we have performed high-resolution RMI simulations with reshock to provide high-fidelity data for analyzing the physical mechanisms underlying the evolution of second moments. The setup of the numerical experiment follows the highest Reynolds number three-dimensional (3D) case in our previous paper [38]. Before reshock, the instability induced at the interface grows nonlinearly but does not achieve the mixing transition. After reshock, the flow inside the mixing layer transitions and remains turbulent with a wide span of scales until the end of the simulation. The 3D simulation presented in this work is advanced to higher grid resolution compared to the cases in the previous work, with the number of grid cells exceeding 4.5 billion. Grid sensitivity tests show that the second moments required for closing the FANS equations are well grid-converged during the simulations. We also examine the budgets of the second-moment transport equations before and after reshock. The budgets analyzed after reshock are based on large-scale contributions to second moments under the influence of the SFS stress. The budgets of the large-scale second moments are not affected by the numerical regularization, and the effects of SFS stress in the evolution of large-scale second moments are studied. Finally, we also analyze the large-scale second-moment budgets at different filtering scales.

II. GOVERNING EQUATIONS

The conservative multicomponent Navier-Stokes equations are solved in this study:

$$\frac{\partial \rho Y_i}{\partial t} + \nabla \cdot (\rho \mathbf{u} Y_i) = -\nabla \cdot \mathbf{J}_i, \quad (1)$$

$$\frac{\partial \rho \mathbf{u}}{\partial t} + \nabla \cdot (\rho \mathbf{u} \mathbf{u} + p \boldsymbol{\delta}) = \nabla \cdot \boldsymbol{\tau}, \quad (2)$$

$$\frac{\partial E}{\partial t} + \nabla \cdot [(E + p) \mathbf{u}] = \nabla \cdot (\boldsymbol{\tau} \cdot \mathbf{u} - \mathbf{q}_c - \mathbf{q}_d), \quad (3)$$

where ρ , $\mathbf{u} = [u, v, w]^T = [u_1, u_2, u_3]^T$, p , and E are the density, velocity vector, pressure, and total energy of the fluid mixture, respectively. Y_i is the mass fraction of species $i \in [1, 2, \dots, N]$, with N the total number of species. \mathbf{J}_i is diffusive mass flux for species i . $\boldsymbol{\tau}$, \mathbf{q}_c , and \mathbf{q}_d are the viscous stress tensor, conductive heat flux, and interspecies diffusional enthalpy flux, respectively. $\boldsymbol{\delta}$ is the identity tensor. Since all Y_i 's sum up to 1 by definition, the continuity equation for the mixture density can be derived by summing up the continuity equations of all species given by Eq. (1) as

$$\frac{\partial \rho}{\partial t} + \nabla \cdot (\rho \mathbf{u}) = 0. \quad (4)$$

The mixture is assumed to be ideal and calorically perfect, with

$$E = \rho \left(e + \frac{1}{2} \mathbf{u} \cdot \mathbf{u} \right), \quad (5)$$

$$p = (\gamma - 1) \rho e, \quad e = c_v T, \quad (6)$$

where e and T are, respectively, specific internal energy and temperature of the mixture. γ and c_v are the ratio of specific heats and the specific heat at a constant volume of the mixture, respectively.

The multicomponent diffusive mass flux of species i is given by [39]

$$\mathbf{J}_i = \rho \frac{M_i}{M^2} \sum_{j=1}^N M_j \tilde{D}_{ij} \nabla X_j, \quad (7)$$

where M_i and X_i are, respectively, the molecular weight and the mole fraction of species i . M is the molecular weight of the mixture, and \tilde{D}_{ij} is the ij th element of the matrix of ordinary multicomponent diffusion coefficients $\tilde{\mathbf{D}}$. The mole fraction of species i is given by

$$X_i = \frac{M}{M_i} Y_i. \quad (8)$$

The multicomponent diffusive mass flux is reduced to Fick's law for a binary mixture:

$$\mathbf{J}_i = -\rho D_i \nabla Y_i, \quad i = 1, 2, \quad (9)$$

where $D_1 = D_2$ is the binary diffusion coefficient. Note that Fick's law is sufficient in this work since only a binary mixture is studied.

The viscous stress tensor $\boldsymbol{\tau}$ for a Newtonian mixture is

$$\boldsymbol{\tau} = 2\mu \mathbf{S} + \left(\mu_v - \frac{2}{3}\mu\right) \delta(\nabla \cdot \mathbf{u}), \quad (10)$$

where μ and μ_v are the shear viscosity and bulk viscosity, respectively, of the mixture. \mathbf{S} is the strain-rate tensor given by

$$\mathbf{S} = \frac{1}{2}[\nabla \mathbf{u} + (\nabla \mathbf{u})^T]. \quad (11)$$

The conductive flux and the interspecies diffusional enthalpy flux [40] are given by

$$\mathbf{q}_c = -\kappa \nabla T, \quad (12)$$

$$\mathbf{q}_d = \sum_{i=1}^N h_i \mathbf{J}_i, \quad (13)$$

where κ is the thermal conductivity of the mixture. h_i is the specific enthalpy of species i :

$$h_i = c_{p,i} T, \quad (14)$$

where $c_{p,i}$ is the specific-heat capacity at constant pressure of species i .

The equations and mixing rules for the fluid properties γ , c_v , $c_{p,i}$, μ , μ_v , κ , and D_i are given in the Appendixes C and D.

III. NUMERICAL METHODS

Three-dimensional numerical experiments with adaptive mesh refinement (AMR) were conducted with the Hydrodynamics Adaptive Mesh Refinement Simulator (HAMeRS) [41] supported with the Structured Adaptive Mesh Refinement Application Infrastructure (SAMRAI) library [42–46] from Lawrence Livermore National Laboratory (LLNL). The convective fluxes of the governing equations are discretized with the explicit form of the sixth-order localized dissipation weighted compact nonlinear scheme (WCNS) [47] for shock-capturing and stabilization of solutions. The accuracy and robustness of the WCNS family for compressible multifluid flows have been demonstrated in previous works [47–49]. Derivatives of diffusive and viscous fluxes are computed with explicit sixth-order finite-difference schemes in nonconservative form. A third-order total variation diminishing Runge-Kutta (RK-TVD) scheme [50] is employed for the time advancement with a convective Courant-Friedrichs-Lewy (CFL) number of 0.5 and a diffusive CFL number of

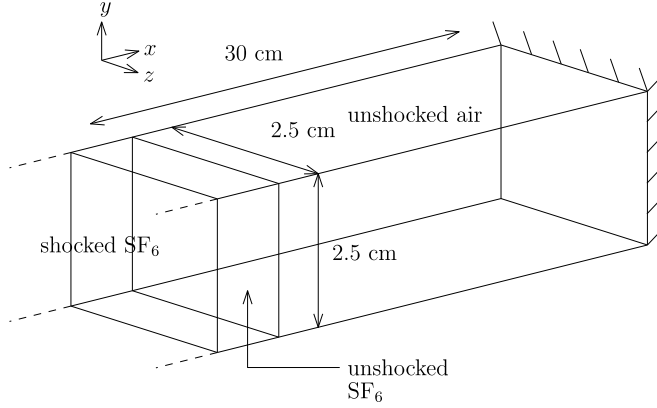


FIG. 1. Schematic diagram of the initial flow field and the computational domain.

0.25. The regions for adaptive mesh refinement are identified with a gradient sensor on the pressure field and a wavelet sensor [51] on the density field to detect shock waves and mixing regions, respectively. An additional sensor based on mass fractions is also used to assist the detection of mixing regions.

IV. INITIAL CONDITIONS AND COMPUTATIONAL DOMAIN

The 3D case setup in our previous paper [38], with physical transport coefficients for the gases considered, is chosen in this work. In this setup, the shock-induced mixing problem is simulated in a numerical shock tube with a cross-sectional area of $2.5 \text{ cm} \times 2.5 \text{ cm}$. A planar shock wave of Mach number $\text{Ma} = 1.45$ is initialized in a sulfur hexafluoride (SF_6) region, with the Rankine-Hugoniot jump conditions to interact with a diffuse interface between SF_6 and air. A multimode perturbation expressed in the following equation is imposed on the interface:

$$S(y, z) = A \sum_m \cos\left(\frac{2\pi m}{L_{yz}}y + \phi_m\right) \cos\left(\frac{2\pi m}{L_{yz}}z + \psi_m\right), \quad (15)$$

where $L_{yz} = 2.5 \text{ cm}$. The perturbation has 11 modes with wave number m between 20 and 30 in each transverse direction. Constant amplitude $A = \sqrt{2} \times 0.01 \text{ mm}$ is used for each mode, and random phase shifts ϕ_m and ψ_m between 0 and 2π are introduced to each mode to prevent summing up of harmonic modes. ϕ_m and ψ_m of each mode are given in the Supplemental Material [52].

The computational domain and initial conditions are shown in Fig. 1. Boundaries are periodic in the transverse directions, and reflective boundary conditions are applied at the end wall. The length of the domain is chosen to be large enough such that no waves leave the open-sided boundary during the simulations. The preshocked gases are stationary initially and have temperature $T = 298 \text{ K}$ and pressure $p = 101\,325 \text{ Pa}$. Table I shows the initial conditions of gases in different portions of the domain. The initial Atwood number $At = (\rho_{\text{SF}_6} - \rho_{\text{air}})/(\rho_{\text{SF}_6} + \rho_{\text{air}})$ across the interface is 0.68.

All simulations start at $t = -0.05 \text{ ms}$, and the shock wave is initially positioned at a location such that the shock-interface interaction first happens at $t = 0$. Since the simulations are initiated in the heavy-light gas setting, the shock wave is transmitted to the light-fluid side and a rarefaction wave is reflected back to the heavy-fluid side. After hitting the wall, the transmitted shock is reflected back toward the interface when it hits the end wall, and this causes the reshock of the interface. Since the shock arrives at the interface from the light-fluid side this time, a transmitted shock and a reflected shock are generated. The reflected shock leads to a second reshock. The end time of the simulations is chosen at $t = 1.75 \text{ ms}$, when the second reshock is just about to happen, as the grid resolution requirements become too large to accurately capture this flow stage. Figure 2 shows the space-time

TABLE I. Initial conditions of the postshock state and the preshock states of the light- and heavy-gas sides.

Quantity	Postshock SF ₆	Preshock SF ₆	Air
ρ (kg m ⁻³)	11.97082	5.972866	1.145601
p (Pa)	218005.4	101325.0	101325.0
T (K)	319.9084	298.0	298.0
u (m s ⁻¹)	98.93441	0	0

$(x-t)$ diagram for different features in a one-dimensional (1D) flow representation. This problem was studied in the previous work [38] with both two-dimensional (2D) and 3D simulations. In this work, results from a higher-resolution 3D AMR simulation are studied for the second-moment analysis of the shock-induced variable-density instability and turbulence.

V. TRANSPORT EQUATIONS OF THE SECOND MOMENTS

To get a statistical view of a chaotic or turbulent field, it is a common practice to ensemble average the governing equations. The conserved variables are decomposed into ensemble means and fluctuations through Reynolds decomposition. The Reynolds decomposition of an arbitrary variable, f , rewrites the variable as

$$f = \bar{f} + f', \quad (16)$$

where \bar{f} and f' are the mean and fluctuation of f , respectively. If the flow has homogeneous directions and the widths of the domain in the homogeneous directions are sufficiently larger than the length scales of turbulent features, one can estimate the ensemble mean with the mean over all

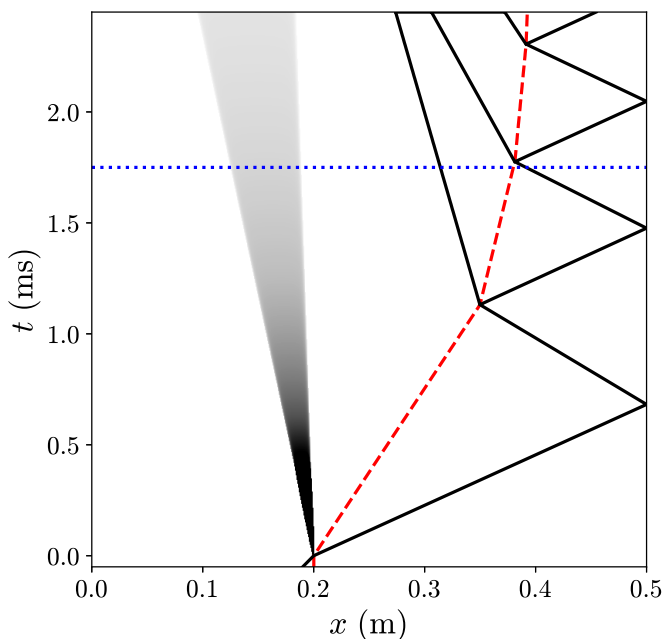


FIG. 2. $x-t$ diagram showing the propagation of material interface, shock waves, and rarefaction. Red dashed line: material interface; black lines: shock waves; gray region: rarefaction. The blue dotted line indicates the end time of the simulations.

homogeneous directions. For variable-density flows, after averaging the conserved variables of the governing equations, it is natural to see the Favre-averaged (density-weighted-averaged) quantities. The Favre decomposition is given by

$$f = \tilde{f} + f'', \quad (17)$$

where $\tilde{f} = \overline{\rho f} / \bar{\rho}$. The Reynolds and Favre averages of the velocity are related with

$$\tilde{u}_i = \bar{u}_i + a_i, \quad (18)$$

where $a_i = \overline{\rho' u'_i} / \bar{\rho}$ is the velocity associated with the turbulent mass flux $\bar{\rho} a_i$. The fluctuation, u'_i , and the Favre fluctuation, u''_i , have a similar relation to the averages:

$$u''_i = u'_i - a_i. \quad (19)$$

If we apply averaging on the continuity equation and the conservative transport equation of momentum given by Eqs. (4) and (2), respectively, we obtain

$$\frac{\partial \bar{\rho}}{\partial t} + \frac{\partial (\bar{\rho} \tilde{u}_k)}{\partial x_k} = 0, \quad (20)$$

$$\frac{\partial (\bar{\rho} \tilde{u}_i)}{\partial t} + \frac{\partial (\bar{\rho} \tilde{u}_k \tilde{u}_i)}{\partial x_k} = - \frac{\partial (\bar{\rho} \delta_{ki})}{\partial x_k} + \frac{\partial \bar{\tau}_{ki}}{\partial x_k} - \frac{\partial (\bar{\rho} \tilde{R}_{ki})}{\partial x_k}, \quad (21)$$

where \tilde{R}_{ij} is the Favre-averaged Reynolds stress tensor given by

$$\tilde{R}_{ij} = \frac{\overline{\rho u'_i u'_j}}{\bar{\rho}}. \quad (22)$$

The Favre-averaged Reynolds stress tensor appears as an unclosed term in the Favre-averaged transport equation of momentum. The development of the Favre-averaged Reynolds stress can be studied through its transport equations given by Besnard *et al.* [18]:

$$\begin{aligned} \underbrace{\frac{\partial \bar{\rho} \tilde{R}_{ij}}{\partial t}}_{\text{term (I)}} + \underbrace{\frac{\partial (\bar{\rho} \tilde{u}_k \tilde{R}_{ij})}{\partial x_k}}_{\text{term (II)}} &= \underbrace{a_i \left(\frac{\partial \bar{\rho}}{\partial x_j} - \frac{\partial \bar{\tau}_{jk}}{\partial x_k} \right) + a_j \left(\frac{\partial \bar{\rho}}{\partial x_i} - \frac{\partial \bar{\tau}_{ik}}{\partial x_k} \right) - \bar{\rho} \tilde{R}_{ik} \frac{\partial \tilde{u}_j}{\partial x_k} - \bar{\rho} \tilde{R}_{jk} \frac{\partial \tilde{u}_i}{\partial x_k}}_{\text{term (III)}} \\ &\quad - \underbrace{\frac{\partial (\overline{\rho u'_i u'_j u'_k})}{\partial x_k} - \frac{\partial (\overline{u'_i p'})}{\partial x_j} - \frac{\partial (\overline{u'_j p'})}{\partial x_i} + \frac{\partial (\overline{u'_i \tau'_{jk}})}{\partial x_k} + \frac{\partial (\overline{u'_j \tau'_{ik}})}{\partial x_k}}_{\text{term (IV)}} \\ &\quad + \underbrace{p' \frac{\partial u'_i}{\partial x_j} + p' \frac{\partial u'_j}{\partial x_i}}_{\text{term (V)}} - \underbrace{\overline{\tau'_{jk} \frac{\partial u'_i}{\partial x_k}} - \overline{\tau'_{ik} \frac{\partial u'_j}{\partial x_k}}}_{\text{term (VI)}}, \end{aligned} \quad (23)$$

where the left-hand side consists of the rate of change [term (I)] and convection [term (II)]. The right-hand side consists of production [term (III)], turbulent transport [term (IV)], pressure-strain redistribution [term (V)], and dissipation [term (VI)].

In the paper by Schwarzkopf *et al.* [21], Favre decomposition is used for the viscous stress in the Favre-averaged Reynolds stress transport equation instead of Reynolds decomposition. However, we follow the original work by Besnard *et al.* [18] to use Reynolds decomposition for the viscous stress as we believe Favre decomposition should only be applied in the advective or convective terms. The Reynolds decomposition of the viscous stress was also employed in the DNS analysis of Livescu *et al.* [53], which was later used to refine the model by Schwarzkopf *et al.* [22]. Besides, the dissipation term with Reynolds decomposition on viscous stress in the turbulent kinetic energy transport equation can be proved to be strictly negative if both shear and bulk viscosities are uniform

in the domain, while that with Favre decomposition on viscous stress cannot be proved to be strictly negative. Also, note that with the relation given by Eq. (19),

$$\frac{\partial(\overline{u'_i p'})}{\partial x_j} = \frac{\partial(\overline{u'_i p'})}{\partial x_j}, \quad (24)$$

$$\frac{\partial(\overline{u'_i \tau'_{jk}})}{\partial x_k} = \frac{\partial(\overline{u'_i \tau'_{jk}})}{\partial x_k}, \quad (25)$$

$$p' \frac{\partial u'_i}{\partial x_j} = p' \frac{\partial u''_i}{\partial x_j}, \quad (26)$$

$$\tau'_{jk} \frac{\partial u'_i}{\partial x_k} = \tau'_{jk} \frac{\partial u''_i}{\partial x_k}. \quad (27)$$

The relations above are commonly used to interchange terms in the transport equations of \tilde{R}_{ij} and k in many previous studies.

In flows where the mean is 1D, such as the numerical experiment being studied in this work (where the y and z directions are homogeneous), the transport equation of \tilde{R}_{11} can be simplified to

$$\begin{aligned} \underbrace{\frac{\partial \tilde{\rho} \tilde{R}_{11}}{\partial t}}_{\text{term (I)}} + \underbrace{\frac{\partial(\tilde{\rho} \tilde{u} \tilde{R}_{11})}{\partial x}}_{\text{term (II)}} &= 2a_1 \left(\frac{\partial \tilde{p}}{\partial x} - \frac{\partial \tilde{\tau}_{11}}{\partial x} \right) - 2\tilde{\rho} \tilde{R}_{11} \frac{\partial \tilde{u}}{\partial x} - \underbrace{\frac{\partial(\overline{\rho u'' u'' u''})}{\partial x} - 2 \frac{\partial(\overline{u' p'})}{\partial x} + 2 \frac{\partial(\overline{u' \tau'_{11}})}{\partial x}}_{\text{term (IV)}} \\ &+ \underbrace{2p' \frac{\partial u'}{\partial x}}_{\text{term (V)}} - 2 \underbrace{\left(\overline{\tau'_{11} \frac{\partial u'}{\partial x}} + \overline{\tau'_{12} \frac{\partial u'}{\partial y}} + \overline{\tau'_{13} \frac{\partial u'}{\partial z}} \right)}_{\text{term (VI)}}. \end{aligned} \quad (28)$$

The transport equation of \tilde{R}_{22} for 1D mean flow can be reduced to

$$\underbrace{\frac{\partial \tilde{\rho} \tilde{R}_{22}}{\partial t}}_{\text{term (I)}} + \underbrace{\frac{\partial(\tilde{\rho} \tilde{u} \tilde{R}_{22})}{\partial x}}_{\text{term (II)}} = - \underbrace{\frac{\partial(\overline{\rho v'' v'' u''})}{\partial x}}_{\text{term (IV)}} + 2 \underbrace{\frac{\partial(\overline{v' \tau'_{21}})}{\partial x}}_{\text{term (V)}} + \underbrace{2p' \frac{\partial v'}{\partial y}}_{\text{term (V)}} - 2 \underbrace{\left(\overline{\tau'_{21} \frac{\partial v'}{\partial x}} + \overline{\tau'_{22} \frac{\partial v'}{\partial y}} + \overline{\tau'_{23} \frac{\partial v'}{\partial z}} \right)}_{\text{term (VI)}}. \quad (29)$$

Note that there is no production term [term (III)] in the transport equation of \tilde{R}_{22} . The transport equation of \tilde{R}_{33} is similar. In the present flow, the Reynolds shear stress components, \tilde{R}_{12} , \tilde{R}_{13} , and \tilde{R}_{23} , are statistically zero due to the homogeneity of the problem in the transverse directions.

The transport equation of the turbulent kinetic energy per unit mass, $k = \tilde{R}_{ii}/2$, can be simply obtained by taking half of the trace of the Reynolds stress tensor transport equation. For 1D mean flow, it has the following form:

$$\begin{aligned} \underbrace{\frac{\partial \tilde{\rho} k}{\partial t}}_{\text{term (I)}} + \underbrace{\frac{\partial(\tilde{\rho} \tilde{u} k)}{\partial x}}_{\text{term (II)}} &= a_1 \left(\frac{\partial \tilde{p}}{\partial x} - \frac{\partial \tilde{\tau}_{11}}{\partial x} \right) - \tilde{\rho} \tilde{R}_{11} \frac{\partial \tilde{u}}{\partial x} - \underbrace{\frac{1}{2} \frac{\partial(\overline{\rho u'_i u'_i u''})}{\partial x} - \frac{\partial(\overline{u' p'})}{\partial x} + \frac{\partial(\overline{u'_i \tau'_{i1}})}{\partial x}}_{\text{term (IV)}} \\ &+ \underbrace{p' \frac{\partial u'_i}{\partial x_i}}_{\text{term (V)}} - \underbrace{\tau'_{ij} \frac{\partial u'_i}{\partial x_j}}_{\text{term (VI)}}, \end{aligned} \quad (30)$$

where the LHS consists of the rate of change [term (I)] and convection [term (II)]. The RHS consists of production [term (III)], turbulent transport [term (IV)], the pressure-dilatation [term (V)], and dissipation [term (VI)]. Note that the production term represents the energy transfer rate between the mean kinetic energy and the turbulent kinetic energy, and it can have a negative sign.

The velocity associated with the turbulent mass flux, a_i , in the mean flow pressure gradient terms only appears in variable-density or/and compressible flows. It is an important term for understanding the energetics in these kinds of flows, as the mean pressure gradient multiplied by it is the agent for the transfer of mean kinetic energy into turbulent kinetic energy. Correct modeling of a_i can also help us close the Reynolds stress transport equations. The transport equation of turbulent mass flux $\bar{\rho}a_i$ is given by [18]

$$\underbrace{\frac{\partial(\bar{\rho}a_i)}{\partial t}}_{\text{term (I)}} + \underbrace{\frac{\partial(\bar{\rho}\tilde{u}_k a_i)}{\partial x_k}}_{\text{term (II)}} = \underbrace{b\left(\frac{\partial\bar{p}}{\partial x_i} - \frac{\partial\bar{\tau}_{ki}}{\partial x_k}\right) - \tilde{R}_{ik}\frac{\partial\bar{p}}{\partial x_k}}_{\text{term (III)}} + \underbrace{\bar{\rho}\frac{\partial(a_k a_i)}{\partial x_k} - \bar{\rho}a_k\frac{\partial\bar{u}_i}{\partial x_k}}_{\text{term (IV)}} - \underbrace{\bar{\rho}\frac{\partial(\overline{\rho'u'_i u'_k}/\bar{\rho})}{\partial x_k}}_{\text{term (V)}} + \underbrace{\bar{\rho}\left(\frac{1}{\rho}\right)'\left(\frac{\partial p'}{\partial x_i} - \frac{\partial\tau'_{ik}}{\partial x_k}\right) + \bar{\rho}\varepsilon_{a_i}}_{\text{term (VI)}}, \quad (31)$$

where the LHS consists of the rate of change [term (I)] and convection [term (II)]. The RHS contains production [term (III)], redistribution [term (IV)], the turbulent transport [term (V)], and destruction [term (VI)]. Also,

$$\varepsilon_{a_i} = -\overline{u'_i \frac{\partial u'_k}{\partial x_k}}. \quad (32)$$

Note that ε_{a_i} is ignored in the work by Besnard *et al.* [18] and in many turbulence models. However, ε_{a_i} was shown to be non-negligible at early times in the evolution of constant acceleration RTI [53]. Here, it is also found that ε_{a_i} is significant in the budgets at different times before reshock for the flow being studied in this work.

For 1D mean flow, the transport equation of $\bar{\rho}a_1$ can be simplified to

$$\underbrace{\frac{\partial(\bar{\rho}a_1)}{\partial t}}_{\text{term (I)}} + \underbrace{\frac{\partial(\bar{\rho}\bar{u}a_1)}{\partial x}}_{\text{term (II)}} = \underbrace{b\left(\frac{\partial\bar{p}}{\partial x} - \frac{\partial\bar{\tau}_{11}}{\partial x}\right) - \tilde{R}_{11}\frac{\partial\bar{p}}{\partial x}}_{\text{term (III)}} + \underbrace{\bar{\rho}\frac{\partial(a_1 a_1)}{\partial x} - \bar{\rho}a_1\frac{\partial\bar{u}}{\partial x}}_{\text{term (IV)}} - \underbrace{\bar{\rho}\frac{\partial(\overline{\rho'u'u'}/\bar{\rho})}{\partial x}}_{\text{term (V)}} + \underbrace{\bar{\rho}\left(\frac{1}{\rho}\right)'\left(\frac{\partial p'}{\partial x} - \frac{\partial\tau'_{11}}{\partial x} - \frac{\partial\tau'_{12}}{\partial y} - \frac{\partial\tau'_{13}}{\partial z}\right) + \bar{\rho}\varepsilon_{a_1}}_{\text{term (VI)}}. \quad (33)$$

Note that a_2 and a_3 for 1D mean flow are statistically equal to zero. The density-specific-volume covariance, $b = -\overline{\rho'(1/\rho)'}$, mediates the turbulent mass flux production mechanism. The component of the production term, $b\bar{p}_{,1}$, is crucial to the prediction of the rate of change of turbulent mass flux and requires the modeling of b .

The transport equation of b was first derived by Besnard *et al.* [18] in the following advection form with the Reynolds-averaged velocity:

$$\frac{\partial b}{\partial t} + \bar{u}_k b_{,k} = -\frac{b+1}{\bar{\rho}}(\bar{\rho}a_k)_{,k} - \bar{\rho}\left(\left(\frac{1}{\rho}\right)'u'_k\right)_{,k} - 2\bar{\rho}\varepsilon_b, \quad (34)$$

where

$$\varepsilon_b = \overline{\left(\frac{1}{\rho}\right)' \frac{\partial u'_k}{\partial x_k}}. \quad (35)$$

TABLE II. Different grids used for the grid sensitivity study. Three levels of grids with 1:8 overall refinement ratio are used in all cases.

Grid	Base grid resolution	Refinement ratios	Finest grid spacing (μm)
B	$640 \times 32 \times 32$	1:2, 1:4	97.7
C	$1280 \times 64 \times 64$	1:2, 1:4	48.8
D	$2560 \times 128 \times 128$	1:2, 1:4	24.4
E	$5120 \times 256 \times 256$	1:2, 1:4	12.2

In Ref. [21], the transport equation of $\bar{\rho}b$ in the conservative form is derived from Eq. (34) with the averaged mixture continuity equation [Eq. (4)] as

$$\underbrace{\frac{\partial \bar{\rho}b}{\partial t}}_{\text{term (I)}} + \underbrace{\frac{\partial(\bar{\rho}\tilde{u}_k b)}{\partial x_k}}_{\text{term (II)}} = \underbrace{-2(b+1)a_k \frac{\partial \bar{\rho}}{\partial x_k}}_{\text{term (III)}} + \underbrace{+2\bar{\rho}a_k \frac{\partial b}{\partial x_k}}_{\text{term (IV)}} + \underbrace{+\bar{\rho}^2 \frac{\partial(\overline{(\rho'(1/\rho)'u'_k/\bar{\rho})})}{\partial x_k}}_{\text{term (V)}} + \underbrace{+2\bar{\rho}^2 \varepsilon_b}_{\text{term (VI)}}, \quad (36)$$

where the left-hand side consists of the rate of change [term (I)] and convection [term (II)]. The right-hand side consists of production [term (III)], redistribution [term (IV)], turbulent transport [term (V)], and destruction [term (VI)]. For 1D mean flow, the transport equation of $\bar{\rho}b$ can be simplified to

$$\underbrace{\frac{\partial(\bar{\rho}b)}{\partial t}}_{\text{term (I)}} + \underbrace{\frac{\partial(\bar{\rho}\tilde{u}b)}{\partial x}}_{\text{term (II)}} = \underbrace{-2(b+1)a_1 \frac{\partial \bar{\rho}}{\partial x}}_{\text{term (III)}} + \underbrace{+2\bar{\rho}a_1 \frac{\partial b}{\partial x}}_{\text{term (IV)}} + \underbrace{+\bar{\rho}^2 \frac{\partial(\overline{(\rho'(1/\rho)'u'/\bar{\rho})})}{\partial x}}_{\text{term (V)}} + \underbrace{+2\bar{\rho}^2 \varepsilon_b}_{\text{term (VI)}}. \quad (37)$$

The transport equation of $\bar{\rho}b$ in conservative form shown above instead of that in advection form is studied in this work. Advection form of the b transport equation was considered in the DNS analysis of Livescu *et al.* [53].

VI. GRID SENSITIVITY ANALYSIS

In this section, the quality of the simulations is studied through a grid sensitivity analysis. Table II shows the grid settings used for the problem. There are a total of three levels of grids with two levels of mesh refinement in all grid settings. The refinement ratios in each direction from the base level to the second level and from the second level to the finest level are 1:2 and 1:4, respectively. Four different grid settings are tested, with the number of grid points in the transverse directions increasing from 32 points (grid B) to 256 points (grid E) on the base level. The finest level for the largest mesh resolution case has a grid spacing of 12.2 μm . With this grid spacing, there are around 68 grid points across the smallest wavelength among the initial modes. The 3D simulations with grids B–D were first presented in [38], but the new simulation using the grid E settings presented here is a higher grid resolution compared to those runs and provides more accurate statistical results. This ultrahigh resolution simulation has cell counts surpassing 4.5 billion, as shown in Appendix B. Figure 3 presents visualizations of the mixing layer at different times with grid E.

The grid sensitivities of the integral mixing width W and the domain-integrated quantities of interest ($\bar{\rho}a_1$, $\bar{\rho}b$, $\bar{\rho}\tilde{R}_{11}$, $\bar{\rho}\tilde{R}_{22}$, $\bar{\rho}\tilde{R}_{33}$, and $\bar{\rho}k$) in the transport equations of second moment quantities are examined in this section. The mixing width is defined as

$$W = \int 4\bar{X}_{\text{SF}_6}(1 - \bar{X}_{\text{SF}_6})dx. \quad (38)$$

The mixing width estimates the characteristic length of the mixing layer due to the entrainment of the fluids. Note that since $\bar{\rho}\tilde{R}_{22}$ and $\bar{\rho}\tilde{R}_{33}$ are statistically identical, the grid sensitivity of $\bar{\rho}(\tilde{R}_{22} + \tilde{R}_{33})/2$ is studied instead.

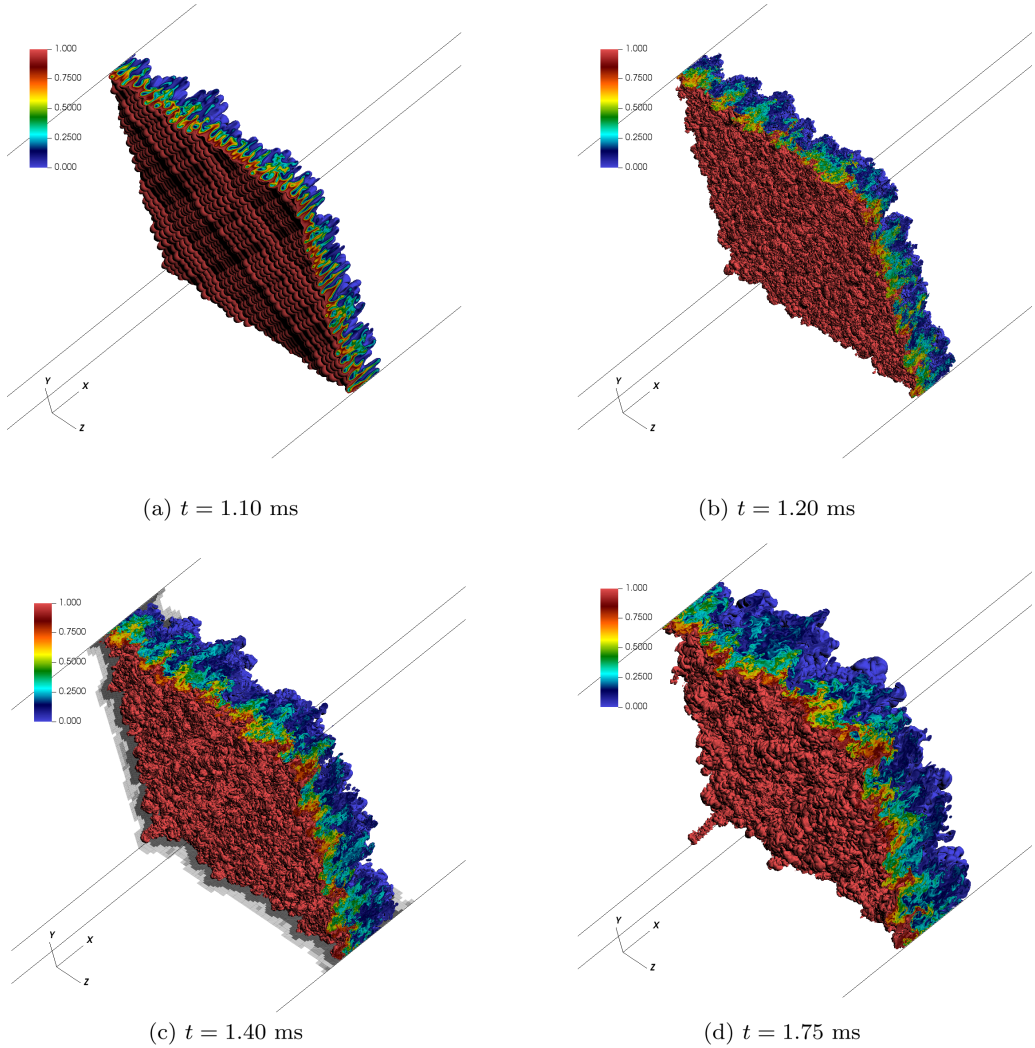


FIG. 3. Isovolumes of the SF_6 mole fraction, X_{SF_6} , at different times in the numerical shock tube with grid E. The colorbar indicates the value of X_{SF_6} . The first and second (last) refinement levels of the AMR grid are shown on the side walls of the domain for the plot at $t = 1.40$ ms.

Figure 4 compares the time evolution of the statistical quantities computed on different grids. From the figure, it can be seen that mixing width, integrals of $\bar{\rho}a_1$, $\bar{\rho}b$, and $\bar{\rho}\tilde{R}_{11}$ are well grid-converged for the entire simulation with the highest resolution grid. The grid sensitivity of the integral of $\bar{\rho}(\tilde{R}_{22} + \tilde{R}_{33})/2$ is higher than other quantities before reshock, but its contribution to the integral of turbulent kinetic energy, $\bar{\rho}k$, is an order of magnitude smaller than that of $\bar{\rho}\tilde{R}_{11}$. Thus, the integral of $\bar{\rho}k$ is also grid-converged reasonably well at all times. The grid sensitivities of the spatial profiles of these second moments including the turbulent kinetic energy at different times are also observed to be small between the grid D and the grid E, which are shown in Appendix A.

As the statistical quantities of interest computed on the finest resolution grid (grid E) show very small grid sensitivity throughout the simulation when compared with those from the next finest resolution grid (grid D), only results from grid E are presented and discussed in the remaining sections.

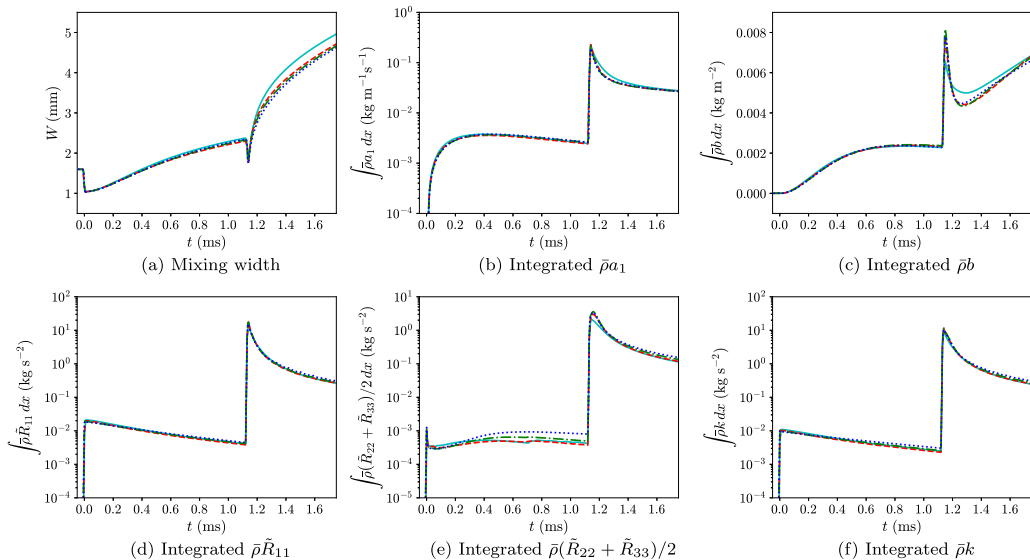


FIG. 4. Grid sensitivities of mixing width and second moment statistics. Cyan solid line: grid B; red dashed line: grid C; green dash-dotted line: grid D; blue dotted line: grid E.

VII. ANALYSIS OF THE SECOND MOMENTS

The importance of the second moments— $\bar{\rho}a_1$, $\bar{\rho}b$, $\bar{\rho}\tilde{R}_{11}$, $\bar{\rho}\tilde{R}_{22}$, and $\bar{\rho}\tilde{R}_{33}$ —to close the Favre-averaged momentum equation for the mixture is discussed earlier. In this section, the time evolution of the spatial profiles of different second moments including the Favre-averaged Reynolds stress and the turbulent kinetic energy is studied in detail, with an examination on their asymmetry due to the variable-density or non-Boussinesq effects.

At each impulsive acceleration such as at first shock and reshock, the advection velocity of the mixing layer changes abruptly. However, the advection speed of the mixing layer between impulsive accelerations is essentially constant in time and is close to that given by the solutions of the 1D flow representation, U_i . Besides, the mean velocity across the mixing layer is observed to be quite uniform. Therefore, in a moving reference frame with speed U_i relative to the simulation reference frame, $\bar{u} \approx 0$ and $\tilde{u} \approx a_1$ statistically. All of the 1D spatial profiles of the second moments discussed in this section are plotted in the moving frame of the mixing layer with the \tilde{x} coordinate system. In other words, the x coordinate is shifted as

$$\tilde{x}(x, t) = x - x_i(t), \quad (39)$$

where x_i is the location of the interface from the solutions of the 1D flow representation.

A. Mean density and turbulent mass flux

The mean density profiles at different times in the moving frame of the mixing layer are shown in Fig. 5. The density profiles are asymmetric where the spikes penetrate into the lighter fluid more than the bubbles into the heavier fluid due to variable-density effects that are also observed in RTI [53,54]. The density profiles become wider over time after first shock and reshock due to the mixing caused by the RMI. While not shown here, the density profiles collapse reasonably well at late times after both first shock and reshock when they are normalized with the mixing width W , similar to RTI [53]. A similar collapse for the mole fraction profiles was also reported in our previous RMI work [38].

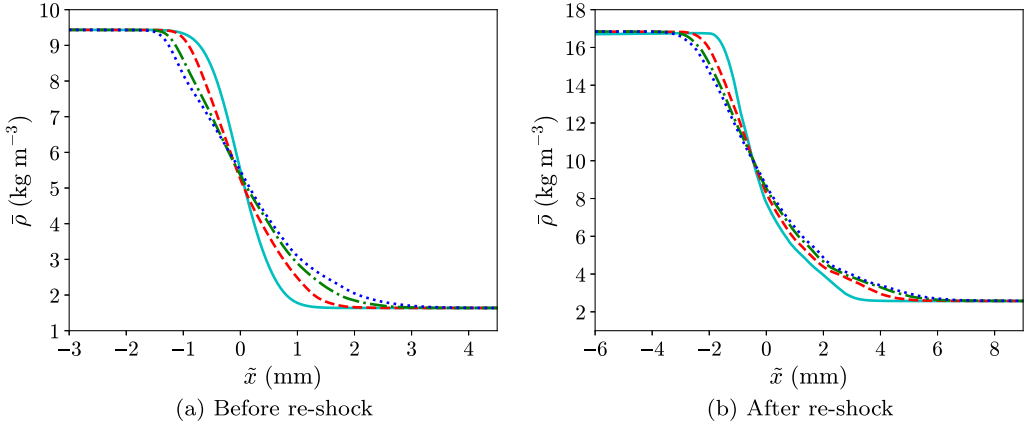


FIG. 5. Profiles of the mean density, $\bar{\rho}$, at different times. Cyan solid line in (a): $t = 0.05$ ms; red dashed line in (a): $t = 0.40$ ms; green dash-dotted line in (a): $t = 0.75$ ms; blue dotted line in (a): $t = 1.10$ ms. Cyan solid line in (b): $t = 1.20$ ms; red dashed line in (b): $t = 1.40$ ms; green dash-dotted line in (b): $t = 1.60$ ms; blue dotted line in (b): $t = 1.75$ ms.

Figure 6 compares the profiles of $\bar{\rho}a_1$ at different times before and after reshock. The study of turbulent mass flux, $\bar{\rho}a_1$, and the velocity associated with turbulent mass flux, a_1 , is very important for understanding variable-density effects in the current problem and modeling similar types of flows. The turbulent mass flux determines the growth of the Favre-averaged Reynolds stress and turbulent kinetic energy in variable-density flows and is studied in previous works on RMI [55–57], RTI [53,54,58], and buoyancy-driven variable-density turbulence [59]. From the figure, it can be seen that there is a sudden rise in $\bar{\rho}a_1$, followed by its decay after each shock event. The jump in the magnitude of $\bar{\rho}a_1$ is caused by the large amount of energy injected at the mixing layer at each impulsive acceleration. The profiles of $\bar{\rho}a_1$ are asymmetric and have longer tails on the light fluid side. It can also be noticed that at late times after first shock and reshock, $\bar{\rho}a_1$ peaks at a position slightly toward the heavier fluid side (slightly negative \tilde{x}). This suggests that there is a fixed point at the same location in the mean density profiles at late times, which can be deduced from Eq. (20).

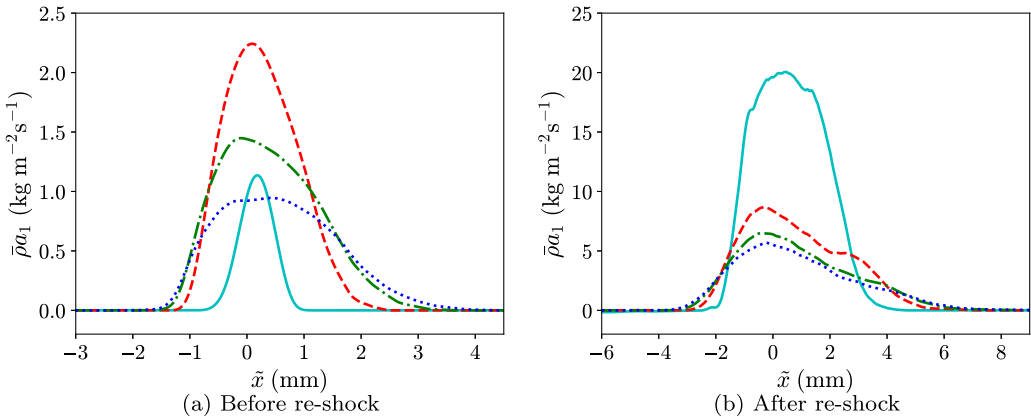


FIG. 6. Profiles of the turbulent mass flux component in the streamwise direction, $\bar{\rho}a_1$, at different times. Cyan solid line in (a): $t = 0.05$ ms; red dashed line in (a): $t = 0.40$ ms; green dash-dotted line in (a): $t = 0.75$ ms; blue dotted line in (a): $t = 1.10$ ms. Cyan solid line in (b): $t = 1.20$ ms; red dashed line in (b): $t = 1.40$ ms; green dash-dotted line in (b): $t = 1.60$ ms; blue dotted line in (b): $t = 1.75$ ms.

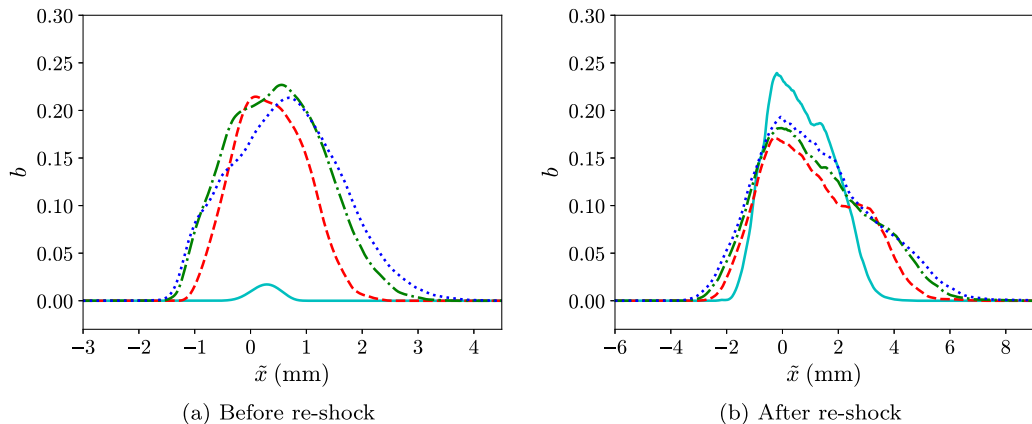


FIG. 7. Profiles of the density-specific-volume covariance, b , at different times. Cyan solid line in (a): $t = 0.05$ ms; red dashed line in (a): $t = 0.40$ ms; green dash-dotted line in (a): $t = 0.75$ ms; blue dotted line in (a): $t = 1.10$ ms. Cyan solid line in (b): $t = 1.20$ ms; red dashed line in (b): $t = 1.40$ ms; green dash-dotted line in (b): $t = 1.60$ ms; blue dotted line in (b): $t = 1.75$ ms.

The fixed point can be seen and verified from the mean density profiles shown in Fig. 5. A fixed point in mean density profiles was also observed in RTI [53].

B. Density-specific-volume covariance

The density-specific-volume covariance b mediates the turbulent mass flux production mechanism. It can also be viewed as a metric for the homogeneity of mixing. b is a non-negative quantity, and $b = 0$ corresponds to fluids that are homogeneously mixed. On the contrary, a high value of b indicates inhomogeneous mixing of the fluids. This statistical quantity was extensively studied in many previous investigations on RMI [56,60–66] and also RTI [53]. Figure 7 displays the profiles of b at different times before and after reshock. The shapes of b have a single peak and are asymmetric at different times due to the variable-density or non-Boussinesq effects. The shapes have longer tails on the lighter fluid side at all times. Before reshock, the peak appears to be on the lighter fluid side at late times, but the peak shifts to the heavier fluid side after reshock. It can be seen that the peak of b at late times after first shock and reshock remains quite stationary. This slow rate of change in the magnitude of b at late times was also observed in the RMI experiments by Balasubramanian *et al.* [60] and Tomkins *et al.* [62] after incident shock and reshock, respectively, and RMI simulations by Tritschler *et al.* [64] after reshock. Similar late-time behavior was also seen in the RTI simulations by Livescu *et al.* [53].

b can also be expressed as a sum of a series of density probability density function (PDF) moments [67]:

$$b = \frac{\overline{\rho'^2}}{\bar{\rho}^2} \left[1 - i_\rho \frac{\overline{\rho'^3}}{(\overline{\rho'^2})^{3/2}} + i_\rho^2 \frac{\overline{\rho'^4}}{(\overline{\rho'^2})^2} - i_\rho^3 \frac{\overline{\rho'^5}}{(\overline{\rho'^2})^{5/2}} + \dots \right], \quad (40)$$

where $i_\rho = (\overline{\rho'^2})^{1/2}/\bar{\rho}$. If i_ρ is very small, the equation reduces to the Boussinesq relation:

$$b \approx \frac{\overline{\rho'^2}}{\bar{\rho}^2}. \quad (41)$$

The ratio of the left-hand side (density-specific-volume covariance) and the right-hand side (square of density intensity) of Eq. (41) can be used to test the Boussinesq approximation, where the corresponding component in turbulent mass flux production can be approximated with density

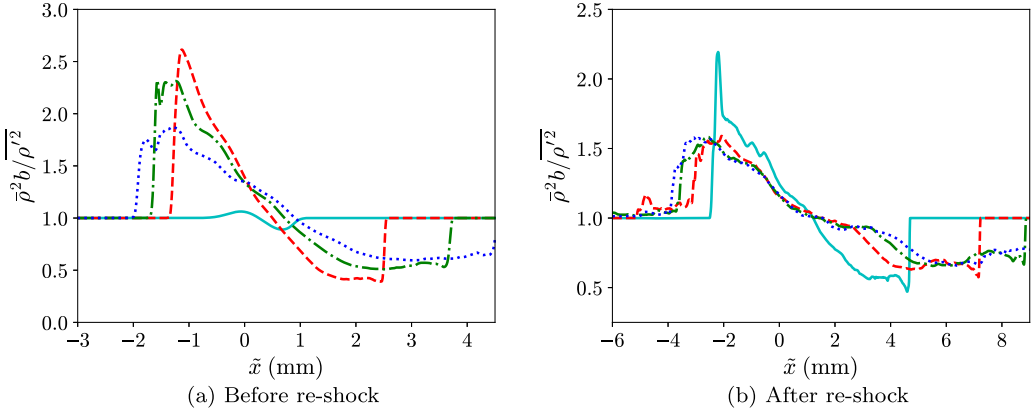


FIG. 8. Profiles of the ratio of the density-specific-volume covariance to the square of density intensity at different times. Cyan solid line in (a): $t = 0.05$ ms; red dashed line in (a): $t = 0.40$ ms; green dash-dotted line in (a): $t = 0.75$ ms; blue dotted line in (a): $t = 1.10$ ms. Cyan solid line in (b): $t = 1.20$ ms; red dashed line in (b): $t = 1.40$ ms; green dash-dotted line in (b): $t = 1.60$ ms; blue dotted line in (b): $t = 1.75$ ms.

variance instead of b . The Boussinesq approximation is valid when the ratio is close to 1. Figure 8 shows the variations in the ratio across the mixing region at different times. It can be seen that the ratio varies from 0.5 to 2.5. The ratio is, in general, larger than 1 on the heavier fluid side and smaller than 1 on the lighter fluid side, because of the skewness of the density field. The peaks are located at the edges of the mixing layers, which indicates that variable-density effects are larger at the edges than at the central part of the mixing layer. The same behavior is also observed in the spherical RMI simulations by Lombardini *et al.* [65] with essentially the same Atwood number and the planar RTI simulations by Livescu *et al.* [53] with slightly smaller Atwood number ($At = 0.5$). As a result, Boussinesq equations would lead to an underestimation of the energy conversion rate on the heavier fluid side and an overestimation on the lighter fluid side for high Atwood number flows. A grid sensitivity analysis of the profiles of the ratio at different times is given in the Supplemental Material [52]. The analysis shows that the differences of the profiles between the grid D and the grid E at different times are minor.

C. Favre-averaged Reynolds stress and turbulent kinetic energy

The Favre-averaged Reynolds stress tensor, \tilde{R}_{ij} , appears as an unclosed term in the averaged transport equation of momentum given by Eq. (21). Figures 9 and 10, respectively, show the profiles of Favre-averaged Reynolds normal stress components in the streamwise and transverse directions at different times. Immediately after first shock, there is generation of the Favre-averaged Reynolds normal stress in the mixing region. However, the Favre-averaged Reynolds normal stress component in the streamwise direction is much larger than those in the transverse directions at that instance. As time advances, the ratios of the component in the streamwise direction to those in the transverse directions decrease, but the Reynolds normal stress fields are still very anisotropic at the moment just before reshock. The streamwise Favre-averaged Reynolds normal stress component peaks at the lighter fluid side because of smaller inertia to entrain the fluid from nonlinear convection. After re-shock, the Favre-averaged Reynolds normal stress fields become more isotropic, but there is still more contribution to the turbulent kinetic energy from the streamwise Reynolds normal stress component until the end of simulation. The comparison of different Favre-averaged Reynolds stress components is shown in Fig. 11. All Reynolds shear stress components should be statistically zero, but Fig. 11 shows that the Reynolds shear stress components are not absolutely zero. This is due to

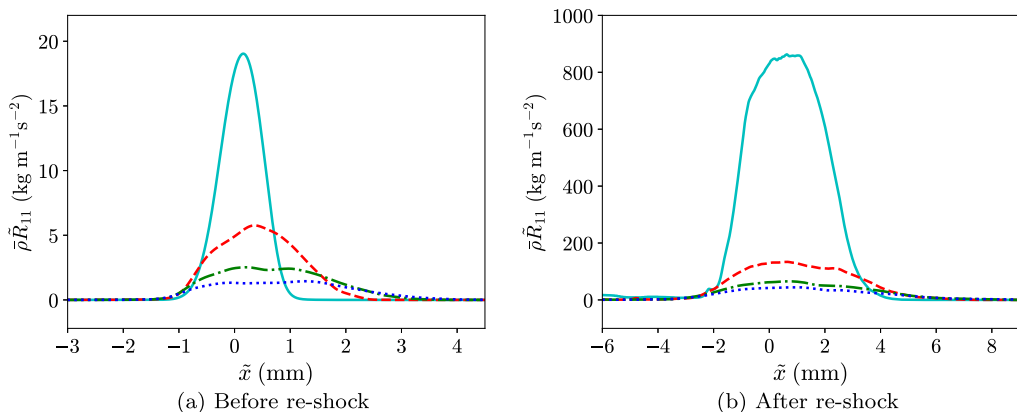


FIG. 9. Profiles of the Reynolds normal stress component in the streamwise direction multiplied by the mean density, $\bar{\rho}\tilde{R}_{11}$, at different times. Cyan solid line in (a): $t = 0.05$ ms; red dashed line in (a): $t = 0.40$ ms; green dash-dotted line in (a): $t = 0.75$ ms; blue dotted line in (a): $t = 1.10$ ms. Cyan solid line in (b): $t = 1.20$ ms; red dashed line in (b): $t = 1.40$ ms; green dash-dotted line in (b): $t = 1.60$ ms; blue dotted line in (b): $t = 1.75$ ms.

some lack of full statistical convergence, but the values are all negligible compared to the Reynolds normal stress components.

The Favre-averaged Reynolds stress \tilde{R}_{ij} can be decomposed as

$$\tilde{R}_{ij} = \frac{\overline{\rho u'_i u'_j}}{\bar{\rho}} - a_i a_j = \underbrace{\overline{u'_i u'_j}}_{\text{term (I)}} + \underbrace{\frac{\overline{\rho' u'_i u'_j}}{\bar{\rho}}}_{\text{term (II)}} - \underbrace{a_i a_j}_{\text{term (III)}},$$

where term (I), $\overline{u'_i u'_j}$, is the definition of the Reynolds stress tensor for single-species incompressible flows. This decomposition is commonly found in previous papers on RMI, such as [55,66,68]. Figure 12 compares the contributions of different terms to \tilde{R}_{11} at different times. We can see from the

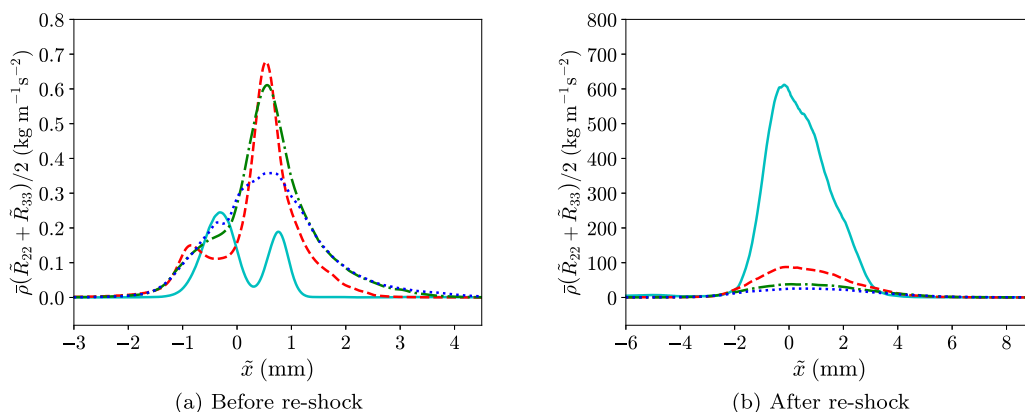


FIG. 10. Profiles of the Reynolds normal stress component in the transverse directions multiplied by the mean density, $\bar{\rho}(\tilde{R}_{22} + \tilde{R}_{33})/2$, at different times. Cyan solid line in (a): $t = 0.05$ ms; red dashed line in (a): $t = 0.40$ ms; green dash-dotted line in (a): $t = 0.75$ ms; blue dotted line in (a): $t = 1.10$ ms. Cyan solid line in (b): $t = 1.20$ ms; red dashed line in (b): $t = 1.40$ ms; green dash-dotted line in (b): $t = 1.60$ ms; blue dotted line in (b): $t = 1.75$ ms.

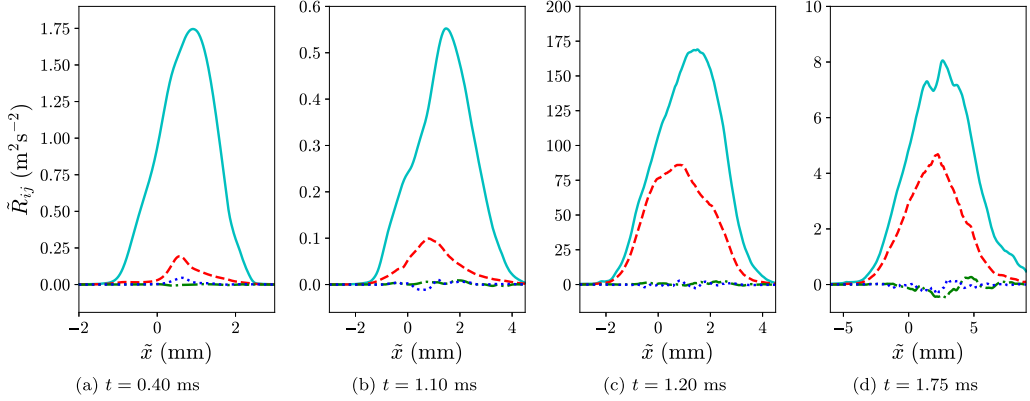


FIG. 11. Comparison of the Reynolds stress components multiplied by the mean density at different times. Cyan solid line: \tilde{R}_{11} ; red dashed line: $(\tilde{R}_{22} + \tilde{R}_{33})/2$; green dash-dotted line: $(\tilde{R}_{12} + \tilde{R}_{13})/2$; blue dotted line: \tilde{R}_{23} .

plots that, although the profile of \tilde{R}_{11} is very similar to $\overline{u'u'}$ [term (I)], the contributions of the other two terms, especially $\overline{\rho'u'u'}/\bar{\rho}$ [term (II)], are not negligible. Term (II) is around 20–40 % of term (I) within the mixing region at late times after first shock and different times after reshock. $-a_1^2$ [term (III)] is around one order of magnitude smaller than term (I). This is different from the observations in [55,66], where terms (II) and (III) are at least 100 and 1000 times smaller, respectively, than term (I). Figure 13 shows the discrepancies between \tilde{R}_{11} and the two different approximations: (i) $\overline{u'u'}$ and (ii) $\overline{\rho'u'u'}/\bar{\rho} = \overline{u'u'} + \overline{\rho'u'u'}/\bar{\rho}$, through the ratios of \tilde{R}_{11} to the approximations. It can be seen that \tilde{R}_{11} cannot be well represented by $\overline{u'u'}$ alone, as the ratio can vary from 0.6 to 2.2. This is associated with the strong variable-density effects of the flow. If $\overline{\rho'u'u'}/\bar{\rho}$ is included to approximate \tilde{R}_{11} , there is a huge improvement in the approximation, as the ratio now only varies from 0.85 to 1. Although this suggests that a_1 has a small contribution to the decomposition of \tilde{R}_{11} , this does not mean that a_1 has an insignificant effect on the time evolution of \tilde{R}_{11} . Thus, it is shown in the next few sections that a_1 plays an important role in the transport equation of \tilde{R}_{11} through the component of the production term, $2a_1\bar{p}_{,1}$. A grid sensitivity analysis of the spatial profiles of different contributions to \tilde{R}_{11} is also

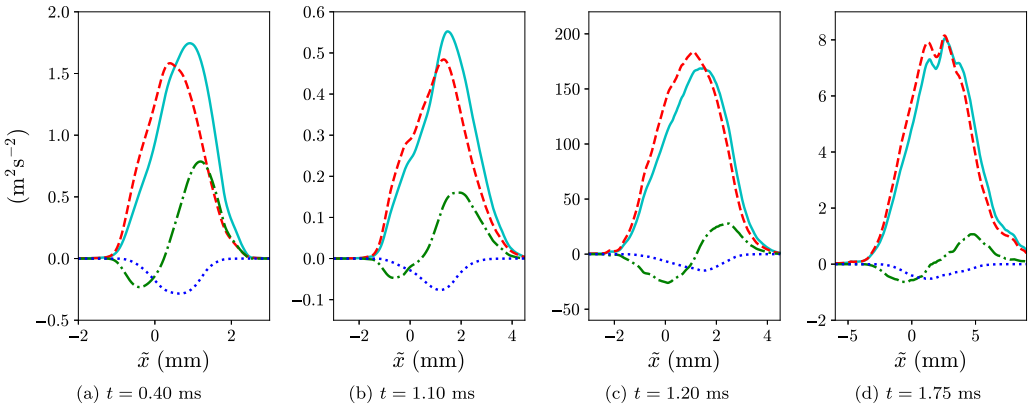


FIG. 12. Decomposition of the Reynolds normal stress component in the streamwise direction multiplied by the mean density, $\bar{\rho}\tilde{R}_{11}$, at different times. Cyan solid line: \tilde{R}_{11} ; red dashed line: $\overline{u'u'}$ [term (I)]; green dash-dotted line: $\overline{\rho'u'u'}/\bar{\rho}$ [term (II)]; blue dotted line: $-a_1^2$ [term (III)].

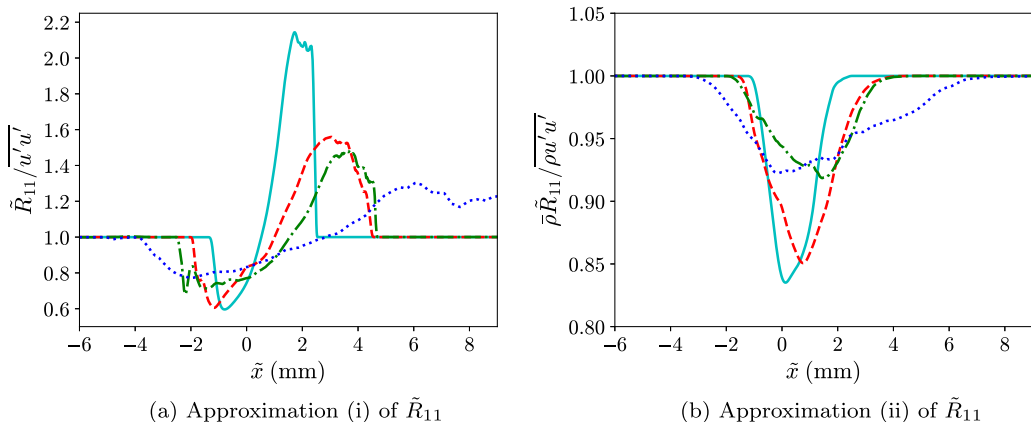


FIG. 13. Ratios of the Reynolds normal stress component in the streamwise direction multiplied by the mean density, $\bar{\rho}\tilde{R}_{11}$, to different approximations at different times. Cyan solid line: $t = 0.40$ ms; red dashed line: $t = 1.10$ ms; green dash-dotted line: $t = 1.20$ ms; blue dotted line: $t = 1.75$ ms.

provided in the Supplemental Material [52]. The profiles only show small grid sensitivities between the grid D and the grid E, and the discussion above is not much affected by the grid sensitivities.

Figure 14 shows the profiles of the turbulent kinetic energy at different times. Before reshock, the profiles look similar to those of $\bar{\rho}\tilde{R}_{11}$ as most of the turbulent kinetic energy is contributed by the Reynolds normal stress component in the streamwise direction. At reshock, the turbulent kinetic energy is amplified by three orders of magnitude. However, it decays rapidly due to large viscous dissipation over time.

VIII. BUDGETS OF THE SECOND MOMENTS BEFORE RESHOCK

In this section, the budgets of second moments— $\bar{\rho}a_1$, $\bar{\rho}b$, and $\bar{\rho}\tilde{R}_{11}$ —together with $\bar{\rho}k$ across the mixing layer before reshock are studied. All budgets are computed with the results from the highest resolution (grid E) simulation, for which the flow fields are well-resolved. A grid sensitivity analysis of the budgets is also given in the Supplemental Material [52]. The budgets are studied in the \tilde{x} coordinate system, equivalent to studying the budgets in the moving reference frame of the

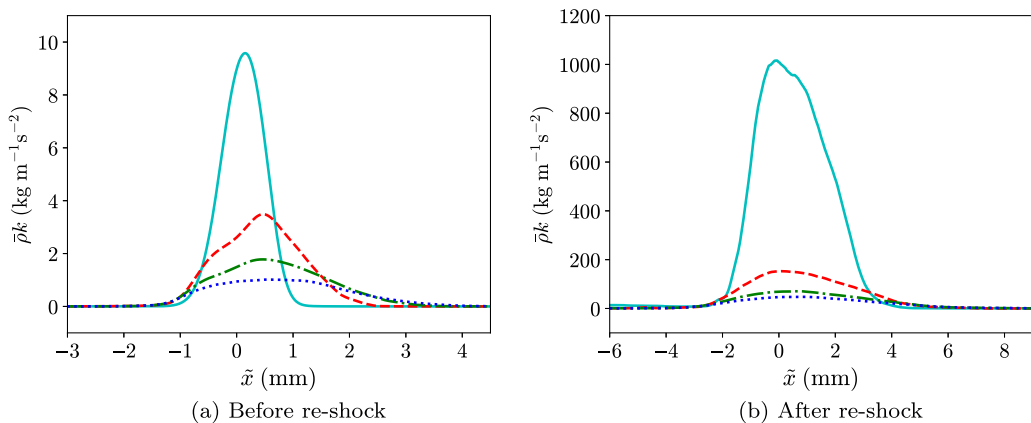


FIG. 14. Profiles of the turbulent kinetic energy, $\bar{\rho}k$, at different times. Cyan solid line in (a): $t = 0.05$ ms; red dashed line in (a): $t = 0.40$ ms; green dash-dotted line in (a): $t = 0.75$ ms; blue dotted line in (a): $t = 1.10$ ms. Cyan solid line in (b): $t = 1.20$ ms; red dashed line in (b): $t = 1.40$ ms; green dash-dotted line in (b): $t = 1.60$ ms; blue dotted line in (b): $t = 1.75$ ms.

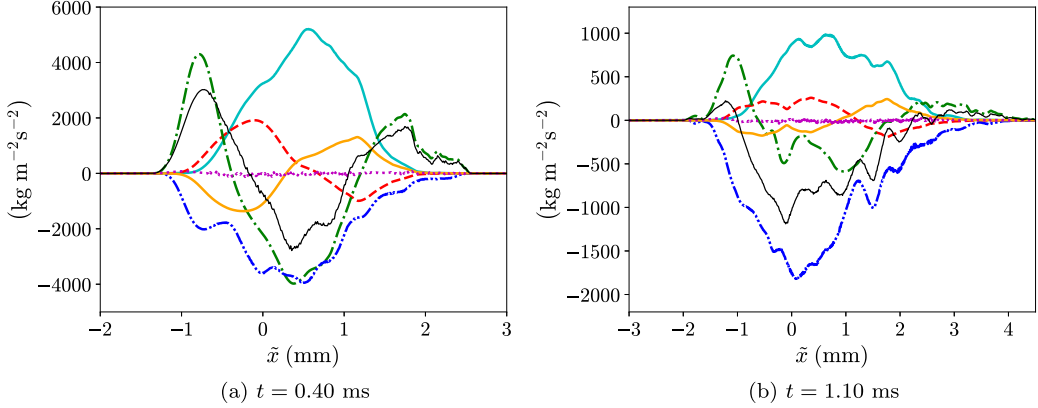


FIG. 15. Budgets of the turbulent mass flux component in the streamwise direction, $\bar{\rho}a_1$, given by Eq. (33), at different times before reshock. Cyan solid line: production [term (III)]; red dashed line: redistribution [term (IV)]; green dash-dotted line: turbulent transport [term (V)]; blue dash-dot-dotted line: destruction [term (VI)]; orange dash-triple-dotted line: negative of convection due to streamwise velocity associated with turbulent mass flux; magenta dotted line: residue; thin black solid line: summation of all terms (rate of change in the moving frame).

mixing layer. The convective terms in all of the transport equations of second moments for 1D mean flow have the common form of $[\bar{\rho}\tilde{u}(\cdot)]_{,1}$, where (\cdot) represents any of the second moments (a_1 , b , or R_{ij}). Using Eq. (18), the convective terms can be rewritten as

$$\frac{\partial \bar{\rho}\tilde{u}(\cdot)}{\partial x} = \underbrace{\frac{\partial \bar{\rho}\tilde{u}(\cdot)}{\partial x}}_{\text{term (I)}} + \underbrace{\frac{\partial \bar{\rho}a_1(\cdot)}{\partial x}}_{\text{term (II)}}, \quad (42)$$

where term (I) is the convection due to mean velocity, and term (II) is the convection due to velocity associated with turbulent mass flux. In the moving reference frame of the mixing layer, it is observed that \tilde{u} is quite uniformly close to zero compared to a_1 . Hence term (I) can be ignored. The convective term in this section is assumed to be fully represented by $[\bar{\rho}a_1(\cdot)]_{,1}$.

A. Turbulent mass flux

Figure 15 shows the spatial profiles of different terms on the right-hand side of the transport equation of the streamwise component of turbulent mass flux, $\bar{\rho}a_1$, given by Eq. (33) at different times before reshock across the mixing layer. The negative of the convective term of the same equation due to a_1 is also shown in the figure. The rate of change term on the left-hand side of the transport equation is computed by restarting the simulation at different checkpoints. In each plot, the magenta dotted line shows the profile of the residue, which is defined as the subtraction of the net right-hand-side term from the net left-hand-side term in the simulation frame. Therefore, the residue represents the numerical effect or the SGS effect on the rate of change of the conserved variable, i.e., $\bar{\rho}a_1$ here. From both Figs. 15(a) and 15(b), it can be seen that the residue is virtually zero across the mixing layer at different times before reshock. Note that the thin black solid line in each plot is the sum of all of the right-hand-side terms including the residue and the negative of the convection term due to a_1 , thus it represents the rate of change of $\bar{\rho}a_1$ in the moving frame of the mixing layer.

From Fig. 15, we can see that production [term (III)], destruction [term (VI)], and turbulent transport [term (V)] terms play important roles in the budget equation at the chosen times before reshock: $t = 0.40$ and 1.10 ms. At the two chosen times, the instability is in the nonlinear growth

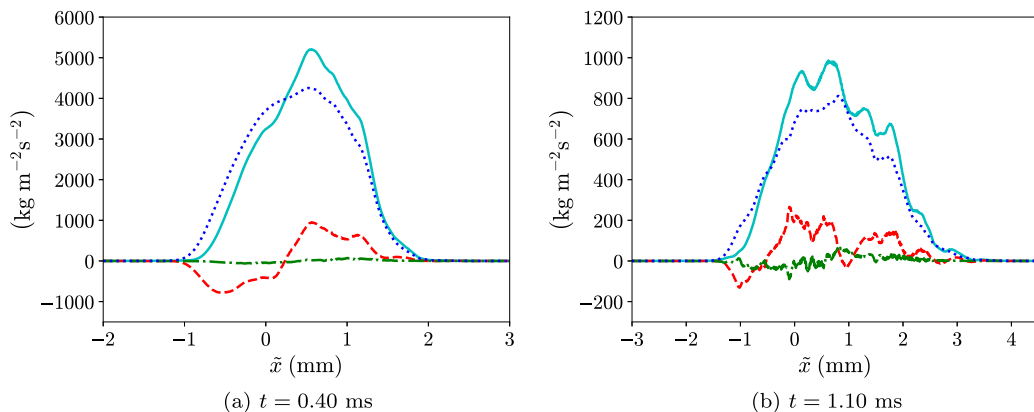


FIG. 16. Compositions of the production term [term (III)] in the transport equation for the turbulent mass flux component in the streamwise direction, $\bar{\rho}a_1$, at different times before reshock. Cyan solid line: overall production; red dashed line: $b\bar{p}_{,1}$; green dash-dotted line: $-b\bar{\tau}_{1,1}$; blue dotted line: $-\bar{R}_{11}\bar{\rho}_{,1}$.

regime. The production and destruction terms are not symmetric as they are skewed to the lighter fluid side with peaks also slightly positioned at that side. In the interior part of the mixing layer, the production, destruction, and turbulent transport terms are the dominant terms. The production term is strictly positive in the mixing region and peaks around the middle part of the mixing region. Nonetheless, both destruction and turbulent transport terms are negative in the interior part of the mixing layer to offset the effect from production. Overall, the combined effect of the destruction and turbulent transport terms is larger than that of the production, and hence the peak of turbulent mass flux reduces over time. At the edges of the mixing layer, all right-hand-side terms are small except the turbulent transport term, which is positive and responsible for the spreading of the turbulent mass flux. The magnitudes of redistribution [term (IV)] and convective terms are smaller than those of other terms but still have significant effects at different times before reshock. The two terms have similar magnitudes but opposite signs. The convective term decreases the turbulent mass flux on the heavier fluid side and increases that on the lighter fluid side. The redistribution term has the opposite effect of bringing the turbulent mass flux from the light fluid side back to the heavy fluid side. Opposite sign but close magnitude for the two corresponding transport terms in the budgets of $\bar{\rho}a_1$ is also noticed in the RTI turbulence by Livescu *et al.* [53].

The composition of the production term [term (III)] is shown in Fig. 16. It can be seen that at the chosen times before reshock, the production term is mainly contributed from the component, $-\bar{R}_{11}\bar{\rho}_{,1}$, which is observed to be strictly positive. Another constituent, $b\bar{p}_{,1}$, has a smaller contribution to the overall term, and $-b\bar{\tau}_{1,1}$ is negligible. $b\bar{p}_{,1}$ transfers the turbulent mass flux from the heavier fluid side to the lighter fluid side, although this effect is hidden in the overall production term. As for the destruction term [term (VI)], Fig. 17 shows that all three constituents [$\bar{\rho}(1/\bar{\rho})'p'_{,1}$, $-\bar{\rho}(1/\bar{\rho})'\tau'_{1,i}$, and $\bar{\rho}\varepsilon_{a_1}$] have similar magnitudes and are generally negative at the two times before reshock.

B. Density-specific-volume covariance

Figure 18 shows the spatial profiles of different budget terms that appear in the transport equation of $\bar{\rho}b$ given by Eq. (37) before reshock. Similar to the plots for budgets of the turbulent mass flux, the magenta dotted line represents the residue, which is the difference between the net left-hand-side and net right-hand-side terms. As seen in Figs. 18(a) and 18(b), the residue is basically zero. This means that there is a negligible numerical effect due to insufficient spatial grid spacing on the time evolution of $\bar{\rho}b$ before reshock. Before reshock, the production [term (III)], turbulent

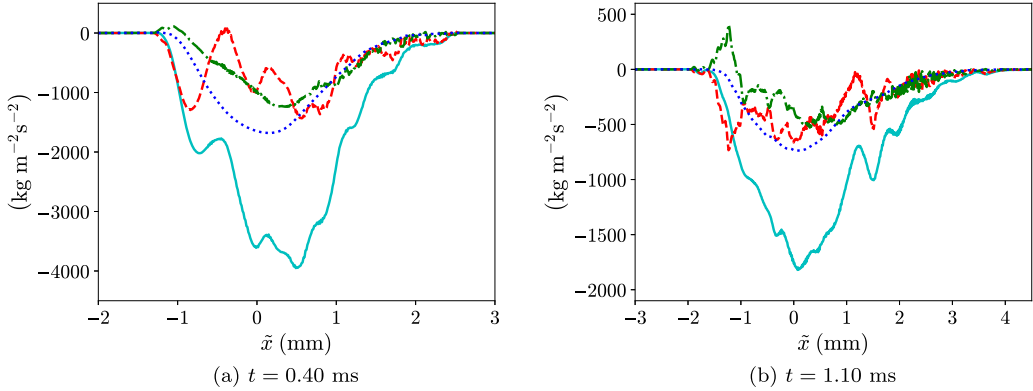


FIG. 17. Compositions of the destruction term [term (VI)] in the transport equation for the turbulent mass flux component in the streamwise direction, $\bar{\rho}a_1$, at different times before reshock. Cyan solid line: overall destruction; red dashed line: $\bar{\rho}(1/\rho)p'_{i1}$; green dash-dotted line: $-\bar{\rho}(1/\rho)\tau'_{ii}$; blue dotted line: $\bar{\rho}\varepsilon_{a_1}$.

transport [term (V)], and destruction [term (VI)] terms are dominant, but the redistribution [term (IV)] and convective terms cannot be neglected in the transport equation of $\bar{\rho}b$ either. Similar to the budgets of $\bar{\rho}a_1$, both production and destruction terms are asymmetric and skewed to the light fluid side. Although there is a positive effect in the interior part of the mixing layer from the production term to increase $\bar{\rho}b$, the effect is offset by both turbulent transport and destruction terms. The net rate of change of $\bar{\rho}b$ around the peak of b is small, so the peak of b (similarly for $\bar{\rho}b$) remains relatively constant in time compared to peaks of other second moments, which is shown earlier. At the edges of the mixing layer, most terms are small except the turbulent transport term, which is positive, which leads $\bar{\rho}b$ and b to spread. Both the redistribution term and the convection term due to a_1 redistribute $\bar{\rho}b$ across the layer, but they have exactly opposite effects (the redistribution term brings $\bar{\rho}$ from the lighter fluid side to the heavy fluid side and vice versa the convective term). They

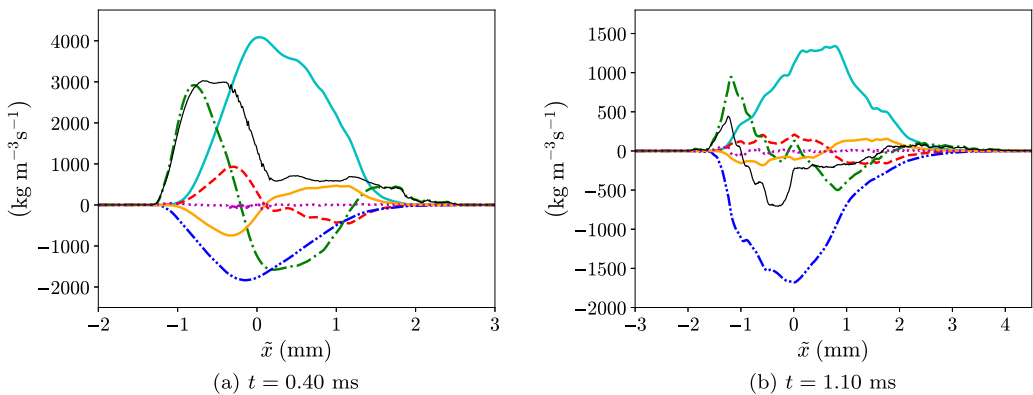


FIG. 18. Budgets of the density-specific-volume covariance multiplied by the mean density, $\bar{\rho}b$, given by Eq. (37), at different times before reshock. Cyan solid line: production [term (III)]; red dashed line: redistribution [term (IV)]; green dash-dotted line: turbulent transport [term (V)]; blue dash-dot-dotted line: destruction [term (VI)]; orange dash-triple-dotted line: negative of convection due to streamwise velocity associated with turbulent mass flux; magenta dotted line: residue; thin black solid line: summation of all terms (rate of change in the moving frame).

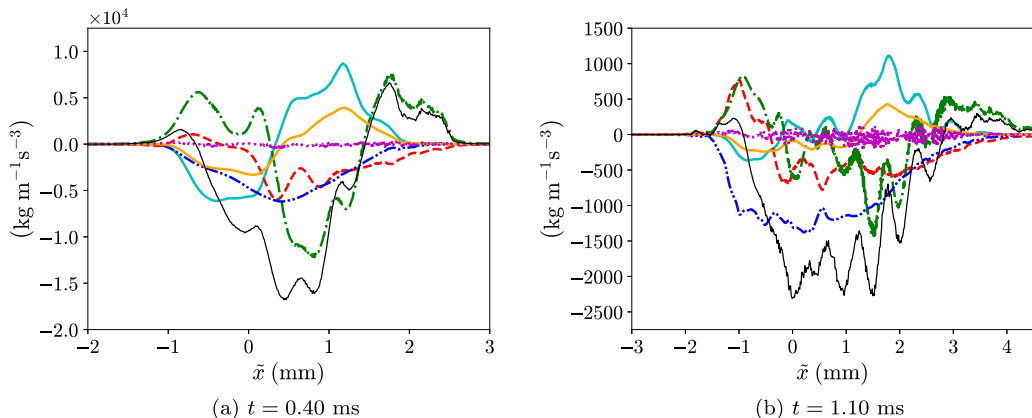


FIG. 19. Budgets of the Reynolds normal stress component in the streamwise direction multiplied by the mean density, $\bar{\rho}\tilde{R}_{11}$, given by Eq. (28), at different times before reshock. Cyan solid line: production [term (III)]; red dashed line: press-strain redistribution [term (V)]; green dash-dotted line: turbulent transport [term (IV)]; blue dash-dot-dotted line: dissipation [term (VI)]; orange dash-triple-dotted line: negative of convection due to streamwise velocity associated with turbulent mass flux; magenta dotted line: residue; thin black solid line: summation of all terms (rate of change in the moving frame).

also have similar shapes and thus roughly cancel effects from each other. A similar cancellation is also shown earlier for the corresponding terms in the budgets of $\bar{\rho}a_1$.

C. Favre-averaged Reynolds stress and turbulent kinetic energy

In Fig. 19, the spatial profiles of different terms in the transport equation of $\bar{\rho}\tilde{R}_{11}$ given by Eq. (28) at different times before reshock are compared. Similar to the budgets of other second moments, the residue due to spatial discretization is negligible before reshock. The critical terms in the interior mixing region that cause the peak of $\bar{\rho}\tilde{R}_{11}$ (slightly inclined towards the lighter fluid side) to decrease before reshock are the pressure-strain redistribution [term (V)], turbulent transport [term (IV)], and dissipation [term (VI)] terms. The production [term (III)] and convection terms are quite positive there, but their combined effect is smaller than that from the negative terms. In general, both production and convection terms are positive on the lighter fluid side and negative on the heavier fluid side. These two terms transport $\bar{\rho}\tilde{R}_{11}$ from the heavier fluid side to the lighter fluid side. On the other hand, the turbulent transport term helps bring $\bar{\rho}\tilde{R}_{11}$ from the lighter fluid side to the heavier fluid side, and more importantly it is also responsible for the spreading of the statistical quantity at the edges of the mixing layer.

Figure 20 shows the composition of production term [term (III)] before reshock. It can be seen that both $2a_1\bar{p}_{,1}$ and $-2\bar{\rho}\tilde{R}_{11}\tilde{u}_{,1}$ have large contributions to the production term, while the remaining component, $-2a_1\bar{\tau}_{11,1}$, is negligible. The composition of the turbulent transport term [term (IV)] is shown in Fig. 21. All three constituents, $-(\overline{\rho u'' u''})_{,1}$, $-2(\overline{u' p'})_{,1}$, and $2(\overline{u' \tau'_{11}})_{,1}$, have significant contributions to the term before reshock. The triple correlation component, $-(\overline{\rho u'' u'' u''})_{,1}$, is the root of the spreading effect, while $-2(\overline{u' p'})_{,1}$ and $2(\overline{u' \tau'_{11}})_{,1}$ have opposite effects for the transfer of $\bar{\rho}\tilde{R}_{11}$ between heavy and light fluid regions. $-2(\overline{u' p'})_{,1}$ transports $\bar{\rho}\tilde{R}_{11}$ from the heavier fluid side to the lighter fluid side and vice versa for $2(\overline{u' \tau'_{11}})_{,1}$.

Finally, the budget terms in the transport equation for the turbulent kinetic energy, $\bar{\rho}k$, given by Eq. (30) are compared at different times before reshock in Fig. 22. The residue due to numerical discretization is negligible at $t = 0.40$ ms. At later times, it becomes slightly larger relative to other budget terms, although it is still small in the budgets. At late times, the major terms in the interior part of the mixing layer are the pressure-dilatation [term (V)] and dissipation [term (VI)] terms.

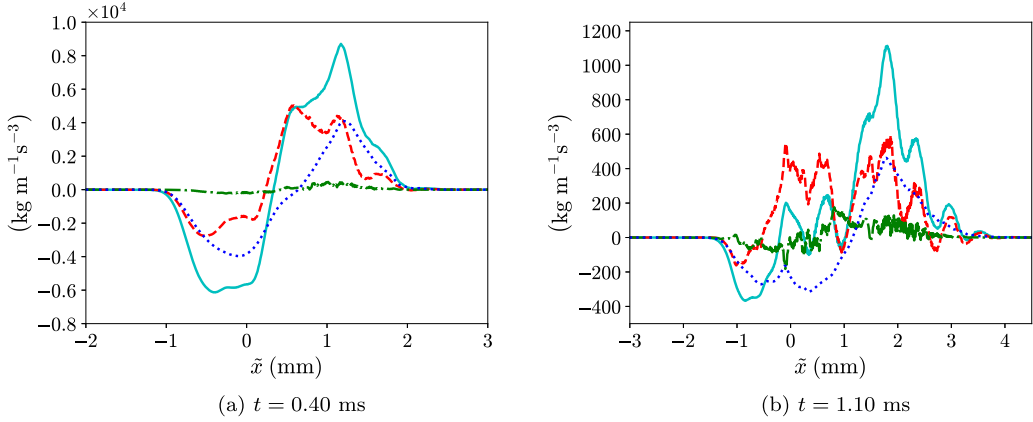


FIG. 20. Compositions of the production term [term (III)] in the transport equation for the Reynolds normal stress component in the streamwise direction multiplied by the mean density, $\bar{\rho}\tilde{R}_{11}$, at different times before reshock. Cyan solid line: overall production; red dashed line: $2a_1\bar{p}_{,1}$; green dash-dotted line: $-2a_1\bar{\tau}_{1,1}$; blue dotted line: $-2\bar{\rho}\tilde{R}_{11}\tilde{u}_{,1}$.

In single-species incompressible flows, the pressure-dilatation term is absent, but this term plays a large role to reduce the effects of dissipation term in this variable-density decaying flow before reshock. At the edges of the mixing layer, the turbulent transport term [term (IV)] is relatively more important and is responsible for the spread of the turbulent kinetic energy.

IX. FILTERED NAVIER-STOKES EQUATIONS AND TRANSPORT EQUATIONS OF THE LARGE-SCALE SECOND MOMENTS

In the present flow, the mixing transition follows after the mixing layer is traversed by the reflected shock. This reshock deposits baroclinic vorticity at both large and small scales, and rapid breakdown to fully developed turbulence ensues. The eddies span a wide range of length scales, where the largest and smallest eddies are estimated to be at scales of $O(1000)$ and $O(1)$ μm ,

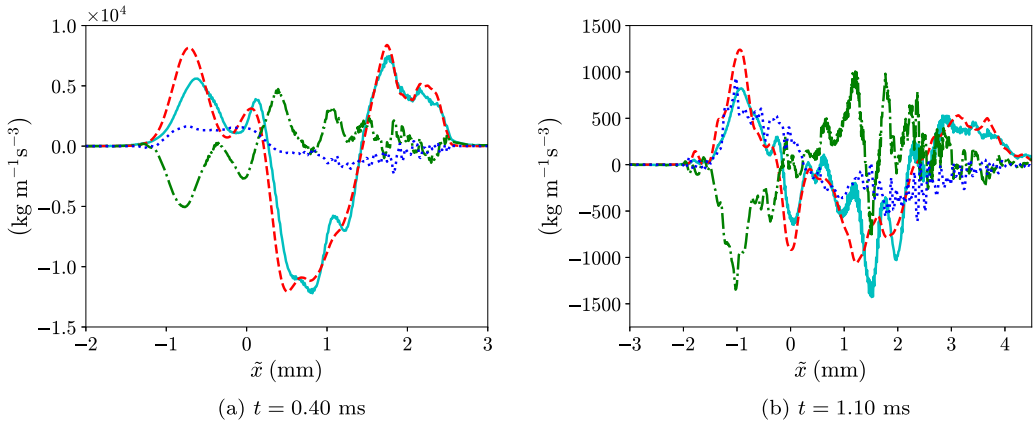


FIG. 21. Compositions of the turbulent transport term [term (IV)] in the transport equation for the Reynolds normal stress component in the streamwise direction multiplied by the mean density, $\bar{\rho}\tilde{R}_{11}$, at different times before reshock. Cyan solid line: overall turbulent transport; red dashed line: $-\overline{(\rho u'' u'' u'')}_{,1}$; green dash-dotted line: $-2\overline{(u' p')}_{,1}$; blue dotted line: $2\overline{(u' \tau'_{11})}_{,1}$.

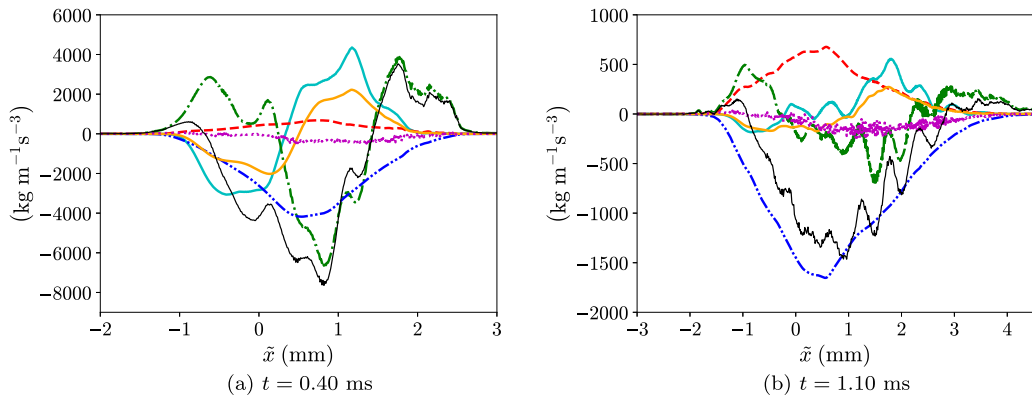


FIG. 22. Budgets of the turbulent kinetic energy, $\bar{\rho}k$, given by Eq. (30), at different times before reshock. Cyan solid line: production [term (III)]; red dashed line: pressure-dilatation [term (V)]; green dash-dotted line: turbulent transport [term (IV)]; blue dash-dot-dotted line: dissipation [term (VI)]; orange dash-triple-dotted line: negative of convection due to streamwise velocity associated with turbulent mass flux; magenta dotted line: residue; thin black solid line: summation of all terms (rate of change in the moving frame).

respectively [38]. The small scales of the turbulent flow after reshock are not well-resolved even in the highest resolution simulation. Therefore, it is more appropriate to study the transport equations of large-scale second moments derived from the filtered Navier-Stokes equations at times after reshock. The idea is that numerical regularization is assumed to have negligible effects on large-scale second moments that only contain scales from zero wave number to a cutoff wave number imposed by a filter that is considerably larger than the grid cutoff wave number. The analysis of the transport equations of the large-scale second moments is useful for (i) studying the mechanisms of the generation, destruction, and spreading of the large-scale turbulent features in shock-induced variable-density turbulence, (ii) examining the self-similarity of the turbulent flow, and (iii) understanding how the subfilter-scale stress can affect the resolved large-scale turbulent features in LES.

While the effects of filtering on the buoyancy-driven variable-density turbulence have been studied in [69], the focus in the current work is different. The analysis proposed here mainly focuses on the effects of SFS stress on large-scale statistical quantities resolved on a lower resolution grid, and the aim is to gain insight into the suitability of using LES data for analyzing RANS-based models. Spherical surface-averaged transport equations of different statistical quantities were also derived with the SGS stress in [65]. Here, we present the planar surface-averaged transport equations of the second moments, including the Favre-averaged Reynolds stress and turbulent kinetic energy, with the effects of SFS stress included.

The filtering operation of a variable, $f = f(x_i, t)$, with filter width, ℓ , can be defined as

$$\langle f(x_i, t) \rangle_\ell = \int_{-\infty}^{\infty} f(x'_i, t) G(x'_i, x_i) dx'_i, \quad (43)$$

where $\langle f \rangle_\ell$ is the filtered value and $G(x'_i, x_i)$ denotes a filter function. In variable-density flows, it is also convenient to define the Favre-filtered value, $\langle f \rangle_L$, as

$$\langle f \rangle_L = \frac{\langle \rho f \rangle_\ell}{\langle \rho \rangle_\ell}. \quad (44)$$

If we apply the filter on the mixture continuity equation and transport equation of momentum given by Eqs. (4) and (2), respectively, we can obtain the filtered Navier-Stokes equations:

$$\frac{\partial \langle \rho \rangle_\ell}{\partial t} + \frac{\partial (\langle \rho \rangle_\ell \langle u_k \rangle_L)}{\partial x_k} = 0, \quad (45)$$

$$\frac{\partial (\langle \rho \rangle_\ell \langle u_i \rangle_L)}{\partial t} + \frac{\partial (\langle \rho \rangle_\ell \langle u_k \rangle_L \langle u_i \rangle_L)}{\partial x_k} = -\frac{\partial (\langle \rho \rangle_\ell \delta_{ki})}{\partial x_k} + \frac{\partial \langle \tau_{ki} \rangle_\ell}{\partial x_k} - \frac{\partial \tau_{ki}^{\text{SFS}}}{\partial x_k}, \quad (46)$$

where commutation terms are assumed to be negligible. τ_{ij}^{SFS} is the SFS stress tensor given by

$$\tau_{ij}^{\text{SFS}} = \langle \rho u_i u_j \rangle_\ell - \langle \rho \rangle_\ell \langle u_i \rangle_L \langle u_j \rangle_L. \quad (47)$$

If averaging is further applied on the filtered continuity equation and transport equation of momentum given by Eqs. (45) and (46), respectively, the following Favre-averaged filtered Navier-Stokes equations are obtained:

$$\frac{\partial \overline{\langle \rho \rangle_\ell}}{\partial t} + \frac{\partial (\overline{\langle \rho \rangle_\ell} \overline{\langle u_k \rangle_L})}{\partial x_k} = 0, \quad (48)$$

$$\frac{\partial (\overline{\langle \rho \rangle_\ell} \overline{\langle u_i \rangle_L})}{\partial t} + \frac{\partial (\overline{\langle \rho \rangle_\ell} \overline{\langle u_k \rangle_L} \overline{\langle u_i \rangle_L})}{\partial x_k} = -\frac{\partial (\overline{\langle \rho \rangle_\ell} \delta_{ki})}{\partial x_k} + \frac{\partial \overline{\langle \tau_{ki} \rangle_\ell}}{\partial x_k} - \frac{\partial \overline{\tau_{ki}^{\text{SFS}}}}{\partial x_k} - \frac{\partial (\overline{\langle \rho \rangle_\ell} \tilde{R}_{L,ki})}{\partial x_k}, \quad (49)$$

where Reynolds and Favre decompositions on the filtered variables ($\langle f \rangle_\ell$ or $\langle f \rangle_L$) are involved:

$$\langle f \rangle_{\ell/L} = \overline{\langle f \rangle_{\ell/L}} + \langle f \rangle'_{\ell/L} = \overline{\langle f \rangle_{\ell/L}} + \langle f \rangle''_{\ell/L}, \quad (50)$$

and $\tilde{R}_{L,ij}$ is the large-scale Favre-averaged Reynolds stress tensor computed with the filtered density and velocity fields and is given by

$$\tilde{R}_{L,ij} = \frac{\overline{\langle \rho \rangle_\ell \langle u_i \rangle_L \langle u_j \rangle_L}}{\overline{\langle \rho \rangle_\ell}}. \quad (51)$$

In a 1D mean flow, the transport equation of $\overline{\langle \rho \rangle_\ell} \tilde{R}_{L,11}$ is given by

$$\begin{aligned} & \underbrace{\frac{\partial (\overline{\langle \rho \rangle_\ell} \tilde{R}_{L,11})}{\partial t}}_{\text{term (I)}} + \underbrace{\frac{\partial (\overline{\langle \rho \rangle_\ell} \overline{\langle u \rangle_L} \tilde{R}_{L,11})}{\partial x}}_{\text{term (II)}} \\ &= \underbrace{2a_{L,1} \left(\frac{\partial \overline{\langle \rho \rangle_\ell}}{\partial x} - \frac{\partial \overline{\langle \tau_{11} \rangle_\ell}}{\partial x} + \frac{\partial \overline{\tau_{11}^{\text{SFS}}}}{\partial x} \right)}_{\text{term (III)}} - 2\overline{\langle \rho \rangle_\ell} \tilde{R}_{L,11} \frac{\partial \overline{\langle u \rangle_L}}{\partial x} \\ & \quad - \underbrace{\frac{\partial (\overline{\langle \rho \rangle_\ell} \langle u \rangle_L \langle u \rangle_L \langle u \rangle_L)}{\partial x}}_{\text{term (IV)}} - 2 \underbrace{\frac{\partial (\overline{\langle u \rangle_L} \langle \rho \rangle'_\ell)}{\partial x}}_{\text{term (IV)}} + 2 \underbrace{\frac{\partial (\overline{\langle u \rangle_L} \langle \tau_{11} \rangle'_\ell)}{\partial x}}_{\text{term (IV)}} - 2 \underbrace{\frac{\partial (\overline{\langle u \rangle_L} \tau_{11}^{\text{SFS}'})}{\partial x}}_{\text{term (IV)}} + \underbrace{2\overline{\langle \rho \rangle'_\ell} \frac{\partial \langle u \rangle'_L}{\partial x}}_{\text{term (V)}} \\ & \quad - 2 \underbrace{\left(\langle \tau_{11} \rangle'_\ell \frac{\partial \langle u \rangle'_L}{\partial x} + \langle \tau_{12} \rangle'_\ell \frac{\partial \langle u \rangle'_L}{\partial y} + \langle \tau_{13} \rangle'_\ell \frac{\partial \langle u \rangle'_L}{\partial z} \right)}_{\text{term (VI)}} + 2 \underbrace{\left(\tau_{11}^{\text{SFS}' } \frac{\partial \langle u \rangle'_L}{\partial x} + \tau_{12}^{\text{SFS}' } \frac{\partial \langle u \rangle'_L}{\partial y} + \tau_{13}^{\text{SFS}' } \frac{\partial \langle u \rangle'_L}{\partial z} \right)}_{\text{term (VI)}}, \end{aligned} \quad (52)$$

where the left-hand side consists of the rate of change [term (I)] and convection [term (II)]. The right-hand side consists of production [term (III)], turbulent transport [term (IV)], pressure-strain redistribution [term (V)], and dissipation [term (VI)]. $a_{L,i} = \overline{\langle \rho \rangle'_\ell \langle u_i \rangle'_L} / \overline{\langle \rho \rangle_\ell}$ is the velocity associated with the large-scale turbulent mass flux $\overline{\langle \rho \rangle'_\ell \langle u_i \rangle'_L}$ computed on filtered fields.

The transport equation of $\langle \bar{\rho} \rangle_\ell \widetilde{R}_{L,22}$ for 1D mean flow can be reduced to

$$\begin{aligned}
 & \underbrace{\frac{\partial(\langle \bar{\rho} \rangle_\ell \widetilde{R}_{L,22})}{\partial t}}_{\text{term (I)}} + \underbrace{\frac{\partial(\langle \bar{\rho} \rangle_\ell \widetilde{u}'_L \widetilde{R}_{L,22})}{\partial x}}_{\text{term (II)}} \\
 &= \underbrace{-\frac{\partial(\langle \bar{\rho} \rangle_\ell \overline{v}'_L \overline{v}''_L \overline{u}''_L)}{\partial x}}_{\text{term (IV)}} + 2 \underbrace{\frac{\partial(\langle \bar{v}'_L \overline{\tau}_{21} \rangle_\ell)}{\partial x}}_{\text{term (IV)}} - 2 \underbrace{\frac{\partial(\langle \bar{v}'_L \tau_{21}^{\text{SFS}'} \rangle_\ell)}{\partial x}}_{\text{term (IV)}} + \underbrace{2 \langle \bar{p}' \rangle_\ell \frac{\partial \langle \bar{v}'_L \rangle_\ell}{\partial y}}_{\text{term (V)}} \\
 & \underbrace{-2 \left(\langle \tau_{21} \rangle'_\ell \frac{\partial \langle \bar{v}'_L \rangle_\ell}{\partial x} + \langle \tau_{22} \rangle'_\ell \frac{\partial \langle \bar{v}'_L \rangle_\ell}{\partial y} + \langle \tau_{23} \rangle'_\ell \frac{\partial \langle \bar{v}'_L \rangle_\ell}{\partial z} \right)}_{\text{term (VI)}} + 2 \left(\tau_{21}^{\text{SFS}'} \frac{\partial \langle \bar{v}'_L \rangle_\ell}{\partial x} + \tau_{22}^{\text{SFS}'} \frac{\partial \langle \bar{v}'_L \rangle_\ell}{\partial y} + \tau_{23}^{\text{SFS}'} \frac{\partial \langle \bar{v}'_L \rangle_\ell}{\partial z} \right).
 \end{aligned} \tag{53}$$

The transport equation of $\langle \bar{\rho} \rangle_\ell \widetilde{R}_{L,33}$ is similar.

The large-scale turbulent kinetic energy per unit mass is defined as $k_L = \widetilde{R}_{L,ii}/2$. The transport equation of $\langle \bar{\rho} \rangle_\ell k_L$ can be obtained by taking half of the trace of the transport equation of $\langle \bar{\rho} \rangle_\ell \widetilde{R}_{L,ij}$. In 1D mean flow, it has the following form:

$$\begin{aligned}
 & \underbrace{\frac{\partial(\langle \bar{\rho} \rangle_\ell k_L)}{\partial t}}_{\text{term (I)}} + \underbrace{\frac{\partial(\langle \bar{\rho} \rangle_\ell \widetilde{u}'_L k_L)}{\partial x}}_{\text{term (II)}} \\
 &= a_{L,1} \underbrace{\left(\frac{\partial \langle \bar{p} \rangle_\ell}{\partial x} - \frac{\partial \langle \bar{\tau}_{11} \rangle_\ell}{\partial x} + \frac{\partial \tau_{11}^{\text{SFS}}}{\partial x} \right)}_{\text{term (III)}} - \langle \bar{\rho} \rangle_\ell \widetilde{R}_{L,11} \frac{\partial \widetilde{u}'_L}{\partial x} \\
 & \underbrace{- \frac{1}{2} \frac{\partial(\langle \bar{\rho} \rangle_\ell \langle \bar{u}_i \rangle'_L \langle \bar{u}_i \rangle''_L \langle \bar{u}_i \rangle''_L)}{\partial x}}_{\text{term (IV)}} - \underbrace{\frac{\partial(\langle \bar{u}'_L \rangle_\ell \langle \bar{p}' \rangle_\ell)}{\partial x}}_{\text{term (IV)}} + \underbrace{\frac{\partial(\langle \bar{u}_i \rangle'_L \langle \bar{\tau}_{i1} \rangle'_\ell)}{\partial x}}_{\text{term (IV)}} - \underbrace{\frac{\partial(\langle \bar{u}_i \rangle'_L \tau_{i1}^{\text{SFS}'} \rangle_\ell)}{\partial x}}_{\text{term (IV)}} \\
 & \underbrace{+ \langle \bar{p}' \rangle_\ell \frac{\partial \langle \bar{u}_i \rangle'_L}{\partial x_i}}_{\text{term (V)}} - \underbrace{\langle \bar{\tau}_{ij} \rangle'_\ell \frac{\partial \langle \bar{u}_i \rangle'_L}{\partial x_j}}_{\text{term (VI)}} + \underbrace{\tau_{ij}^{\text{SFS}'} \frac{\partial \langle \bar{u}_i \rangle'_L}{\partial x_j}}_{\text{term (VI)}},
 \end{aligned} \tag{54}$$

where the left-hand side consists of the rate of change [term (I)] and convection [term (II)]. The right-hand side consists of production [term (III)], turbulent transport [term (IV)], pressure-dilatation [term (V)], and dissipation [term (VI)]. Note that term (III) represents the transfer of energy between $\langle \bar{\rho} \rangle_\ell k_L$ and the mean kinetic energy computed from filtered fields, $K_L = \langle \bar{\rho} \rangle_\ell \widetilde{u}'_L \langle \bar{u}_i \rangle'_L / 2$. Besides, the combination of $-\langle \bar{u}_i \rangle'_L \tau_{i1}^{\text{SFS}'} \rangle_\ell$ and $\tau_{ij}^{\text{SFS}'} \partial \langle \bar{u}_i \rangle'_L$ contributes to the transfer of energy between $\langle \bar{\rho} \rangle_\ell k_L$ and the mean SFS turbulent kinetic energy, $\tau_{ii}^{\text{SFS}}/2$.

In 1D mean flow, the transport equation of the large-scale turbulent mass flux component in the streamwise direction, $\langle \bar{\rho} \rangle_\ell a_{L,1}$, can be simplified to

$$\begin{aligned}
 & \underbrace{\frac{\partial(\langle \bar{\rho} \rangle_\ell a_{L,1})}{\partial t}}_{\text{term (I)}} + \underbrace{\frac{\partial(\langle \bar{\rho} \rangle_\ell \widetilde{u}'_L a_{L,1})}{\partial x}}_{\text{term (II)}} \\
 &= b_L \underbrace{\left(\frac{\partial \langle \bar{p} \rangle_\ell}{\partial x} - \frac{\partial \langle \bar{\tau}_{11} \rangle_\ell}{\partial x} + \frac{\partial \tau_{11}^{\text{SFS}}}{\partial x} \right)}_{\text{term (III)}} - \widetilde{R}_{L,11} \frac{\partial \langle \bar{\rho} \rangle_\ell}{\partial x}
 \end{aligned}$$

$$\begin{aligned}
 & \underbrace{+\overline{\langle \rho \rangle}_\ell \frac{\partial (a_{L,1} a_{L,1})}{\partial x}}_{\text{term (IV)}} - \overline{\langle \rho \rangle}_\ell a_{L,1} \frac{\partial \overline{\langle u \rangle}_L}{\partial x} - \underbrace{\overline{\langle \rho \rangle}_\ell \frac{\partial (\overline{\langle \rho \rangle}'_\ell \overline{\langle u \rangle}'_L \overline{\langle u \rangle}'_L / \overline{\langle \rho \rangle}_\ell)}}_{\text{term (V)}} \\
 & \underbrace{+\overline{\langle \rho \rangle}_\ell \left(\frac{1}{\overline{\langle \rho \rangle}_\ell} \right)' \left(\frac{\partial \langle \rho \rangle'_\ell}{\partial x} - \frac{\partial \langle \tau_{11} \rangle'_\ell}{\partial x} - \frac{\partial \langle \tau_{12} \rangle'_\ell}{\partial y} - \frac{\partial \langle \tau_{13} \rangle'_\ell}{\partial z} + \frac{\partial \tau_{11}^{\text{SFS}'}}{\partial x} + \frac{\partial \tau_{12}^{\text{SFS}'}}{\partial y} + \frac{\partial \tau_{13}^{\text{SFS}'}}{\partial z} \right)}_{\text{term (VI)}} + \overline{\langle \rho \rangle}_\ell \varepsilon_{a_{L,1}},
 \end{aligned} \tag{55}$$

where the left-hand side consists of the rate of change [term (I)] and convection [term (II)]. The right-hand side contains production [term (III)], redistribution [term (IV)], turbulent transport [term (V)], and destruction [term (VI)]. Also,

$$\varepsilon_{a_{L,i}} = -\overline{\langle u_i \rangle'_L} \frac{\partial \langle u_k \rangle'_L}{\partial x_k}. \tag{56}$$

b_L is the large-scale density-specific-volume covariance computed from the filtered fields and is given by $b_L = -\overline{\langle \rho \rangle}'_\ell (1/\overline{\langle \rho \rangle}_\ell)'$.

In 1D mean flow, the transport equation of $\overline{\langle \rho \rangle}_\ell b_L$ is given by

$$\begin{aligned}
 \underbrace{\frac{\partial (\overline{\langle \rho \rangle}_\ell b_L)}{\partial t}}_{\text{term (I)}} + \underbrace{\frac{\partial (\overline{\langle \rho \rangle}_\ell \widetilde{\langle u \rangle}_L b_L)}{\partial x}}_{\text{term (II)}} &= \underbrace{-2(b_L + 1)a_{L,1} \frac{\partial \overline{\langle \rho \rangle}_\ell}{\partial x}}_{\text{term (III)}} + \underbrace{+2\overline{\langle \rho \rangle}_\ell a_{L,1} \frac{\partial b_L}{\partial x}}_{\text{term (IV)}} \\
 &+ \underbrace{+\overline{\langle \rho \rangle}_\ell^2 \frac{\partial (\overline{\langle \rho \rangle}'_\ell (1/\overline{\langle \rho \rangle}_\ell)' \overline{\langle u \rangle}'_L / \overline{\langle \rho \rangle}_\ell)}{\partial x}}_{\text{term (V)}} + \underbrace{+2\overline{\langle \rho \rangle}_\ell^2 \varepsilon_{b_L}}_{\text{term (VI)}},
 \end{aligned} \tag{57}$$

where the left-hand side consists of the rate of change [term (I)] and convection [term (II)]. The right-hand side consists of production [term (III)], redistribution [term (IV)], turbulent transport [term (V)], and destruction [term (VI)]. Also,

$$\varepsilon_{b_L} = \left(\frac{1}{\overline{\langle \rho \rangle}_\ell} \right)' \frac{\partial \langle u_k \rangle'_L}{\partial x_k}. \tag{58}$$

A truncated Gaussian filter [70] is used. At each filtering operation, 1D filters in the x , y , and z directions are applied successively to the 3D fields. The filter in the x direction is given by

$$\begin{aligned}
 \langle f_{i,j,k} \rangle_{\ell,x} &= \frac{3565}{10\,368} f_{i,j,k} + \frac{3091}{12\,960} (f_{i-1,j,k} + f_{i+1,j,k}) + \frac{1997}{25\,920} (f_{i-2,j,k} + f_{i+2,j,k}) \\
 &+ \frac{149}{12\,960} (f_{i-3,j,k} + f_{i+3,j,k}) + \frac{107}{103\,680} (f_{i-4,j,k} + f_{i+4,j,k}),
 \end{aligned} \tag{59}$$

where the effective filter width of one filtering operation is $\ell = 4\Delta$, and Δ is the grid spacing of the finest grid level. Filtering in the y and z directions is in similar forms. The Gaussian filtering operation can be applied successively to achieve filtering with an essentially larger filter width. If the filter is applied N_f times repeatedly, the effective filter width is $\ell \approx 4\sqrt{N_f}\Delta$. The approximated filter widths obtained on the finest grid level of grid E with different numbers of filtering operations are shown in Table III. The truncated Gaussian filter is selected because of its positivity-preserving property for the density field.

TABLE III. Approximated filter widths obtained on the finest grid level of grid E with different numbers of filtering operations.

Number of filtering operations	Approximated filter width in Δ	Approximated filter width in physical unit (mm)
1	4Δ	0.049
4	8Δ	0.098
16	16Δ	0.195
64	32Δ	0.391
256	64Δ	0.781

X. EFFECTS OF THE FILTER WIDTH ON THE LARGE-SCALE SECOND MOMENTS AND THE SFS STRESS

The effects of filter width on the large-scale second moments including the Reynolds normal stress in the streamwise direction multiplied by the mean filtered density— $\overline{\langle \rho \rangle_\ell a_{L,1}}$, $\overline{\langle \rho \rangle_\ell b_L}$, and $\overline{\langle \rho \rangle_\ell \tilde{R}_{L,11}}$ —at $t = 1.40$ ms are shown in Figs. 23(a), 23(b), and 23(c), respectively. It can be seen that the magnitudes of the large-scale quantities reduce when the essential width of the filter applied to the density and momentum fields is increased because they are composed of scales from zero

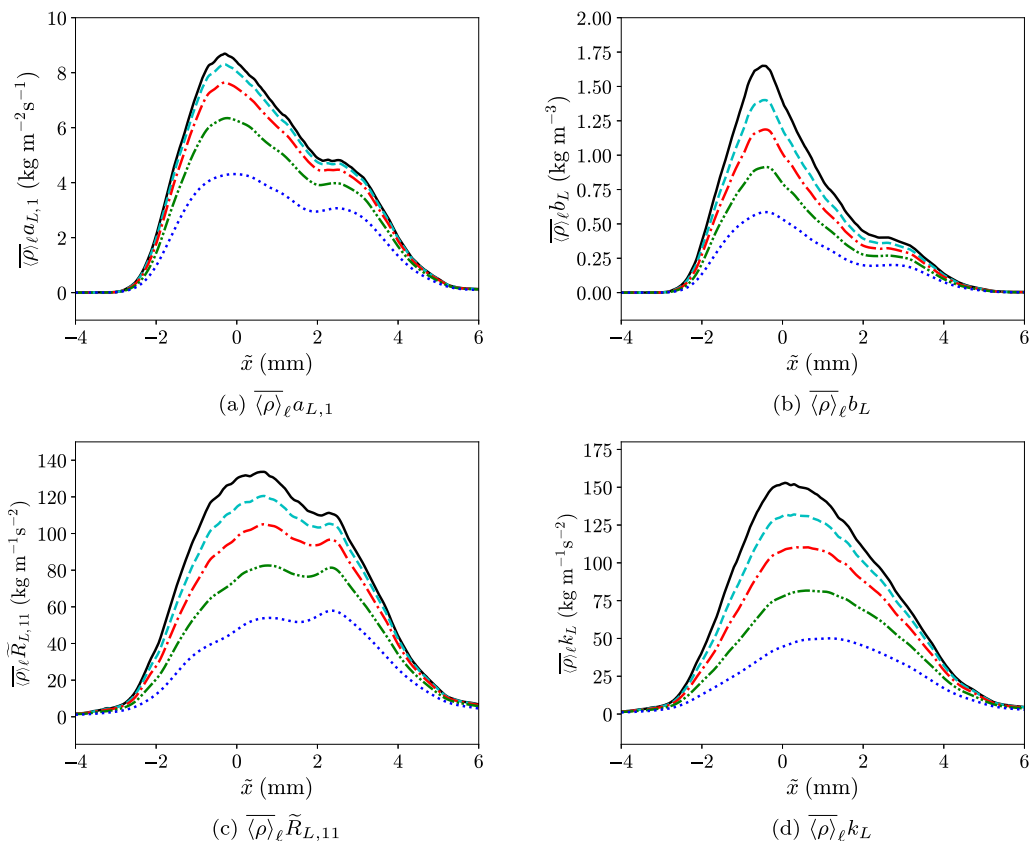


FIG. 23. Effect of filtering on the large-scale second moments and the turbulent kinetic energy, $\overline{\langle \rho \rangle_\ell k_L}$, at $t = 1.40$ ms after reshock. Black solid line: no filtering; cyan dashed line: $\ell \approx 8\Delta$; red dash-dotted line: $\ell \approx 16\Delta$; green dash-dot-dotted line: $\ell \approx 32\Delta$; blue dotted line: $\ell \approx 64\Delta$.

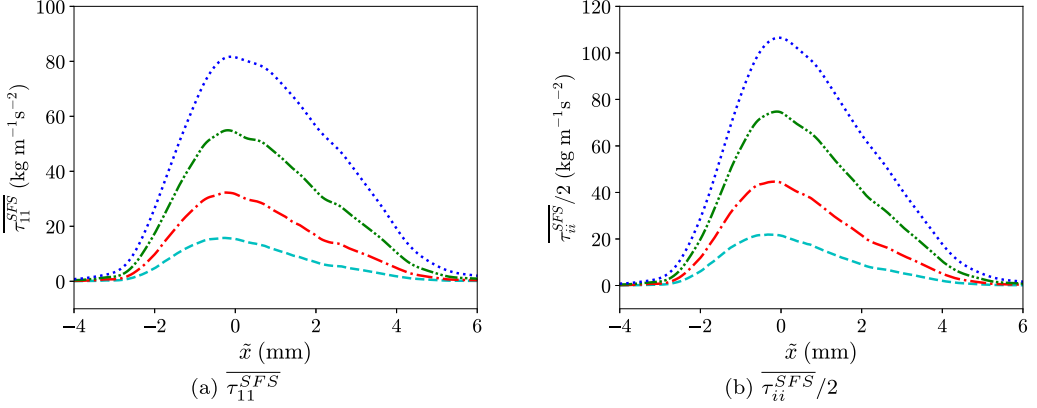


FIG. 24. Effect of filtering on the mean SFS stress component in the streamwise direction, $\overline{\tau_{11}^{SFS}}$, and the mean SFS turbulent kinetic energy, $\overline{\tau_{ii}^{SFS}}/2$, at $t = 1.40$ ms after reshock. Cyan dashed line: $\ell \approx 8\Delta$; red dash-dotted line: $\ell \approx 16\Delta$; green dash-dot-dotted line: $\ell \approx 32\Delta$; blue dotted line: $\ell \approx 64\Delta$.

wave number to a larger cutoff wave number. The shape of each quantity remains quite self-similar with different filter widths. Especially the location of the peak of each quantity does not move significantly under the effect of filtering. At large filter widths, all large-scale second moments including $\langle \rho \rangle_\ell \tilde{R}_{L,11}$ have similar degrees of changes in the magnitudes with the same filter width change.

Figure 24(a) shows the effect of filtering on the mean SFS normal stress component in the streamwise direction, $\overline{\tau_{11}^{SFS}}$. It can be seen that the magnitude of the SFS stress component increases with larger filter width. In fact, it is noticed that the sum of $\overline{\tau_{11}^{SFS}}$ and large-scale $\langle \rho \rangle_\ell \tilde{R}_{L,11}$ is virtually constant under the filtering effect. The same relation is also observed for the sum of the large-scale turbulent kinetic energy and the mean SFS turbulent kinetic energy, $\overline{\tau_{ii}^{SFS}}/2$. The magnitude of the large-scale turbulent kinetic energy decreases while that of the SFS turbulent kinetic energy rises when more filtering operations are applied, as seen in Figs. 23(d) and 24(b), respectively. These suggest that the correlations between the small scales and large scales are negligible compared to the large-scale–large-scale and small-scale–small-scale correlations. The effects of filter width on large-scale second-moments, SFS stress, and SFS turbulent kinetic energy at other times after reshock are shown in the Supplemental Material [52].

XI. BUDGETS OF THE LARGE-SCALE SECOND MOMENTS AFTER RESHOCK

In this section, the budgets of large-scale second moments computed with the filtered density and Favre-filtered velocity fields— $\langle \rho \rangle_\ell a_{L,1}$, $\langle \rho \rangle_\ell b_L$, and $\langle \rho \rangle_\ell \tilde{R}_{L,11}$ —together with $\langle \rho \rangle_\ell k_L$ across the mixing layer after reshock are examined. The chosen filter width is $\ell \approx 64\Delta = 0.781$ mm. A grid sensitivity analysis of the budgets at this filter width is provided in the Supplemental Material [52].

As with the unfiltered budgets before reshock, the budgets of large-scale second moments after reshock are studied in the \tilde{x} coordinate system, equivalent to studying the budgets in the moving reference frame of the mixing layer. The convective terms in all of the transport equations of large-scale second moments for 1D mean flow have the common form of $[\langle \rho \rangle_\ell \langle u \rangle_L(\cdot)]_1$, where (\cdot) represents any of the large-scale second moments ($a_{L,1}$, b_L , $\tilde{R}_{L,ij}$, or k_L). Using the relation $\langle u \rangle_L = \langle \tilde{u} \rangle_L + a_{L,1}$, the convective terms can be rewritten as

$$\frac{\partial \langle \rho \rangle_\ell \langle \tilde{u} \rangle_L(\cdot)}{\partial x} = \underbrace{\frac{\partial \langle \rho \rangle_\ell \langle \tilde{u} \rangle_L(\cdot)}{\partial x}}_{\text{term (I)}} + \underbrace{\frac{\partial \langle \rho \rangle_\ell a_{L,1}(\cdot)}{\partial x}}_{\text{term (II)}}, \quad (60)$$

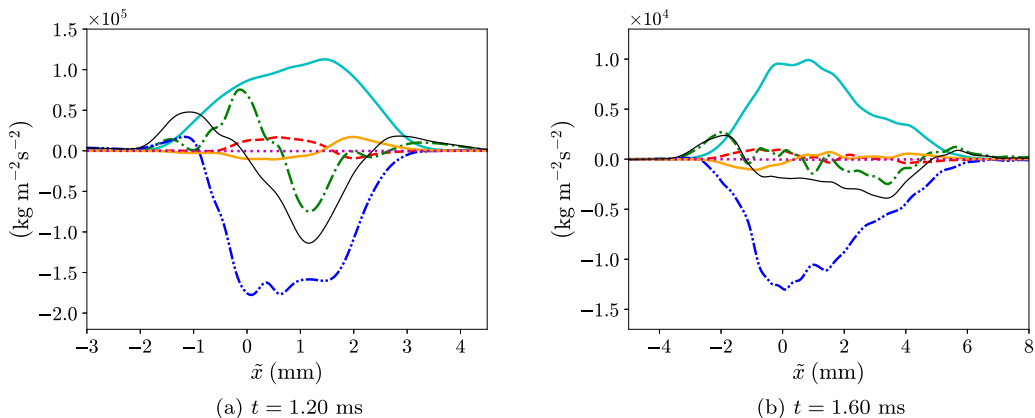


FIG. 25. Budgets of the large-scale turbulent mass flux component in the streamwise direction, $\overline{\langle \rho \rangle_\ell a_{L,1}}$, given by Eq. (55), at different times after reshock. Cyan solid line: production [term (III)]; red dashed line: redistribution [term (IV)]; green dash-dotted line: turbulent transport [term (V)]; blue dash-dot-dotted line: destruction [term (VI)]; orange dash-triple-dotted line: negative of convection due to streamwise velocity associated with turbulent mass flux; magenta dotted line: residue; thin black solid line: summation of all terms (rate of change in the moving frame).

where term (I) is the convection due to mean Favre-filtered velocity, and term (II) is the convection due to velocity associated with large-scale turbulent mass flux. Similar to the scenario without filtering, $\overline{\langle u \rangle_L}$ is observed to be uniformly close to zero in the moving reference frame of the mixing layer, and the term (I) can be neglected. Thus, the convective term is thought to be fully contributed by $[\overline{\langle \rho \rangle_\ell a_{L,1}}]_1$ in the analysis of this section. While only the budgets of the large-scale second moments at $t = 1.20$ and 1.60 ms are shown in this section, the budgets at two other times after reshock are included in the Supplemental Material [52].

A. Large-scale turbulent mass flux

Figure 25 shows the spatial profiles of different right-hand-side terms in the transport equation for the large-scale turbulent mass flux component in the streamwise direction, $\overline{\langle \rho \rangle_\ell a_{L,1}}$, given by Eq. (55), together with the negative of the convection term due to $a_{L,1}$ after reshock. Similar to the budgets before reshock, the magenta dotted line represents the residue which is defined as the subtraction of the net right-hand-side terms from the net left-hand-side term in the simulation frame. The residue here provides a way to verify that the numerical regularization or SGS effect has negligible effects on the budgets of large-scale second moments at the chosen filter width. The rate of change of $\overline{\langle \rho \rangle_\ell a_{L,1}}$ in the moving reference frame of the mixing layer is represented by the thin black line, which is the subtraction of the convective term due to $a_{L,1}$ from the summation of the net right-hand side and the residue.

Similar to the times before reshock, production [term (III)] and destruction [term (VI)] terms are asymmetric after reshock, as shown in Fig. 25. Both terms are skewed toward and have peaks at positions slightly toward the lighter fluid side. As seen from Fig. 25, the production and destruction terms are the dominant terms among all the right-hand-side terms in the interior mixing region after reshock. In this region, the magnitude of the destruction is larger than that of the production, and this drives the peak of the large-scale turbulent mass flux to diminish over time after reshock, as indicated by the negative rate of change at all times. At the edges of the mixing region, the turbulent transport term [term (V)] becomes relatively more important and causes the turbulent mass flux to spread over time. The redistribution [term (IV)] and convective terms are small across the mixing layer compared to the other right-hand-side terms. In fact, the redistribution term is

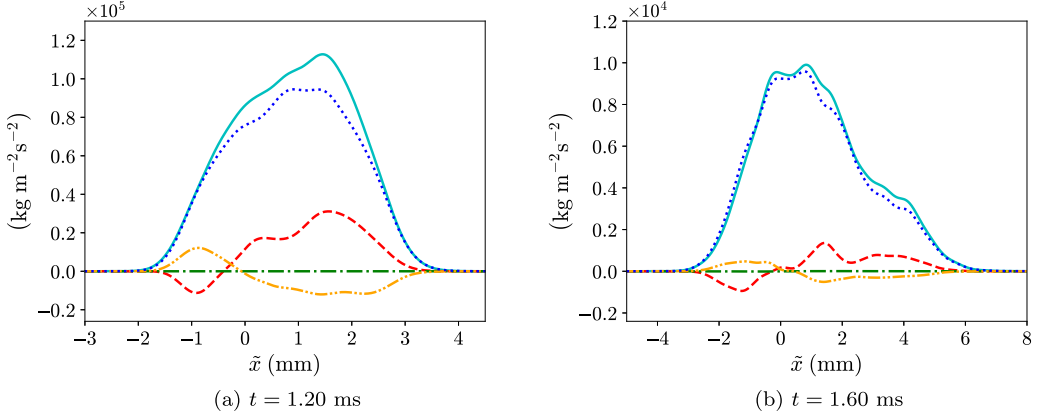


FIG. 26. Compositions of the production term [term (III)] in the transport equation for the large-scale turbulent mass flux component in the streamwise direction, $\overline{\langle \rho \rangle}_{\ell} a_{L,1}$, at different times after reshock. Cyan solid line: overall production; red dashed line: $b_L \overline{\langle p \rangle}_{\ell,1}$; green dash-dotted line: $-b_L \overline{\langle \tau_{11} \rangle}_{\ell,1}$; orange dash-dot-dotted line: $b_L \overline{\tau_{11}^{\text{SFS}}}_{,1}$; blue dotted line: $-\tilde{R}_{L,11} \overline{\langle \rho \rangle}_{\ell,1}$.

commonly ignored in many turbulent mixing models, such as the BHR k - S - a model by Banerjee *et al.* [19] and the k - L - a model by Morgan and Wickett [29]. The compositions of the production and destruction terms are shown in Figs. 26 and 27, respectively. As seen from both figures, the components with filtered molecular shear stress, $-b_L \overline{\langle \tau_{11} \rangle}_{\ell,1}$ and $-\overline{\langle \rho \rangle}_{\ell} \overline{(1/\langle \rho \rangle)'} (\partial \langle \tau_{1i} \rangle'_{\ell} / \partial x_i)$, are both zero at different times, and this indicates that the molecular shear stress has no direct effect on the large-scale turbulent mass flux through its budget.

Examining Fig. 26 for the composition of the production term [term (III)], it can be seen that the shapes and relative importance of the two components of the production term, $-\tilde{R}_{L,11} \overline{\langle \rho \rangle}_{\ell,1}$ and $b_L \overline{\langle p \rangle}_{\ell,1}$, after reshock are similar to those of the corresponding ones before reshock. However, there is an additional term with the SFS stress, $b_L \overline{\tau_{11}^{\text{SFS}}}_{,1}$, in the composition due to filtering. In general,

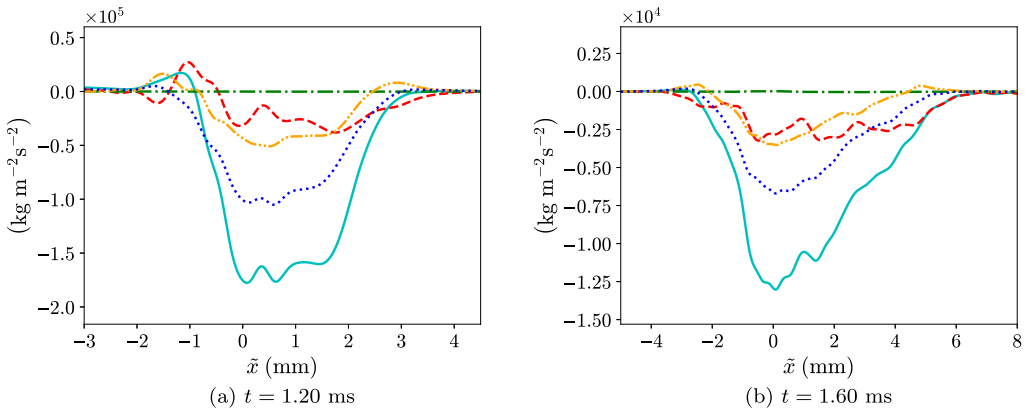


FIG. 27. Compositions of the destruction term [term (VI)] in the transport equation for the large-scale turbulent mass flux component in the streamwise direction, $\overline{\langle \rho \rangle}_{\ell} a_{L,1}$, at different times after reshock. Cyan solid line: overall destruction; red dashed line: $\overline{\langle \rho \rangle}_{\ell} \overline{(1/\langle \rho \rangle)'} \overline{\langle p \rangle}_{\ell,1}$; green dash-dotted line: $-\overline{\langle \rho \rangle}_{\ell} \overline{(1/\langle \rho \rangle)'} (\partial \langle \tau_{1i} \rangle'_{\ell} / \partial x_i)$; orange dash-dot-dotted line: $\overline{\langle \rho \rangle}_{\ell} \overline{(1/\langle \rho \rangle)'} (\partial \tau_{1i}^{\text{SFS}} / \partial x_i)$; blue dotted line: $-\overline{\langle \rho \rangle}_{\ell} \overline{(1/\langle \rho \rangle)'} (\partial \tau_{1i}^{\text{SFS}} / \partial x_i)$.

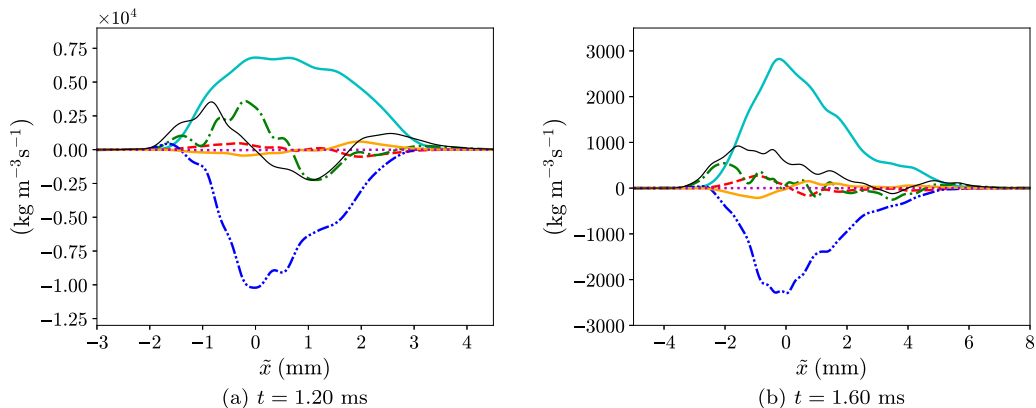


FIG. 28. Budgets of the large-scale density-specific-volume covariance multiplied by the mean filtered density, $\langle \bar{\rho} \rangle_\ell b_L$, given by Eq. (57), at different times after reshock. Cyan solid line: production [term (III)]; red dashed line: redistribution [term (IV)]; green dash-dotted line: turbulent transport [term (V)]; blue dash-dot-dotted line: destruction [term (VI)]; orange dash-triple-dotted line: negative of convection due to streamwise velocity associated with turbulent mass flux; magenta dotted line: residue; thin black solid line: summation of all terms (rate of change in the moving frame).

the component with the large-scale Reynolds stress, $-\tilde{R}_{L,11} \langle \bar{\rho} \rangle_{\ell,1}$, has the largest contribution to the production term and appears strictly positive. Another two constituents, $b_L \langle \bar{\rho} \rangle_{\ell,1}$ and $b_L \tau_{11}^{\text{SFS}}$, have smaller contributions and have conflicting effects. The latter largely reduces the influence of the former on the production term. Therefore, the production term can be regarded as mainly supplied by the component with the large-scale Reynolds stress. As for the destruction [term (VI)], it can be seen in Fig. 27 that the contribution of each constituent after reshock is similar to the corresponding one in the unfiltered budgets before reshock, except that the role of the component with molecular shear stress is replaced by a component with SFS stress, $\langle \bar{\rho} \rangle_\ell (1 / \langle \bar{\rho} \rangle_\ell)' (\partial \tau_{1i}^{\text{SFS}} / \partial x_i)$. Similar to the corresponding component with ε_{a_1} in the budgets before reshock, the component with $\varepsilon_{a_{L,1}}$ also contributes significantly to the destruction term after reshock.

B. Large-scale density-specific-volume covariance

Figure 28 shows the spatial profiles of different terms that appear in the transport equation for the large-scale density-specific-volume covariance multiplied by the mean filtered density, $\langle \bar{\rho} \rangle_\ell b_L$, given by Eq. (57) after reshock. As for the plots for budgets of the large-scale turbulent mass flux, the magenta dotted line represents the residue. As seen in the subfigures, the residue is virtually zero at different times after reshock, and this means that there is an insignificant effect of numerical regularization on the rate of change of $\langle \bar{\rho} \rangle_\ell b_L$.

As seen from the figure, the production [term (III)] and destruction [term (VI)] terms are the dominant terms in the interior region of the mixing layer. In the papers by Tomkins *et al.* [62] and Mohaghar *et al.* [66], it was also observed in the layer interior that the production term is dominant in the budgets of density-specific-volume covariance. In the interior part of the mixing layer, the rate of change of $\langle \bar{\rho} \rangle_\ell b_L$ is negative just after reshock as the magnitude of the negative destruction term is larger than that of the positive production term. Thus, the amplitude of the large-scale second moment decreases just after reshock. Nevertheless, soon after reshock, the relative magnitude of the production term in the middle part of the mixing layer becomes larger, and even larger than that of the destruction term at late times. As a result, the rate of change of $\langle \bar{\rho} \rangle_\ell b_L$ at the peak location turns slightly positive at later times. Overall, the budget terms are quite balanced in the interior part of the mixing layer at late times as the production term roughly cancels the destruction term. This is

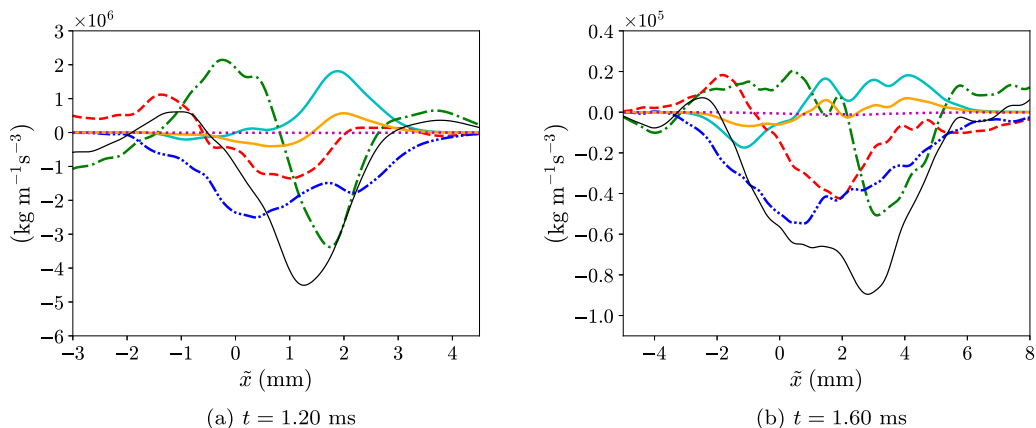


FIG. 29. Budgets of the large-scale Favre-averaged Reynolds normal stress component in the streamwise direction multiplied by the mean filtered density, $\langle \bar{\rho} \rangle_\ell \tilde{R}_{L,11}$, given by Eq. (52), at different times after reshock. Cyan solid line: production [term (III)]; red dashed line: press-strain redistribution [term (V)]; green dash-dotted line: turbulent transport [term (IV)]; blue dash-dot-dotted line: dissipation [term (VI)]; orange dash-triple-dotted line: negative of convection due to streamwise velocity associated with turbulent mass flux; magenta dotted line: residue; thin black solid line: summation of all terms (rate of change in the moving frame).

similar to the observations on the budgets of density-specific-volume covariance in the heavy-light case of the spherical RMI [65] and the planar RTI [53]. As a result, $\langle \bar{\rho} \rangle_\ell b_L$ and b_L have quite stationary peaks at late times. Although the turbulent transport term [term (V)] is not small in the central part of the mixing layer, its effect is small compared to the production and destruction terms. However, the turbulent transport term becomes relatively more important at the heavier fluid edge of the mixing region. The term is positive at both edges of the mixing layer and is the vital term at the heavier fluid side for the spreading of $\langle \bar{\rho} \rangle_\ell b_L$ over time.

C. Large-scale Favre-averaged Reynolds stress and large-scale turbulent kinetic energy

In Fig. 29, the spatial profiles of different budget terms of the large-scale Favre-averaged Reynolds stress component in the streamwise direction multiplied by the mean filtered density, $\langle \bar{\rho} \rangle_\ell \tilde{R}_{L,11}$, after reshock are shown. Each budget term in the transport equation for $\langle \bar{\rho} \rangle_\ell \tilde{R}_{L,11}$ is given by Eq. (52). As shown in the figure, the residue, represented by the magenta dotted line, is basically zero at all times. Thus, the effect of numerical regularization on $\langle \bar{\rho} \rangle_\ell \tilde{R}_{L,11}$ can be ignored.

From the figure, we can see that all terms except the convection term play significant roles in the rate of change of $\langle \bar{\rho} \rangle_\ell \tilde{R}_{L,11}$ in the interior part of the mixing region. Similar to the budgets before reshock, the production term [term (III)] is positive on the light fluid side and negative on the heavy fluid side to transport $\langle \bar{\rho} \rangle_\ell \tilde{R}_{L,11}$ from the heavier fluid side to the lighter fluid side. On the other hand, generally the turbulent transport term [term (IV)] has a larger magnitude but the opposite effect in the interior region of the mixing layer compared to the production term. In the same region, both pressure-strain redistribution [term (V)] and dissipation [term (VI)] terms are negative in general and hence the overall rate of change is negative. At the edges of the mixing layer, only the turbulent transport and pressure-strain redistribution are critical terms. Their combined effect contributes to the spreading of $\langle \bar{\rho} \rangle_\ell \tilde{R}_{L,11}$ on the lighter fluid side over time, while there is some antispreading effect on the heavier fluid side for quite a long period of time after reshock.

Figures 30 and 31 show the compositions of production [term (III)] and turbulent transport [term (IV)] terms, respectively, after reshock. Both figures show that the components due to filtered molecular shear stress, $-2a_{L,1} \langle \tau_{11} \rangle_{\ell,1}$ and $2 \langle \langle u \rangle'_L \langle \tau_{11} \rangle'_\ell \rangle_{,1}$, are insignificant to the budgets at different times after reshock. Considering the composition of the production term in Fig. 30, the component

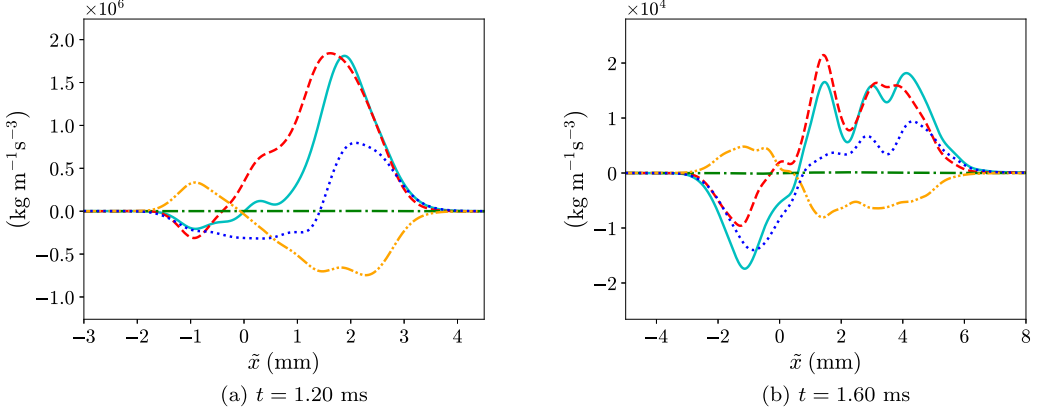


FIG. 30. Compositions of the production term [term (III)] in the transport equation for the large-scale Favre-averaged Reynolds normal stress component in the streamwise direction multiplied by the mean filtered density, $\overline{\langle \rho \rangle}_\ell \tilde{R}_{L,11}$, at different times after reshock. Cyan solid line: overall production; red dashed line: $2a_{L,1} \overline{\langle p \rangle}_{\ell,1}$; green dash-dotted line: $-2a_{L,1} \overline{\langle \tau_{11} \rangle}_{\ell,1}$; orange dash-dot-dotted line: $2a_{L,1} \overline{\tau_{11}^{\text{SFS}}}$; blue dotted line: $-2 \overline{\langle \rho \rangle}_\ell \tilde{R}_{L,11} \overline{\langle u \rangle}_{L,1}$.

with SFS stress, $2a_{L,1} \overline{\tau_{11}^{\text{SFS}}}$, appears as a new term compared to the budgets without filtering before reshock. Both constituents $2a_{L,1} \overline{\langle p \rangle}_{\ell,1}$ and $-2 \overline{\langle \rho \rangle}_\ell \tilde{R}_{L,11} \overline{\langle u \rangle}_{L,1}$ play similar roles to the production term. They are negative on the heavier fluid side and positive on the lighter fluid side. However, the former has a larger effect on the lighter side while the effect of the latter is stronger on the heavier fluid side. The component with SFS stress has a similar magnitude to $-2 \overline{\langle \rho \rangle}_\ell \tilde{R}_{L,11} \overline{\langle u \rangle}_{L,1}$ but the opposite effect that brings $\overline{\langle \rho \rangle}_\ell \tilde{R}_{L,11}$ from the lighter fluid side to the heavier fluid side. Inspecting the composition of the turbulent transport term, the three constituents, $-\overline{\langle \rho \rangle}_\ell \overline{\langle u \rangle}'_L \overline{\langle u \rangle}''_L \overline{\langle u \rangle}''_L$, $-2 \overline{\langle u \rangle}'_L \overline{\langle p \rangle}'_{\ell,1}$, and $-2 \overline{\langle u \rangle}'_L \tau_{11}^{\text{SFS}}$, have significant contributions to the term after reshock. The triple velocity correlation component, $-\overline{\langle \rho \rangle}_\ell \overline{\langle u \rangle}''_L \overline{\langle u \rangle}''_L \overline{\langle u \rangle}''_L$, and the component arising from

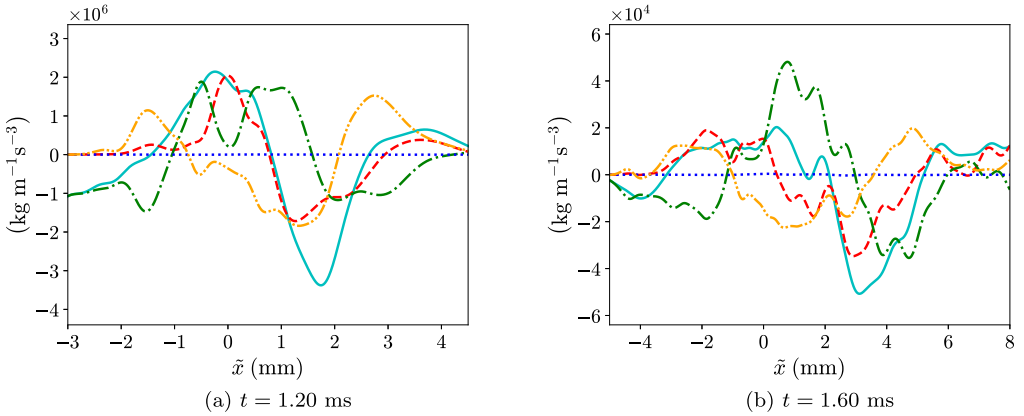


FIG. 31. Compositions of the turbulent transport term [term (IV)] in the transport equation for the large-scale Favre-averaged Reynolds normal stress component in the streamwise direction multiplied by the mean filtered density, $\overline{\langle \rho \rangle}_\ell \tilde{R}_{L,11}$, at different times after reshock. Cyan solid line: overall turbulent transport; red dashed line: $-\overline{\langle \rho \rangle}_\ell \overline{\langle u \rangle}'_L \overline{\langle u \rangle}''_L \overline{\langle u \rangle}''_L$; green dash-dotted line: $-2 \overline{\langle u \rangle}'_L \overline{\langle p \rangle}'_{\ell,1}$; blue dotted line: $2 \overline{\langle u \rangle}'_L \overline{\langle \tau_{11} \rangle}'_{\ell,1}$; orange dash-dot-dotted line: $-2 \overline{\langle u \rangle}'_L \tau_{11}^{\text{SFS}}$.

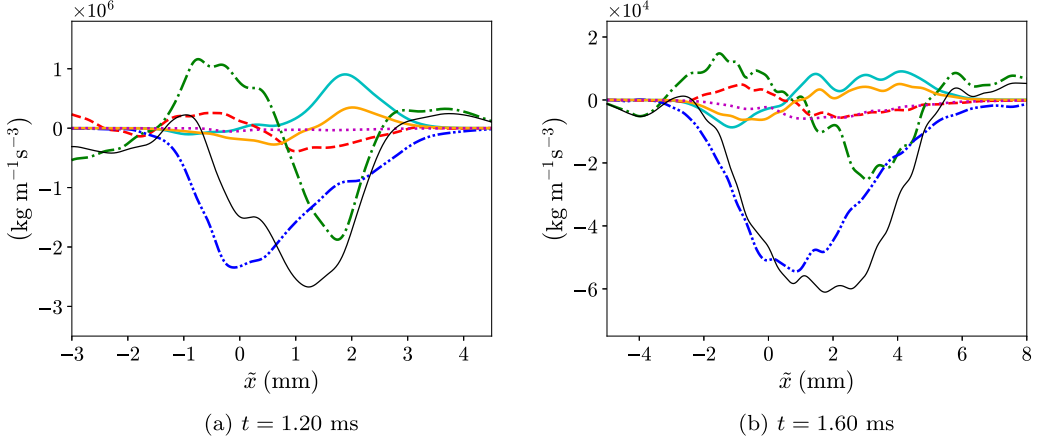


FIG. 32. Budgets of the large-scale turbulent kinetic energy, $\overline{(\rho)_\ell k_L}$, given by Eq. (54), at different times after reshock. Cyan solid line: production [term (III)]; red dashed line: pressure-dilatation [term (V)]; green dash-dotted line: turbulent transport [term (IV)]; blue dash-dot-dotted line: dissipation [term (VI)]; orange dash-triple-dotted line: negative of convection due to streamwise velocity associated with turbulent mass flux; magenta dotted line: residue; thin black solid line: summation of all terms (rate of change in the moving frame).

filtering, $-2\overline{(\langle u \rangle'_L \tau_{11}^{\text{SFS}'})}_{,1}$, are responsible for the spreading of $\overline{(\rho)_\ell \tilde{R}_{L,11}}$. On the other hand, the constituent $-2\overline{(\langle u \rangle'_L \langle \rho \rangle'_\ell)}_{,1}$ has an antispreading effect.

Figure 32 shows a comparison of different budget terms in the transport equation for the large-scale turbulent kinetic energy, $\overline{(\rho)_\ell k_L}$, given by Eq. (54). The residue of $\overline{(\rho)_\ell k_L}$ is negligible at early times after reshock but becomes slightly larger at later times. At $t = 1.60$ ms, the residue cannot be considered as zero but is still small compared with other budget terms. Through grid sensitivity analysis presented in the Supplemental Material [52], it is found that the residue computed with the grid E is largely reduced compared to that with the grid D.

It should be noted again that in incompressible single-species flow, the pressure-dilatation term [term (V)] is zero. As seen from the figure, the pressure-dilatation term in the variable-density flow being studied here is not zero. However, its influence is generally very small across the mixing layer, and its effect is roughly canceled by the convection term. The effect from pressure-dilatation is commonly ignored in many RANS-based models [19,29] for RMI-induced turbulence. In the interior part of the mixing region, the dissipation dominates the overall rate of change of the large-scale turbulent kinetic energy, and the quantity decays over time. Note that the dissipation term is contributed mainly by the component with SFS stress, $\overline{\tau_{ij}^{\text{SFS}'}}(\partial \langle u_i \rangle'_L / \partial x_j)$. In the interior region of RTI [53], the production and dissipation terms are equally important in the turbulent kinetic energy budget, while the former has a small contribution for the RMI turbulence studied in this work. The production term is large over time in RTI and buoyancy-driven variable-density turbulence due to the continuous conversion of potential energy into kinetic energy [53,59,71]. However, this mechanism does not exist in RMI.

XII. EFFECTS OF FILTERING ON THE BUDGETS OF THE LARGE-SCALE SECOND MOMENTS AFTER RESHOCK

The effects of filtering on the budgets of different large-scale second moments and turbulent kinetic energy with $\ell \approx 16\Delta$ and $\ell \approx 64\Delta$ at $t = 1.40$ ms after reshock are shown in Figs. 33–36, respectively. Note that the unfiltered budgets and the filtered budgets with another filter width can be found in the Supplemental Material [52].

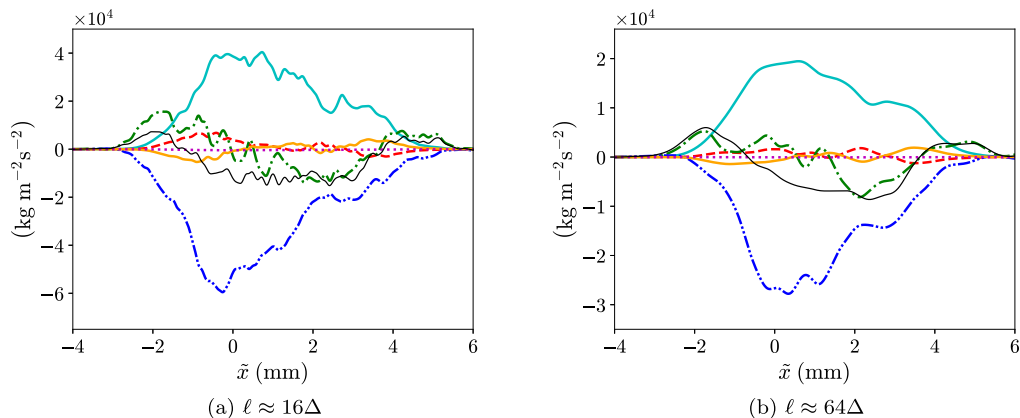


FIG. 33. Effect of filtering on the budgets of the large-scale turbulent mass flux component in the streamwise direction, $\langle \bar{\rho} \rangle_{\ell} a_{L,1}$, given by Eq. (55), at $t = 1.40$ ms. Cyan solid line: production [term (III)]; red dashed line: redistribution [term (IV)]; green dash-dotted line: turbulent transport [term (V)]; blue dash-dot-dotted line: destruction [term (VI)]; orange dash-triple-dotted line: negative of convection due to streamwise velocity associated with turbulent mass flux; magenta dotted line: residue; thin black solid line: summation of all terms (rate of change in the moving frame).

It should be mentioned that the budget of $\bar{\rho} a_1$ is already closed when no filtering is used and hence from Fig. 33, it can be seen that the residues in the budgets of the corresponding large-scale turbulent mass flux component with different filter widths are also negligible across the entire mixing region. Similar to the effects of the filter on the large-scale second-moments, the magnitudes of different terms in the transport equation for the large-scale turbulent mass flux component decrease when a larger filter width is applied on the mixture density and momentum equations, but their shapes remain quite similar. From Figs. 34 and 35, it can be seen that the residues in the budgets of the density-specific-volume covariance and the Reynolds normal stress component

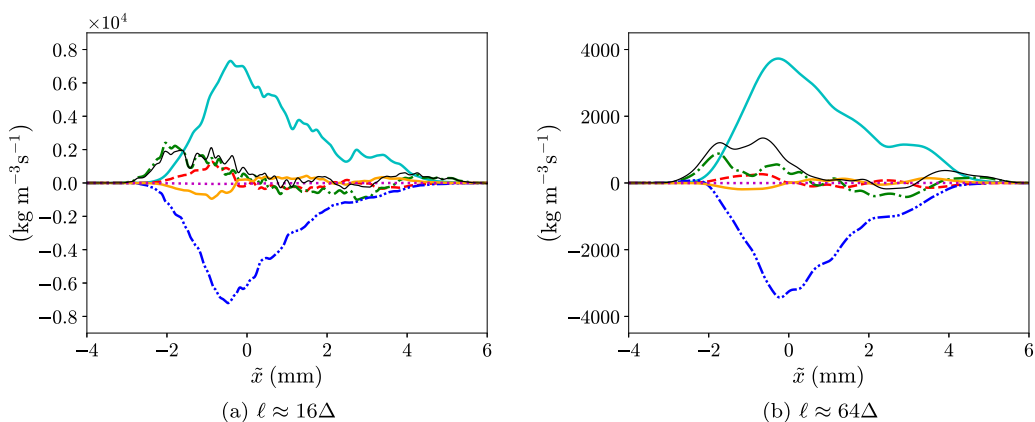


FIG. 34. Effect of filtering on the budgets of the large-scale density-specific-volume covariance multiplied by the mean filtered density, $\langle \bar{\rho} \rangle_{\ell} b_L$, given by Eq. (57), at $t = 1.40$ ms. Cyan solid line: production [term (III)]; red dashed line: redistribution [term (IV)]; green dash-dotted line: turbulent transport [term (V)]; blue dash-dot-dotted line: destruction [term (VI)]; orange dash-triple-dotted line: negative of convection due to streamwise velocity associated with turbulent mass flux; magenta dotted line: residue; thin black solid line: summation of all terms (rate of change in the moving frame).

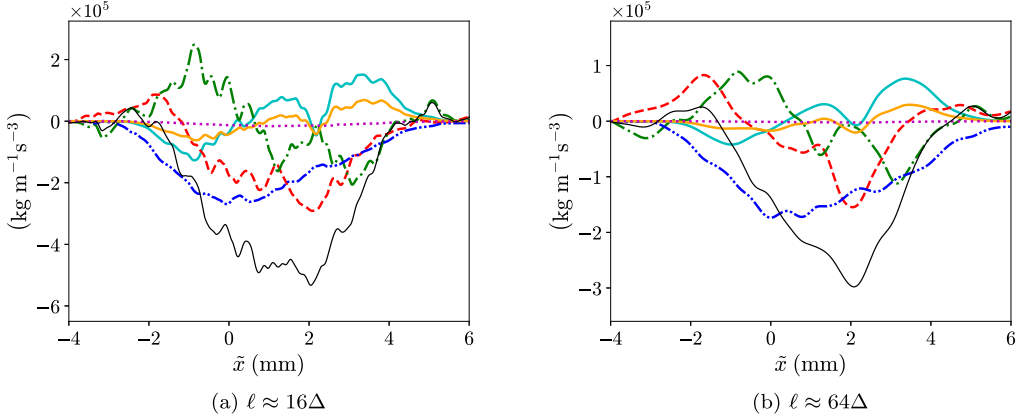


FIG. 35. Effect of filtering on the budgets of the large-scale Reynolds normal stress component in the streamwise direction multiplied by the mean filtered density, $\overline{(\rho)}_\ell \tilde{R}_{L,11}$, given by Eq. (52), at $t = 1.40$ ms. Cyan solid line: production [term (III)]; red dashed line: press-strain redistribution [term (V)]; green dash-dotted line: turbulent transport [term (IV)]; blue dash-dot-dotted line: dissipation [term (VI)]; orange dash-triple-dotted line: negative of convection due to streamwise velocity associated with turbulent mass flux; magenta dotted line: residue; thin black solid line: summation of all terms (rate of change in the moving frame).

(both multiplied by the mean filtered density) are already virtually zero when the Navier-Stokes equations are filtered with filter width $\ell \approx 16\Delta$. The shapes of different terms in the budgets of the two large-scale second moments also appear similar, and the magnitudes reduce with a larger filter width. As for the budgets of large-scale turbulent kinetic energy, an even larger filter width or more successive filtering operations are needed for the residue to become negligibly small, which is indicated by Fig. 36. Nevertheless, the budget terms of the large-scale turbulent kinetic energy are also quite similar for filter widths $\ell \approx 16\Delta$ and $\ell \approx 64\Delta$. From all of these figures mentioned above, it can also be noticed that the ratios of the magnitudes between the major terms for each

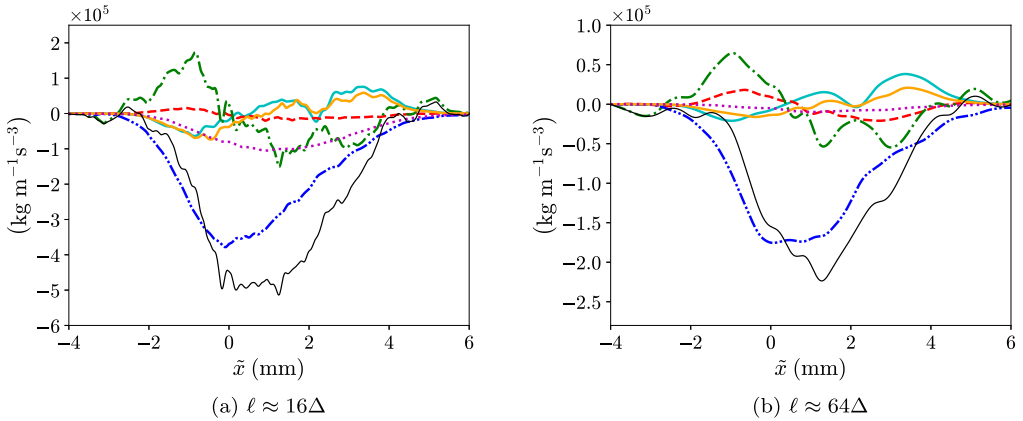


FIG. 36. Effect of filtering on the budgets of the large-scale turbulent kinetic energy, $\overline{(\rho)}_\ell k_L$, given by Eq. (54), at $t = 1.40$ ms. Cyan solid line: production [term (III)]; red dashed line: pressure-dilatation [term (V)]; green dash-dotted line: turbulent transport [term (IV)]; blue dash-dot-dotted line: dissipation [term (VI)]; orange dash-triple-dotted line: negative of convection due to streamwise velocity associated with turbulent mass flux; magenta dotted line: residue; thin black solid line: summation of all terms (rate of change in the moving frame).

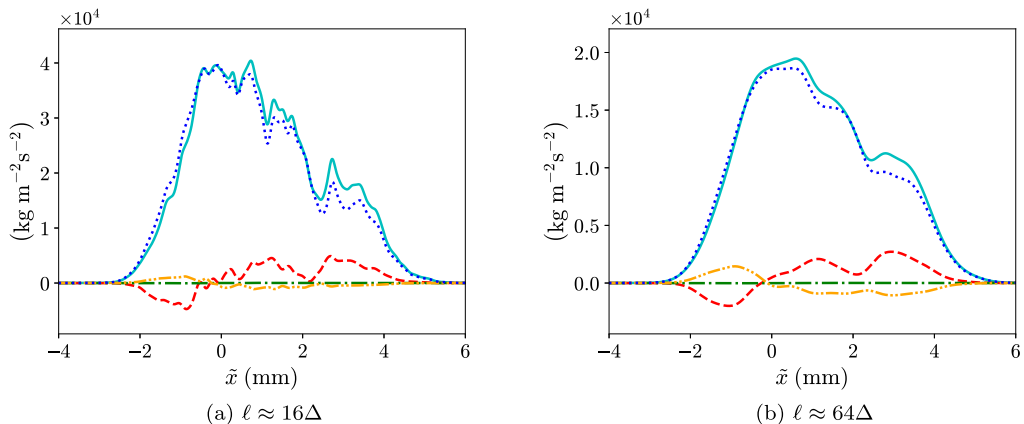


FIG. 37. Effect of filtering on the compositions of the production term [term (III)] in the transport equation for the large-scale turbulent mass flux component in the streamwise direction, $\overline{\langle \rho \rangle}_\ell a_{L,1}$, at $t = 1.40$ ms. Cyan solid line: overall production; red dashed line: $b_L \overline{\langle p \rangle}_{\ell,1}$; green dash-dotted line: $-b_L \overline{\langle \tau_{11} \rangle}_{\ell,1}$; orange dash-dot-dotted line: $b_L \tau_{11}^{\text{SFS}}_{\ell,1}$; blue dotted line: $-\tilde{R}_{L,11} \overline{\langle \rho \rangle}_{\ell,1}$.

budget do not change much with different filter widths. Thus, the budget terms in each transport equation are quite self-similar with different degrees of filtering.

Figures 37 and 38, respectively, show the effects of filtering on the compositions of the production [term (III)] and destruction [term (VI)] terms in the budgets of the large-scale turbulent mass flux component in the streamwise direction at $t = 1.40$ ms. It can be seen from both figures that the magnitudes of the components with the SFS stress in the production and destruction compositions, $b_L \tau_{11}^{\text{SFS}}_{\ell,1}$ and $\overline{\langle \rho \rangle}_\ell (1/\overline{\langle \rho \rangle}_\ell)' (\partial \tau_{1i}^{\text{SFS}'}/\partial x_i)$, increase when a larger filter width is applied. Examining the production term, while there is a larger effect from the constituent with the SFS stress, $b_L \tau_{11}^{\text{SFS}}_{\ell,1}$, with a wider filter width, the magnitude of term $b_L \overline{\langle p \rangle}_{\ell,1}$ also becomes larger to offset the increased effect

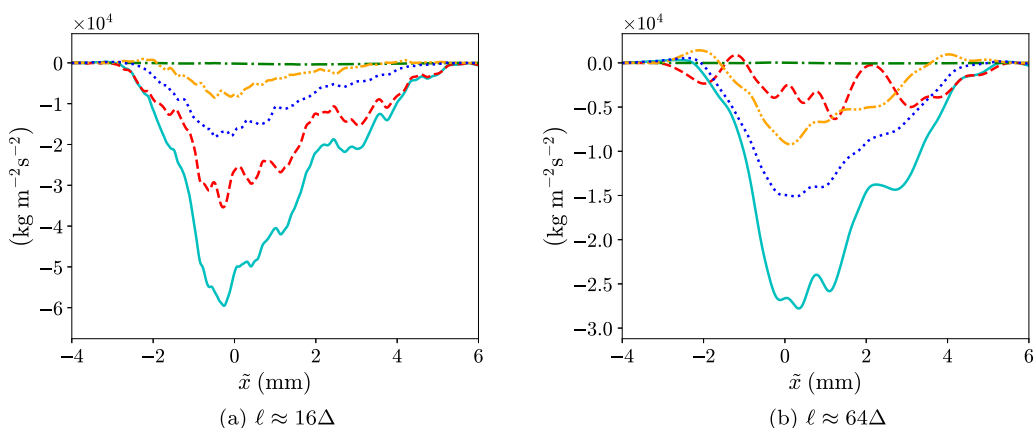


FIG. 38. Effect of filtering on the compositions of the destruction term [term (VI)] in the transport equation for the large-scale turbulent mass flux component in the streamwise direction, $\overline{\langle \rho \rangle}_\ell a_{L,1}$, at $t = 1.40$ ms. Cyan solid line: overall destruction; red dashed line: $\overline{\langle \rho \rangle}_\ell (1/\overline{\langle \rho \rangle}_\ell)' \overline{\langle p \rangle}_{\ell,1}$; green dash-dotted line: $-\overline{\langle \rho \rangle}_\ell (1/\overline{\langle \rho \rangle}_\ell)' (\partial \tau_{1i} \overline{\rho}_{\ell} / \partial x_i)$; orange dash-dot-dotted line: $\overline{\langle \rho \rangle}_\ell (1/\overline{\langle \rho \rangle}_\ell)' (\partial \tau_{1i}^{\text{SFS}'}/\partial x_i)$; blue dotted line: $\overline{\langle \rho \rangle}_\ell e_{a_{L,1}}$.

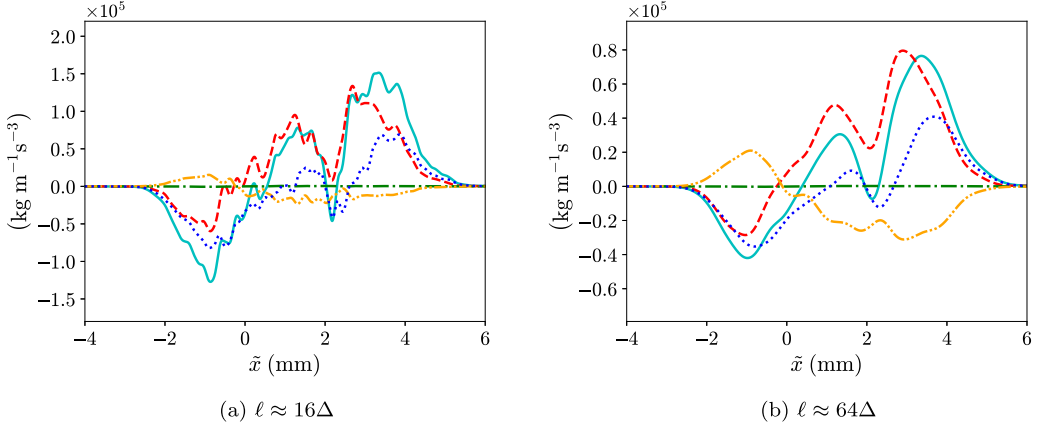


FIG. 39. Effect of filtering on the compositions of the production term [term (III)] in the transport equation for the large-scale Favre-averaged Reynolds normal stress component in the streamwise direction multiplied by the mean filtered density, $\langle \rho \rangle_\ell \widetilde{R}_{L,11}$, at $t = 1.40$ ms. Cyan solid line: overall production; red dashed line: $2a_{L,1} \langle \overline{p} \rangle_{\ell,1}$; green dash-dotted line: $-2a_{L,1} \langle \overline{\tau_{11}} \rangle_{\ell,1}$; orange dash-dot-dotted line: $2a_{L,1} \overline{\tau_{11}^{\text{SFS}}}$; blue dotted line: $-2 \langle \overline{\rho} \rangle_\ell \widetilde{R}_{L,11} \langle \overline{u} \rangle_{L,1}$.

from $b_L \overline{\tau_{11}^{\text{SFS}}}$. Thus, the shape of the overall production term remains self-similar with filtering. As for the destruction term, the corresponding component with SFS stress also increases in magnitude to provide more of a destruction effect when the filter width is larger, but another two constituents, $\langle \overline{\rho} \rangle_\ell (1/\langle \overline{\rho} \rangle_\ell)' \langle \overline{p} \rangle_{\ell,1}'$ and $\langle \overline{\rho} \rangle_\ell \varepsilon_{aL,1}$, adjust (the magnitude of the former decreases and that of the latter increases) and hence the overall destruction term is also self-similar with filtering.

The effects of filtering on the composition of the production [term (III)] and turbulent transport [term (IV)] terms in the budget of the large-scale Reynolds normal stress component in the streamwise direction multiplied by the mean filtered density are studied in Figs. 39 and 40, respectively, at $t = 1.40$ ms. The component with the SFS stress in the production term, $2a_{L,1} \overline{\tau_{11}^{\text{SFS}}}$, has a larger

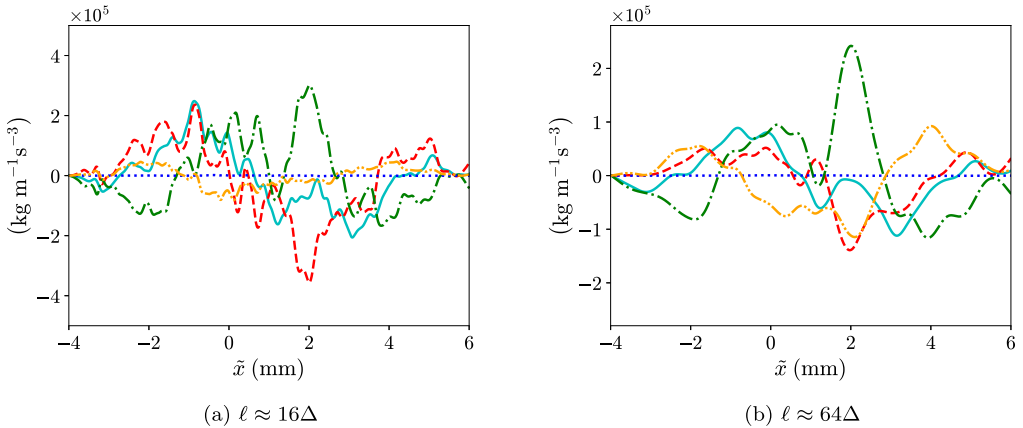


FIG. 40. Effect of filtering on the compositions of the turbulent transport term [term (IV)] in the transport equation for the large-scale Favre-averaged Reynolds normal stress component in the streamwise direction multiplied by the mean filtered density, $\langle \overline{\rho} \rangle_\ell \widetilde{R}_{L,11}$, at $t = 1.40$ ms. Cyan solid line: overall turbulent transport; red dashed line: $-\langle \overline{\rho} \rangle_\ell \langle \overline{u} \rangle_L'' \langle \overline{u} \rangle_L'' \langle \overline{u} \rangle_L''$; green dash-dotted line: $-2 \langle \overline{u} \rangle_L' \langle \overline{p} \rangle_{\ell,1}'$; blue dotted line: $2 \langle \overline{u} \rangle_L' \langle \overline{\tau_{11}} \rangle_{\ell,1}'$; orange dash-dot-dotted line: $-2 \langle \overline{u} \rangle_L' \overline{\tau_{11}^{\text{SFS}}}$.

magnitude with more filtering operations, but this change is offset by the adjustment of $2a_{L,1}\overline{\langle p \rangle}_{\ell,1}$, which also has a larger magnitude but the opposite effect compared with the former. Similarly, the constituent with SFS stress in the turbulent transport term, $-2\langle \langle u \rangle'_L \tau_{11}' \rangle_{,1}$, has a greater magnitude as the filter width increases, but its larger influence is offset by the change of $-2\langle \langle u \rangle'_L \langle p \rangle'_\ell \rangle_{,1}$. In general, the overall shapes of the production and turbulent transport terms are quite similar for different filter widths, but their compositions change as the SFS stress plays a more important role in each of the two terms.

XIII. CONCLUSIONS

A second-moment analysis of high Atwood number variable-density mixing induced by RMI was conducted with high-resolution 3D AMR simulation data. In the numerical experiment, the material interface separating SF₆ and air is impulsively accelerated twice and the mixing layer becomes turbulent after reshock. The roles that the two second moments, turbulent mass flux and density-specific-volume covariance, play in the development of Favre-averaged Reynolds stress were discussed through the examination of the transport equations for the second moments, including the Favre-averaged Reynolds stress and turbulent kinetic energy. The study of the transport mechanisms of the second moments can foster the improvement of existing reduced-order models for closing the Favre-averaged Navier-Stokes equations in RANS-based simulations. The quantities of interest, including the second moments computed with the simulation data, were found to be well grid-converged at the finest grid setting, and the study of their time evolution revealed the non-Boussinesq and anisotropic nature of the variable-density flow induced by RMI. The transport equations of the Reynolds stress and second moments were studied before reshock when mixing occurs due to the instability. The relative importance of different terms in the budgets of the quantities across the mixing layer was found to vary a lot, and the origins of the generation, destruction, and spreading of the quantities of interest over time were traced back to the corresponding budget terms. Unlike the situation where all scales in the flow are well-resolved in the highest resolution simulation before reshock, the wide span of scales generated due to mixing transition after reshock leads to underresolved simulation results. While the budgets of some second moments, including the Reynolds stress, are unclosed during this time period, the budgets of large-scale Reynolds stress and second moments at sufficiently large scale were found to be unaffected by the numerical regularization, when the influence of the SFS stress is taken into account. The effects of the SFS stress on the development of large-scale quantities at different filtered scales were studied. Although the SFS stress can significantly contribute to the composition of different budget terms when a large filter width is used, the overall budgets of large-scale Reynolds stress and second moments remain quite self-similar with filtering as the shapes of different budget terms and their relative magnitudes are similar with different filter widths. This suggests that the budget analysis of large-scale quantities in LESs can be relevant for the development and validation of RANS-based closures that model each budget term as a whole, even when the Reynolds stress and turbulent kinetic energy are not well-resolved, provided that the effects of an accurate representation of the SFS stress are included in the budget terms. This also addresses the importance of reconstructing the SFS stress in LESs of this type of variable-density flows in order to model the development of the turbulence accurately. Nevertheless, the study of the evolution mechanism of the SFS stress requires an analysis of its transport equation with fully resolved turbulence data. As a result, future research of RMI-induced variable-density turbulence with higher resolution simulations, such as DNSs that resolve all spatiotemporal scales, can largely advance turbulence modeling in LES, RANS, and hybrid RANS-LES approaches.

ACKNOWLEDGMENTS

This work was performed under the auspices of U.S. Department of Energy. M.L.W. and S.K.L. were supported by Los Alamos National Laboratory under Grant No. 431679. Los Alamos National

Laboratory is operated by Triad National Security, LLC, for the National Nuclear Security Administration of U.S. Department of Energy (Contract No. 89233218CNA000001). Computational resources were provided by the Los Alamos National Laboratory Institutional Computing Program and the Advanced Simulation and Computation (ASC) Program.

APPENDIX A: GRID SENSITIVITY ANALYSIS OF THE SPATIAL PROFILES OF SECOND MOMENTS

The grid sensitivities of the spatial profiles of $\bar{\rho}a_1$, b , $\bar{\rho}\tilde{R}_{11}$, and $\bar{\rho}k$ at different times between the grid D and the grid E are shown, respectively, in Figs. 41–44. Overall, these spatial profiles have small grid sensitivities between the two grid resolutions at different times, which are consistent with the grid sensitivities of the time evolution of the domain-integrated values.

APPENDIX B: TIME EVOLUTION OF THE NUMBERS OF GRID CELLS IN THE SIMULATIONS

Figure 45 shows the number of grid cells and the weighted number of grid cells summed over all grid levels for different AMR grid resolutions over time. The weighted number of grid cells is defined as

$$\sum_{l=0}^{l_{\max}} \frac{\Delta x_{l_{\max}}}{\Delta x_l} N_l, \quad (\text{B1})$$

where N_l and Δx_l are the number of grid cells and grid spacing, respectively, at level l . The maximum level number $l_{\max} = 2$ is used in this work. The weighted number of grid cells accounts for the fact that the time step size is larger for grid cells at the lower grid level from the CFL condition and has less computational cost compared to grid cells at higher grid levels. Since larger time step sizes are used for coarser grid levels in the multitime stepping (subcycling) algorithm of the AMR code, the weighted number of grid cells is a better metric for comparing the computational cost of different AMR simulations. From Fig. 45, it can be seen that both the number of cells and the weighted number of cells are the largest near the end of simulation for each grid resolution. The maximum number of cells and the weighted number of cells for the grid E setting are around 4.55

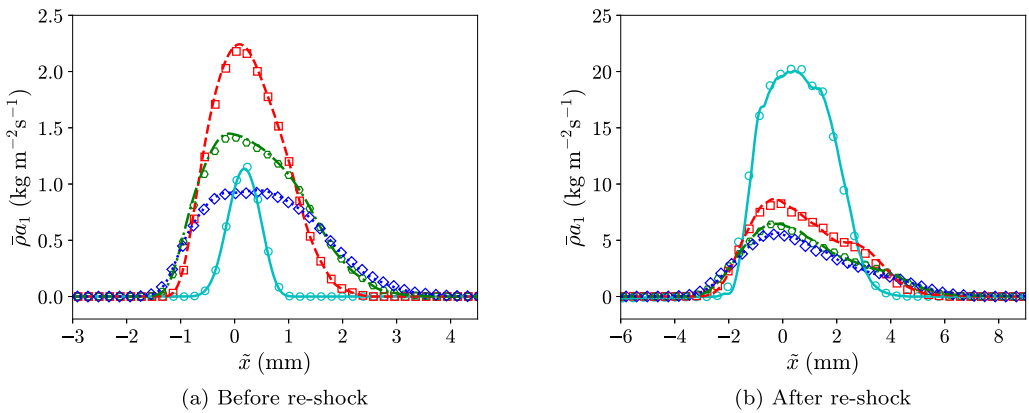


FIG. 41. Grid sensitivities of the profiles of the turbulent mass flux component in the streamwise direction, $\bar{\rho}a_1$, at different times between the grid D and the grid E. The profiles with the grid D and the grid E are shown with symbols and lines, respectively. Cyan circles or solid line in (a): $t = 0.05$ ms; red squares or dashed line in (a): $t = 0.40$ ms; green hexagons or dash-dotted line in (a): $t = 0.75$ ms; blue diamonds or dotted line in (a): $t = 1.10$ ms. Cyan circles or solid line in (b): $t = 1.20$ ms; red squares or dashed line in (b): $t = 1.40$ ms; green hexagons or dash-dotted line in (b): $t = 1.60$ ms; blue diamonds or dotted line in (b): $t = 1.75$ ms.

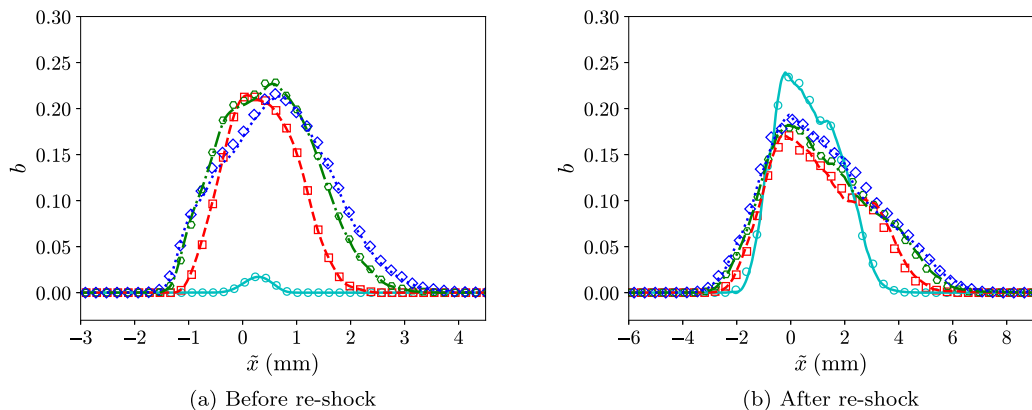


FIG. 42. Grid sensitivities of the profiles of the density-specific-volume covariance, b , at different times between the grid D and the grid E. The profiles with the grid D and the grid E are shown with symbols and lines, respectively. Cyan circles or solid line in (a): $t = 0.05$ ms; red squares or dashed line in (a): $t = 0.40$ ms; green hexagons or dash-dotted line in (a): $t = 0.75$ ms; blue diamonds or dotted line in (a): $t = 1.10$ ms. Cyan circles or solid line in (b): $t = 1.20$ ms; red squares or dashed line in (b): $t = 1.40$ ms; green hexagons or dash-dotted line in (b): $t = 1.60$ ms; blue diamonds or dotted line in (b): $t = 1.75$ ms.

and 4.19 billion, respectively. Both the number of cells and the weighted number of cells are close to each other over time since most of the grid cells are on the finest level.

APPENDIX C: TRANSPORT COEFFICIENTS

The shear viscosity, μ_i , of species i is given by the Chapman-Enskog model [72]:

$$\mu_i = 2.6693 \times 10^{-6} \frac{\sqrt{M_i T}}{\Omega_{\mu,i} \sigma_i^2}, \quad (\text{C1})$$

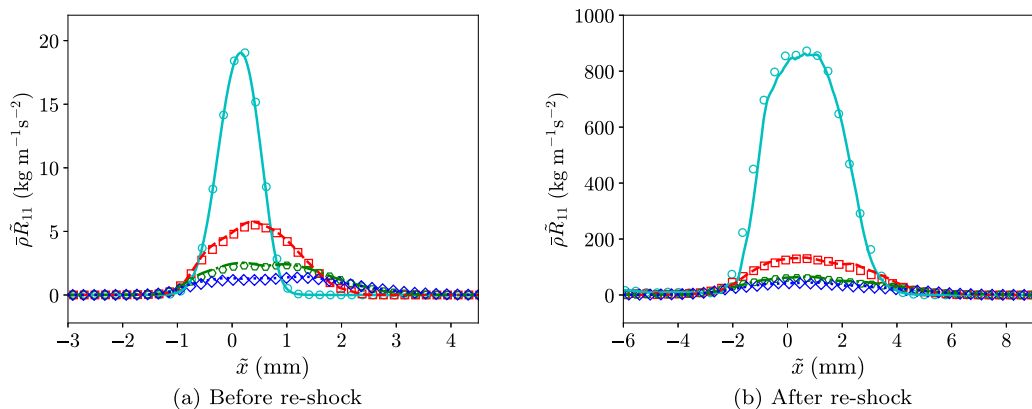


FIG. 43. Grid sensitivities of the profiles of the Reynolds normal stress component in the streamwise direction multiplied by the mean density, $\bar{\rho} \bar{R}_{11}$, at different times between the grid D and the grid E. The profiles with the grid D and the grid E are shown with symbols and lines, respectively. Cyan circles or solid line in (a): $t = 0.05$ ms; red squares or dashed line in (a): $t = 0.40$ ms; green hexagons or dash-dotted line in (a): $t = 0.75$ ms; blue diamonds or dotted line in (a): $t = 1.10$ ms. Cyan circles or solid line in (b): $t = 1.20$ ms; red squares or dashed line in (b): $t = 1.40$ ms; green hexagons or dash-dotted line in (b): $t = 1.60$ ms; blue diamonds or dotted line in (b): $t = 1.75$ ms.

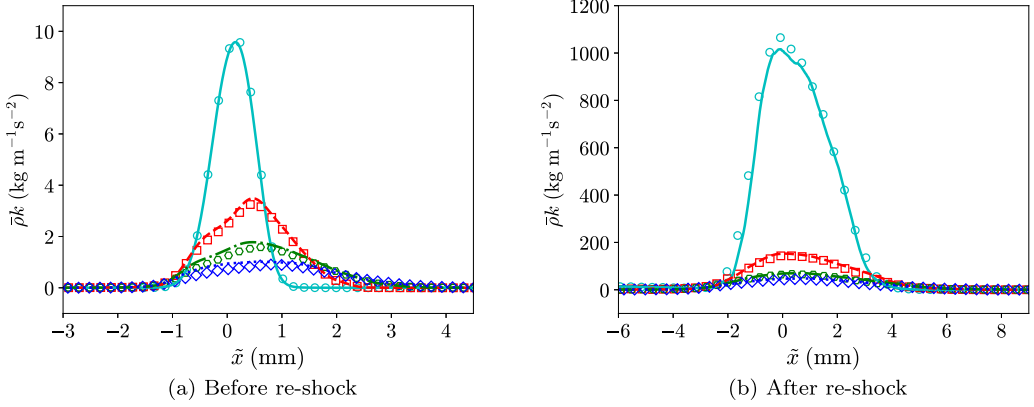


FIG. 44. Grid sensitivities of the profiles of the turbulent kinetic energy, $\bar{\rho}k$, at different times between the grid D and the grid E. The profiles with the grid D and the grid E are shown with symbols and lines, respectively. Cyan circles or solid line in (a): $t = 0.05$ ms; red squares or dashed line in (a): $t = 0.40$ ms; green hexagons or dash-dotted line in (a): $t = 0.75$ ms; blue diamonds or dotted line in (a): $t = 1.10$ ms. Cyan circles or solid line in (b): $t = 1.20$ ms; red squares or dashed line in (b): $t = 1.40$ ms; green hexagons or dash-dotted line in (b): $t = 1.60$ ms; blue diamonds or dotted line in (b): $t = 1.75$ ms.

where σ_i is the collision diameter and $\Omega_{\mu,i}$ is the collision integral of the species given by

$$\Omega_{\mu,i} = A(T_i^*)^B + C \exp(DT_i^*) + E \exp(FT_i^*), \quad (\text{C2})$$

where $T_i^* = T/(\epsilon/k)_i$, $A = 1.16145$, $B = -0.14874$, $C = 0.52487$, $D = -0.7732$, $E = 2.16178$, and $F = -2.43787$. T is the temperature of the species. $(\epsilon/k)_i$ is the Lennard-Jones energy parameter, and M_i is the molecular mass of the species. The values of M_i , $(\epsilon/k)_i$, and σ_i are given in Table IV.

The bulk viscosity, μ_v , of air is given by the linear model by Gu and Ubachs [73]:

$$\mu_v = A + BT, \quad (\text{C3})$$

where $A = -3.15 \times 10^{-5} \text{ kg m}^{-1} \text{ s}^{-1}$ and $B = 1.58 \times 10^{-7} \text{ kg m}^{-1} \text{ s}^{-1} \text{ K}^{-1}$.

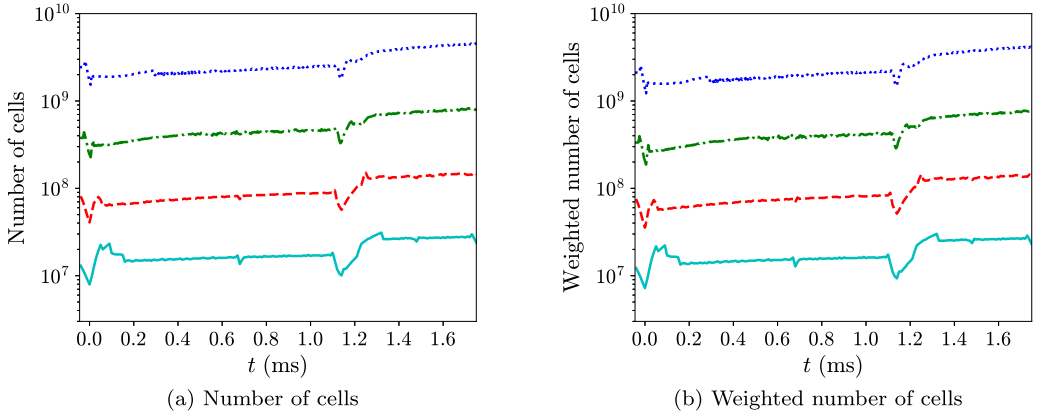


FIG. 45. Number of grid cells during the simulations. Cyan solid line: grid B; red dashed line: grid C; green dash-dotted line: grid D; blue dotted line: grid E.

TABLE IV. Fluid properties.

Gas	γ_i	$c_{p,i}$ (J kg ⁻¹ K ⁻¹)	$c_{v,i}$ (J kg ⁻¹ K ⁻¹)	M_i (g mol ⁻¹)	R_i (J kg ⁻¹ K ⁻¹)	$(\epsilon/k)_i$ (K)	σ_i (Å)	Pr_i
SF ₆	1.09312	668.286	611.359	146.055	56.9269	222.1	5.128	0.79
Air	1.39909	1040.50	743.697	28.0135	296.802	78.6	3.711	0.71

The bulk viscosity, μ_v , of SF₆ is given by Cramer's model [74]:

$$\mu_v = (\gamma - 1)^2 c_v|_v (p\tau_v), \quad (\text{C4})$$

$$c_v|_v = \left(\frac{c_v}{R} - \frac{f_r + 3}{2} \right), \quad (\text{C5})$$

$$(p\tau_v) = A \exp\left(\frac{B}{T^{1/3}} + \frac{C}{T^{2/3}} \right), \quad (\text{C6})$$

where $f_r = 3$, $A = 0.2064 \times 10^{-5}$ kg m⁻¹ s⁻¹, $B = 121$ K^{1/3}, and $C = -339$ K^{2/3} for SF₆.

The thermal conductivity of species i , κ_i , is defined by

$$\kappa_i = c_{p,i} \frac{\mu_i}{\text{Pr}_i}, \quad (\text{C7})$$

where Pr_i and $c_{p,i}$ are the species-specific Prandtl number and specific heat at constant pressure, respectively.

Mass diffusion coefficient of a binary mixture, D_{ij} , is given by [75]

$$D_{ij} = D_i = D_j = \frac{0.0266}{\Omega_{D,ij}} \frac{T^{3/2}}{p\sqrt{M_{ij}\sigma_{ij}^2}}, \quad (\text{C8})$$

where p and T are the pressure and temperature of the mixture. $\Omega_{D,ij}$ is the collision integral for diffusion given by

$$\Omega_{D,ij} = A(T_{ij}^*)^B + C \exp(DT_{ij}^*) + E \exp(FT_{ij}^*) + G \exp(HT_{ij}^*), \quad (\text{C9})$$

where $T_{ij}^* = T/T_{\epsilon_{ij}}$, $A = 1.06036$, $B = -0.1561$, $C = 0.19300$, $D = -0.47635$, $E = 1.03587$, $F = -1.52996$, $G = 1.76474$, and $H = -3.89411$. M_{ij} , σ_{ij} , and $T_{\epsilon_{ij}}$ are the effective molecular mass, collision diameter, and Lennard-Jones energy parameter, respectively, for the mixture:

$$M_{ij} = \frac{2}{\frac{1}{M_i} + \frac{1}{M_j}}, \quad (\text{C10})$$

$$\sigma_{ij} = \frac{\sigma_i + \sigma_j}{2}, \quad (\text{C11})$$

$$T_{\epsilon_{ij}} = \sqrt{\left(\frac{\epsilon}{k} \right)_i \left(\frac{\epsilon}{k} \right)_j}. \quad (\text{C12})$$

The values of M_i , $(\epsilon/k)_i$, and σ_i of different species are given in Table IV.

APPENDIX D: MIXING RULES

With the assumption that all species are at pressure and temperature equilibria, the ratio of specific heats of the mixture follows as

$$\gamma = \frac{c_p}{c_v}, \quad c_p = \sum_{i=1}^N Y_i c_{p,i}, \quad c_v = \sum_{i=1}^N Y_i c_{v,i}. \quad (\text{D1})$$

The molecular mass of the mixture is given by

$$M = \left(\sum_{i=1}^N \frac{Y_i}{M_i} \right)^{-1}. \quad (\text{D2})$$

The mixture shear viscosity, bulk viscosity, and thermal conductivity are given by

$$\mu = \frac{\sum_{i=1}^N \mu_i Y_i / \sqrt{M_i}}{\sum_{i=1}^N Y_i / \sqrt{M_i}}, \quad (\text{D3})$$

$$\mu_v = \frac{\sum_{i=1}^N \mu_{v,i} Y_i / \sqrt{M_i}}{\sum_{i=1}^N Y_i / \sqrt{M_i}}, \quad (\text{D4})$$

$$\kappa = \frac{\sum_{i=1}^N \kappa_i Y_i / \sqrt{M_i}}{\sum_{i=1}^N Y_i / \sqrt{M_i}}. \quad (\text{D5})$$

-
- [1] R. D. Richtmyer, Taylor instability in shock acceleration of compressible fluids, *Commun. Pure Appl. Math.* **13**, 297 (1960).
- [2] E. E. Meshkov, Instability of the interface of two gases accelerated by a shock wave, *Fluid Dyn.* **4**, 101 (1969).
- [3] Y. Zhou, Rayleigh-Taylor and Richtmyer-Meshkov instability induced flow, turbulence, and mixing. i, *Phys. Rep.* **720**, 1 (2017).
- [4] K. Kifonidis, T. Plewa, L. Scheck, H.-Th. Janka, and E. Müller, Non-spherical core collapse supernovae-II. the late-time evolution of globally anisotropic neutrino-driven explosions and their implications for SN 1987 A, *Astron. & Astrophys.* **453**, 661 (2006).
- [5] J. Guzman and T. Plewa, Non-spherical core-collapse supernovae: evolution towards homologous expansion, *Nonlinearity* **22**, 2775 (2009).
- [6] N. J. Hammer, H.-Th. Janka, and E. Müller, Three-dimensional simulations of mixing instabilities in supernova explosions, *Astrophys. J.* **714**, 1371 (2010).
- [7] D. Arnett, The role of mixing in astrophysics, *Astrophys. J. Suppl. Ser.* **127**, 213 (2000).
- [8] S. W. Haan, S. M. Pollaine, J. D. Lindl, L. J. Suter, R. L. Berger, L. V. Powers, W. E. Alley, P. A. Amendt, J. A. Futterman, W. K. Levedahl *et al.*, Design and modeling of ignition targets for the National Ignition Facility, *Phys. Plasmas* **2**, 2480 (1995).
- [9] S. W. Haan, J. D. Lindl, D. A. Callahan, D. S. Clark, J. D. Salmonson, B. A. Hammel, L. J. Atherton, R. C. Cook, M. J. Edwards, S. Glenzer *et al.*, Point design targets, specifications, and requirements for the 2010 ignition campaign on the National Ignition Facility, *Phys. Plasmas* **18**, 051001 (2011).
- [10] K. S. Raman, V. A. Smalyuk, D. T. Casey, S. W. Haan, D. E. Hoover, O. A. Hurricane, J. J. Kroll, A. Nikroo, J. L. Peterson, B. A. Remington *et al.*, An in-flight radiography platform to measure hydrodynamic instability growth in inertial confinement fusion capsules at the National Ignition Facility, *Phys. Plasmas* **21**, 072710 (2014).
- [11] J. Yang, T. Kubota, and E. E. Zukoski, Applications of shock-induced mixing to supersonic combustion, *AIAA J.* **31**, 854 (1993).
- [12] Q. Yang, J. Chang, and W. Bao, Richtmyer-Meshkov instability induced mixing enhancement in the scramjet combustor with a central strut, *Adv. Mech. Eng.* **6**, 614189 (2014).
- [13] D. Livescu, Turbulence with large thermal and compositional density fluctuations, *Annu. Rev. Fluid Mech.* **52**, 309 (2020).
- [14] P. Moin and K. Mahesh, Direct numerical simulation: A tool in turbulence research, *Annu. Rev. Fluid Mech.* **30**, 539 (1998).
- [15] M. Lesieur, O. Métais, P. Comte *et al.*, *Large-eddy Simulations of Turbulence* (Cambridge University Press, Cambridge, 2005)
- [16] S. B. Pope, *Turbulent Flows* (Cambridge University Press, Cambridge, 2000).

- [17] B. Chaouat, The state of the art of hybrid rans/les modeling for the simulation of turbulent flows, *Flow, Turbul. Combust.* **99**, 279 (2017).
- [18] D. Besnard, F. H. Harlow, R. M. Rauenzahn, and C. Zemach, Turbulence transport equations for variable-density turbulence and their relationship to two-field models, Tech. Rep. (Los Alamos National Lab., NM, 1992).
- [19] A. Banerjee, R. A. Gore, and M. J. Andrews, Development and validation of a turbulent-mix model for variable-density and compressible flows, *Phys. Rev. E* **82**, 046309 (2010).
- [20] K. Stalsberg-Zarling and R. A. Gore, The BHR2 turbulence model: incompressible isotropic decay, Rayleigh-Taylor, Kelvin-Helmholtz and homogeneous variable density turbulence, LANL Report, LA-UR-11, 4773 (2011).
- [21] J. D. Schwarzkopf, D. Livescu, R. A. Gore, R. M. Rauenzahn, and J. R. Ristorcelli, Application of a second-moment closure model to mixing processes involving multicomponent miscible fluids, *J. Turbul.* **12**, N49 (2011).
- [22] J. D. Schwarzkopf, D. Livescu, J. R. Baltzer, R. A. Gore, and J. R. Ristorcelli, A two-length scale turbulence model for single-phase multi-fluid mixing, *Flow, Turbul. Combust.* **96**, 1 (2016).
- [23] M. J. Steinkamp, T. T. Clark, and F. H. Harlow, Two-point description of two-fluid turbulent mixing-i. model formulation, *Int. J. Multiphase Flow* **25**, 599 (1999).
- [24] M. J. Steinkamp, T. T. Clark, and F. H. Harlow, Two-point description of two-fluid turbulent mixing-ii. numerical solutions and comparisons with experiments, *Int. J. Multiphase Flow* **25**, 639 (1999).
- [25] D. C. Besnard, F. H. Harlow, R. M. Rauenzahn, and C. Zemach, Spectral transport model for turbulence, *Theor. Comput. Fluid Dyn.* **8**, 1 (1996).
- [26] N. Pal, S. Kurien, T. Clark, D. Aslangil, and D. Livescu, Two-point spectral model for variable-density homogeneous turbulence, *Phys. Rev. Fluids* **3**, 124608 (2018).
- [27] N. Pal, I. Boureima, N. Braun, S. Kurien, P. Ramaprabhu, and A. Lawrie, Local wave-number model for inhomogeneous two-fluid mixing, *Phys. Rev. E* **104**, 025105 (2021).
- [28] O. Grégoire, D. Souffland, and S. Gauthier, A second-order turbulence model for gaseous mixtures induced by Richtmyer-Meshkov instability, *J. Turbul.* **6**, N29 (2005).
- [29] B. E. Morgan and M. E. Wickett, Three-equation model for the self-similar growth of Rayleigh-Taylor and Richtmyer-Meshkov instabilities, *Phys. Rev. E* **91**, 043002 (2015).
- [30] G. Dimonte and R. Tipton, K-L turbulence model for the self-similar growth of the Rayleigh-Taylor and Richtmyer-Meshkov instabilities, *Phys. Fluids* **18**, 085101 (2006).
- [31] Y. Zhou, Rayleigh-Taylor and Richtmyer-Meshkov instability induced flow, turbulence, and mixing. ii, *Phys. Rep.* **723**, 1 (2017).
- [32] P. Chassaing, The modeling of variable density turbulent flows. a review of first-order closure schemes, *Flow, Turbul. Combust.* **66**, 293 (2001).
- [33] J. P. Mellado, S. Sarkar, and Y. Zhou, Large-eddy simulation of Rayleigh-Taylor turbulence with compressible miscible fluids, *Phys. Fluids* **17**, 076101 (2005).
- [34] P. Wang, J. Fröhlich, V. Michelassi, and W. Rodi, Large-eddy simulation of variable-density turbulent axisymmetric jets, *Int. J. Heat Fluid Flow* **29**, 654 (2008).
- [35] J.-s. Bai, J.-h. Liu, T. Wang, L.-y. Zou, P. Li, and D.-w. Tan, Investigation of the Richtmyer-Meshkov instability with double perturbation interface in nonuniform flows, *Phys. Rev. E* **81**, 056302 (2010).
- [36] D. J. Hill, C. Pantano, and D. I. Pullin, Large-eddy simulation and multiscale modelling of a Richtmyer-Meshkov instability with reshock, *J. Fluid Mech.* **557**, 29 (2006).
- [37] G. S. Sidharth and G. V. Candler, Stretched-vortex based subgrid-scale modeling of variable-density flows, in *45th AIAA Fluid Dynamics Conference* (AIAA, Dallas, TX, 2015), p. 2782.
- [38] M. L. Wong, D. Livescu, and S. K. Lele, High-resolution Navier-Stokes simulations of Richtmyer-Meshkov instability with reshock, *Phys. Rev. Fluids* **4**, 104609 (2019).
- [39] J. O. Hirschfelder, C. F. Curtiss, R. B. Bird, and M. G. Mayer, *Molecular Theory of Gases and Liquids* (Wiley, New York, 1954), Vol. 26.
- [40] F. A. Williams, *Combustion Theory* (CRC, Boca Raton, FL, 2018).
- [41] M. L. Wong, High-order shock-capturing methods for study of shock-induced turbulent mixing with adaptive mesh refinement simulations, Ph.D. thesis, Stanford University, 2019.

- [42] B. T. N. Gunney and R. W. Anderson, Advances in patch-based adaptive mesh refinement scalability, *J. Parallel Distrib. Comput.* **89**, 65 (2016).
- [43] B. T. N. Gunney, A. M. Wissink, and D. A. Hysom, Parallel clustering algorithms for structured AMR, *J. Parallel Distrib. Comput.* **66**, 1419 (2006).
- [44] R. D. Hornung, A. M. Wissink, and S. R. Kohn, Managing complex data and geometry in parallel structured AMR applications, *Eng. Comput.* **22**, 181 (2006).
- [45] R. D. Hornung and S. R. Kohn, Managing application complexity in the SAMRAI object-oriented framework, *Concurrency Comput.: Practice Exper.* **14**, 347 (2002).
- [46] A. M. Wissink, R. D. Hornung, S. R. Kohn, S. S. Smith, and N. Elliott, Large scale parallel structured AMR calculations using the SAMRAI framework, in *Supercomputing, ACM/IEEE 2001 Conference* (IEEE, Piscataway, NJ, 2001), pp. 22–22.
- [47] M. L. Wong and S. K. Lele, High-order localized dissipation weighted compact nonlinear scheme for shock-and interface-capturing in compressible flows, *J. Comput. Phys.* **339**, 179 (2017).
- [48] T. Nonomura, S. Morizawa, H. Terashima, S. Obayashi, and K. Fujii, Numerical (error) issues on compressible multicomponent flows using a high-order differencing scheme: Weighted compact nonlinear scheme, *J. Comput. Phys.* **231**, 3181 (2012).
- [49] M. L. Wong, J. B. Angel, M. F. Barad, and C. C. Kiris, A positivity-preserving high-order weighted compact nonlinear scheme for compressible gas-liquid flows, *J. Comput. Phys.* **444**, 110569 (2021).
- [50] C.-W. Shu and S. Osher, Efficient implementation of essentially non-oscillatory shock-capturing schemes, II, *J. Comput. Phys.* **83**, 32 (1989).
- [51] M. L. Wong and S. K. Lele, Multiresolution feature detection in adaptive mesh refinement with high-order shock- and interface-capturing scheme, *46th AIAA Fluid Dynamics Conference, AIAA Aviation* (AIAA, Washington, DC, 2016).
- [52] See Supplemental Material at <http://link.aps.org/supplemental/10.1103/PhysRevFluids.7.044602> for additional details on the initial perturbations, the grid sensitivity analysis of different spatial profiles and budgets, the effects of filtering on the large-scale second moments and their budgets, and the budgets of large-scale second moments at other times not presented in the main article.
- [53] D. Livescu, J. R. Ristorcelli, R. A. Gore, S. H. Dean, W. H. Cabot, and A. W. Cook, High-Reynolds number Rayleigh-Taylor turbulence, *J. Turbul.* **10**, N13 (2009).
- [54] D. Livescu, J. R. Ristorcelli, M. R. Petersen, and R. A. Gore, New phenomena in variable-density Rayleigh-Taylor turbulence, *Phys. Scr.* **2010**, 014015 (2010).
- [55] B. J. Balakumar, G. C. Orlicz, J. R. Ristorcelli, S. Balasubramanian, K. P. Prestridge, and C. D. Tomkins, Turbulent mixing in a Richtmyer-Meshkov fluid layer after reshock: velocity and density statistics, *J. Fluid Mech.* **696**, 67 (2012).
- [56] M. Mohaghar, J. Carter, B. Musci, D. Reilly, J. McFarland, and D. Ranjan, Evaluation of turbulent mixing transition in a shock-driven variable-density flow, *J. Fluid Mech.* **831**, 779 (2017).
- [57] D. T. Reese, A. M. Ames, C. D. Noble, J. G. Oakley, D. A. Rothamer, and R. Bonazza, Simultaneous direct measurements of concentration and velocity in the Richtmyer-Meshkov instability, *J. Fluid Mech.* **849**, 541 (2018).
- [58] D. Aslangil and M. L. Wong, Study of iso-thermal stratification strength on 2d multi-mode compressible Rayleigh-Taylor instability, in *AIAA SciTech 2022 Forum* (AIAA, San Diego, CA, 2022), p. 0456.
- [59] D. Livescu and J. R. Ristorcelli, Buoyancy-driven variable-density turbulence, *J. Fluid Mech.* **591**, 43 (2007).
- [60] S. Balasubramanian, G. C. Orlicz, and K. P. Prestridge, Experimental study of initial condition dependence on turbulent mixing in shock-accelerated Richtmyer-Meshkov fluid layers, *J. Turbul.* **14**, 170 (2013).
- [61] G. C. Orlicz, S. Balasubramanian, and K. P. Prestridge, Incident shock mach number effects on Richtmyer-Meshkov mixing in a heavy gas layer, *Phys. Fluids* **25**, 114101 (2013).
- [62] C. D. Tomkins, B. J. Balakumar, G. Orlicz, K. P. Prestridge, and J. R. Ristorcelli, Evolution of the density self-correlation in developing Richtmyer-Meshkov turbulence, *J. Fluid Mech.* **735**, 288 (2013).
- [63] C. R. Weber, N. S. Haehn, J. G. Oakley, D. A. Rothamer, and R. Bonazza, An experimental investigation of the turbulent mixing transition in the Richtmyer-Meshkov instability, *J. Fluid Mech.* **748**, 457 (2014).
- [64] V. K. Tritschler, B. J. Olson, S. K. Lele, S. Hickel, X. Y. Hu, and N. A. Adams, On the Richtmyer-

- Meshkov instability evolving from a deterministic multimode planar interface, *J. Fluid Mech.* **755**, 429 (2014).
- [65] M. Lombardini, D. I. Pullin, and D. I. Meiron, Turbulent mixing driven by spherical implosions. part 2. turbulence statistics, *J. Fluid Mech.* **748**, 113 (2014).
- [66] M. Mohaghar, J. Carter, G. Pathikonda, and D. Ranjan, The transition to turbulence in shock-driven mixing: Effects of mach number and initial conditions, *J. Fluid Mech.* **871**, 595 (2019).
- [67] D. Livescu and J. R. Ristorcelli, Variable-density mixing in buoyancy-driven turbulence, *J. Fluid Mech.* **605**, 145 (2008).
- [68] S. K. Shankar and S. K. Lele, Numerical investigation of turbulence in reshocked Richtmyer-Meshkov unstable curtain of dense gas, *Shock Waves* **24**, 79 (2014).
- [69] J. A. Saenz, D. Aslangil, and D. Livescu, Filtering, averaging, and scale dependency in homogeneous variable density turbulence, *Phys. Fluids* **33**, 025115 (2021).
- [70] A. W. Cook and W. H. Cabot, Hyperviscosity for shock-turbulence interactions, *J. Comput. Phys.* **203**, 379 (2005).
- [71] D. Aslangil, D. Livescu, and A. Banerjee, Effects of Atwood and Reynolds numbers on the evolution of buoyancy-driven homogeneous variable-density turbulence, *J. Fluid Mech.* **895**, A12 (2020).
- [72] S. Chapman and T. G. Cowling, *The Mathematical Theory of Non-uniform Gases* (Cambridge University Press, Cambridge, 1991), p. 447.
- [73] Z. Gu and W. Ubachs, A systematic study of Rayleigh-Brillouin scattering in air, N₂, and O₂ gases, *J. Chem. Phys.* **141**, 104320 (2014).
- [74] M. S. Cramer, Numerical estimates for the bulk viscosity of ideal gases, *Phys. Fluids (1994-present)* **24**, 066102 (2012).
- [75] B. E. Poling, J. M. Prausnitz, O. John Paul, and R. C. Reid, *The Properties of Gases and Liquids* (McGraw-Hill, New York, 2001), Vol. 5.